Investigation of charge carrier transport in metal halide perovskites by THz Spectroscopy

Andrei Petsiuk

Univ.-Diss.

zur Erlangung des akademischen Grades

"doctor rerum naturalium"

(Dr. rer. nat.)

in der Wissenschaftsdisziplin "Experimentalphysik "

eingereicht an der

Mathematisch-Naturwissenschaftlichen Fakultät

Institut für Physik und Astronomie

der Universität Potsdam

und

außeruniversitäres Institut

Helmholtz Zentrum Berlin

Ort und Tag der Disputation: Universität Potsdam, 15 Juli, 2021.

Hauptbetreuer*in: Prof. Dr. Dieter Neher

Betreuer*innen: Dr. Thomas Unold

Gutachter*innen: Prof. Dr. D. Neher, Prof. Dr. V. Dyakonov, Dr. T. Unold

Published online on the
Publication Server of the University of Potsdam:
https://doi.org/10.25932/publishup-51544
https://nbn-resolving.org/urn:nbn:de:kobv:517-opus4-515441

Table of Contents

1. Introduction

The increased amount of CO_2 emission over the last decades around the globe encourages to search for alternative renewable sources of energy that are more environment friendly. Renewable sources of energy imply to exploit the energy of the sun, wind, geothermal resources and etc. for the sake of human demand. For that a solar cell (SC) is a device that may be used in order to convert the energy of the sun light into electricity. The basic principles of solar cells are quite straight-forward: the sun light is absorbed in an absorber layer of the SC, free charge carriers are generated as a result of light absorption and then the charge carriers are collected. An absorber of good solar cell should have large absorption coefficient, appropriate band gap close as much as possible to a band gap predicted by Shockley-Queisser limit for single-junction SCs, should be non-toxic, abundant, sustainable, stable at various environment conditions, and as defect-free as possible.

Silicon is the most commercially used material in the solar cell market due to its many outstanding properties: it is abundant, non-toxic and is obtained by well-known manufacturing processes[1]. The current record efficiency of silicon-based SCs has overcome 26 % [NREL, efficiency chart: https://www.nrel.gov/pv/cell-efficiency.html]. However, alongside with all advantages, the silicon possesses relatively low absorption coefficient coming from indirect band gap of the material[2] that requires to use much material and increases the thickness of the absorbing layer in SC. Moreover, the manufacturing of pure (non-defect and non-impurity) silicon is an expensive process that may ultimately limit the final prices of solar modules[1].

To overcome these issues related to Si-based SCs, a variety of materials was found for application in thin film photovoltaics, such as amorphous silicon (a-Si), cadmium telluride (CdTe), copper indium gallium selenide (CIGS). The possibility of cheap production compared to silicon based SCs together with high absorption coefficient favors the drastic reduction of amount of the material used in SC and thus potentially lower cost. However, so far these materials reveal lower power conversion efficiency (PCE) in part because of the presence of grain boundaries and high defects concentrations[1].

Therefore, the attempts were undertaken to discover the materials that could combine low cost production as well as would deliver high efficiencies. Relatively recently in 2009 the metal halide perovskites have shown themselves as a promising material for this role for application in thin film photovoltaics.

The perovskites were discovered in 1839 and named after Russian meteorologist Lev Perovski. The perovskite material has a structure that can be described by the chemical formula ABX_3, where *A* and *B* are cations and *X* is an anion. The first studies of metal halide perovskites (MHP) are dated back to 1958[3], when the photoconductive response in $CsPbX_3$ was observed. However, real large interest in photovoltaics applications the perovskites started just a decade ago.

The growth of the photoconversion efficiency of the perovskite-based SCs has been tremendous just within a decade of active research in these materials. The first perovskite-based SC was built according dye-synthesized technology and had an efficiency of a bit above 3%[4]. The current record efficiency of perovskite SCs has already overcome 25 % [NREL chart: https://www.nrel.gov/pv/cell-efficiency.html] and is comparable to commercialized Si-based SCs efficiencies. The tremendous success of perovskites is, on one hand, due to enormous progress in chemical engineering, but, on another hand, is due to outstanding electronic and optical properties of this material.

Among the remarkable optoelectronic properties one can account for an appropriate for SCs band gap, that can be tuned by composition[5], simple and cheap manufacturing processes[6], long charge carriers diffusion length[7,8], moderate mobility[9], low trap state densities[10,11], long lifetimes[7] and large absorption coefficient[12,13]. However, along with these advantages, the metal-halide perovskites suffer from a lack of chemical stability under exposure to moisture, reveal light-induced phase segregation[14] and are toxic due to use of lead.

The several approaches were proposed in order to overcome the issues related to chemical stability of metal halide perovskites. The first one is related to composition modification of the perovskites materials by replacing or mixing the cations and halides[15,16]. Another approach is based on intercalation of the large bulky hydrophobic organic cations, that slice the perovskite structure and reduce the dimensionality of the perovskite into two-dimensional perovskite structure[17]. Alternatively, the stability can be enhanced by development of appropriate encapsulation techniques[18].

One of the key parameters that plays an important role in SC operation is mobility of the absorber material[19]. The charge carrier mobility in MHPs is relatively modest compared to many standard compound semiconductors like GaAs or InP. The reported mobility values are in the range from 0.1 to 40 $cm^2V^{-1}s^{-1}$ depending on the composition of perovskites, its dimensionality and the measurements technique[9]. Different approaches were introduced to explain the relatively low mobility in MHPs at room temperatures, including polaron

formation[20,21], scattering at optical and acoustic phonons[22,23], dielectric drag[24], Rashba effect[25], dynamic disordering[26] in three-dimensional perovskites, exciton formation in two and one-dimensional perovskites. However, none of the applied theories has clearly explained the observed modest mobility values in MHP.

This thesis is dedicated to investigation of charge carrier transport and dynamics in three-, two-dimensional and nanocrystalline MHPs thin films characterized by THz Spectroscopy and consists of six chapters..

Chapter 2 is dedicated to theoretical background of linear charge carrier transport theory based on relaxation time approximation and includes the theory of charge carrier scattering at optical and acoustic phonons, charged and neutral impurities as well as basics of polaron theory and exciton formation theory.

THz Spectroscopy, or Optical Pump THz Probe Spectroscopy (OPTP), is a contact free technique and yields the sum of electron and hole mobility within grains (intra-grain mobility). The THz set-up, used in this work, principles of THz pulse generation and detection as well as the data analysis with the models interpreting the measured data are introduced in chapter 3.

Chapter 4 deals with charge carrier transport in three-dimensional polycrystalline $MAPbI_3$, $(Cs,FA)PbI_3$ and $(Cs,FA,MA)Pb(I,Br)_3$ thin films, prepared by S. Zhang and Dr. M. Stolterfoht in the research group Prof. Dr. D. Neher at the Potsdam University and $CsPbI_3$, prepared by Dr. P. Becker in the group of Dr. T. Unold at Helmholtz Zentrum Berlin. Charge carrier mobility spectra in the frequency range from 0.5 to 2.5 THz are shown and analyzed by the modified Drude-Smith model. Furthermore, the mobility spectra in $MAPbI_3$ are analyzed in a broad range of temperatures from 10 K to 295 K. The calculation of electron and hole mobility scattered at polar optical and acoustic phonons, charged and neutral impurities is performed as a function of temperature as well as impact of exciton formation on charge carrier mobility is discussed. The scattering mechanisms are discussed in details in a broad range of temperatures with the main focus on low temperature mobility. Finally, the impact of cations on charge carrier mobility at various temperatures is discussed.

Two-dimensional perovskites have emerged as an appropriate material class to enhance the chemical stability in MHPs. However, the power conversion efficiency of two-dimensional perovskites-based solar cells is still lower than in the most three-dimensional perovskites SCs mostly due to poor charge carrier transport properties because of quantum and dielectric confinement. Chapter 5 is dedicated to charge carrier mobility spectra analysis in two-

dimensional perovskites thin films $BA_2MA_{n-1}Pb_nI_{3n+1}$ with n =2-4 prepared by hot-casting technique and provided by S. Zhang from the research group Prof. Dr. D. Neher at Potsdam University. Finally, the photoconductivity transients are shown and the charge carrier dynamics in these thin films is discussed.

Another new emerging class of perovskites are colloidal nanocrystalline MHPs that possess high photoluminescence quantum yield (PLQY). However, similar to two-dimensional MHPs, the nanocrystalline MHPs suffer from relatively low PCE due to poor nanocrystal coupling. The charge carrier mobility spectra for nanocrystalline MHPs thin films are shown in the final experimental chapter 6. The nanocrystalline MHPs with nanocrystal of size 8-20 nm were prepared by hot-injection technique by Martin Kaergel in the group of Dr. T. Unold and underwent post-production treatments in order to increase the coupling between the nanocrystals. The influence of post-treatment processes on the charge carrier mobility and dynamics in these thin films are studied in detail.

2. Charge carrier transport theory

2.1. Introduction

While moving in the crystal the free (mobile) charge carriers undergo scattering at atoms. If there is no any electric field, the charge carriers randomize their momentum after collisions and there is no any directed motion of charge carriers in the crystal (no current). If an electric field E is applied in the crystal, then charge carriers move with drift velocity proportional to the applied electric field: $v_d = \mu E$ where μ is mobility of charge carriers. Mobility has a simple relation to the scattering time τ – average time between collisions, $\mu = e/m \cdot \tau$, where m is effective mass and e electron charge.

The charge carrier scattering in the crystal are associated with scattering at phonons, at charged or neutral impurities, or at other electrons and holes at high charge carrier densities. The scattering implies the change of the momentum from a momentum state $\boldsymbol{k}$ to a state $\boldsymbol{k}'$ accompanied with energy conservation (elastic scattering) or loss of part of the energy (inelastic scattering).

The phonons in the lattice are associated with collective motion of the atoms in the lattice. One may distinguish between optical and acoustic phonons. The optical phonons are associated with vibrating dipoles in polar materials, while the acoustic phonons are in turn associated with deformation of the lattice due to thermal motion of the atoms. In polar materials the charge carrier may induce strain in the crystal due to electrostatic interaction with dipoles. The self-induced strain has piezoelectric nature and it is associated with acoustic phonons that interact with charge carriers via piezoelectric potential. The scattering at polar optical phonons has electrostatic nature and scattering occurs in inelastic way, i.e. with partial loss of energy. Due to low energy of acoustic phonons, the scattering at acoustic phonon is often considered as (quasi-) elastic.

Alongside with scattering at phonons, in polar materials with low energy optical phonons the charge carrier may become coupled to these low energy optical phonons and create a polaron. Furthermore, in the material with low dielectric constants the electrons and holes may create a bound state-exciton. The formation of various quasiparticles like polarons or excitons may in general influence the charge carrier transport.

The scattering at impurities may occur at charged impurities by means of Coulomb interactions and at neutral impurities by means of weak interactions. Since the mass of impurities is much larger than a mass of the charge carriers, the scattering at impurities is elastic.

The interaction of charge carriers at other charge carriers occur by means of electrostatic interactions only if the distance between the charge particles is sufficient to have an impact on each other. Thus, this scattering mechanism is important at very high densities of the charge carriers.

Regardless of the scattering mechanisms, the scattering limits the transport in the materials and thereby reduces the mobility. Mobility is proportional to the momentum relaxation time of a particle τ, that in turn depends on the probability of a particle undergo a transition from a momentum state k to a state k'. In general the dependency of scattering time on the transition probability cannot be obtained analytically and requires solution of the Boltzmann transport equation, which describes the evolution of the system (charge carrier distribution function) after perturbation. However, assumptions of the linear transport and average momentum relaxation approximation simplify the relation between scattering time and transition probability simplifies: scattering time is inverse proportional to the transition probability that can be determined from the Fermi Golden rule if the scattering Hamiltonian is known.

This chapter deals with description of different mechanisms of scattering and its influence on temperature dependent charge carrier mobility that is further used to calculate the mobility in this thesis. This chapter is based on the following books on charge carrier transport in semiconductors: Jacoboni *Theory of electron transport in semiconductors*[27]; Ridley, "*Quantum Processes in Semiconductors"*[28]; Yu, "*Fundamentals of Semiconductors"*[29]; the polarons theory section is based on Devreese, *"Polarons"*[30] and Devreese, Alexandrov *"Froehlich polaron and bipolaron: recent developments"*[31]; The exciton section is based on the following reviews: Katan etal., "*Dielectric and Quantum Confinement Effects in Lower-Dimensional Metal Halide Perovskites*"[32] and Marongiu et al., "*The role of excitons in 3D and 2D in lead halide perovskites*" [33].

2.2. Boltzmann transport equation within linear transport

Boltzmann equation

Boltzmann transport equation describes the evolution of the system in the non-equilibrium state. The state of such a system is described by the distribution function $f(\boldsymbol{k}, \boldsymbol{r}, t)$ that defines the probability of occupation of a state $\boldsymbol{k}$ with energy E_k. The distribution function is in general a function of a particle position $\boldsymbol{r}$, momentum $\boldsymbol{k}$ (velocity $\boldsymbol{v}$) and time t.

In equilibrium state in the absence of external forces, the electrons and holes obey the Fermi-Dirac distribution:

$$f_{FD} = \frac{1}{\exp\frac{E - E_F}{kT} + 1} \tag{2.1}$$

where E_F is a Fermi energy, T is a temperature and k is the Boltzmann constant.

However, if the electron (hole) gas is perturbed by some external forces, the distribution function changes in time. There are three processes that account for a change of the distribution function:

1. Diffusion – charge carriers move into and out of the considered volume in r and k –space.
2. Applied external field that forces the charge carriers to change their momentum.
3. Scattering – collision with other particles, e.g. atoms, impurities, phonons, other charged particles with a change of momentum state from k to another momentum state k'.

Then the total change in the distribution function represents the sum of contributions due to each of these three processes:

$$\frac{df}{dt} = \left(\frac{\partial f}{\partial t}\right)_{diff} + \left(\frac{\partial f}{\partial t}\right)_{field} + \left(\frac{\partial f}{\partial t}\right)_{scatt} \tag{2.2}$$

In case of steady state $\frac{df}{dt} = 0$ and then the sum of diffusion, field and scattering terms is equal to zero. In case of perturbed system $\frac{df}{dt} \neq 0$.

By considering the partial derivatives for each of the processes one may obtain the following formula[27]:

$$\frac{df}{dt} = -\boldsymbol{v} \cdot \boldsymbol{\nabla}_{\boldsymbol{r}} f - \dot{\boldsymbol{k}} \cdot \boldsymbol{\nabla}_{\boldsymbol{k}} f + \left(\frac{\partial f}{\partial t}\right)_{scatt} \tag{2.3}$$

where $\boldsymbol{v}$ is a velocity of a particle, $\boldsymbol{k}$ is its momentum, the first term on the right in the *equation (2.3)* represent the change of the distribution function due to diffusion, and the second one is due to applied external forces. The *equation (2.3)* represents the Boltzmann transport equation.

In order to define the scattering term in *equation (2.3)* we should introduce the probability $P(k', k)$ of a particle to undergo a transition from a momentum state *k* to another unoccupied momentum state k'. If $f_{k'}$is a number of charge carriers in k' state, then a number of available state is $1 - f_{k'}$ and the total probability of a charge carrier scatters from momentum state *k* to a momentum state k': $\int P(k, k')(1 - f_{k'})dk'$. If the total number of electrons in a state *k* is equal to f_k, then the total number of electrons scattered from state *k* to a momentum state k' is equal to $f_k \int P(k, k')(1 - f_{k'})dk'$. The reverse process of scattering from a state k' to a state *k* is also possible. Applying the same approach, the total number of charge carriers scattered into a state *k* from a state k' is equal to $(1 - f_k) \int f_{k'} P(k', k)\, dk'$. By taking into account the difference in number of charge carriers scattered into and out of volume dk', the scattering term is given by[27]

$$\left(\frac{\partial f}{\partial t}\right)_{scatt} = \frac{V}{(2\pi)^3} \int [f_{k'} P(k', k)(1 - f_k) - f_k P(k, k')(1 - f_{k'})]\, dk' \tag{2.4}$$

This integral expression is known as collision integral. The factor $(2\pi)^3$ comes from the definition of density of states in *k*-space and *V* donates the volume, resulting from density of states.

The probability $P(k', k)$ can be in turn determined from Fermi's golden rule by knowing the scattering Hamiltonian $\widehat{H}_{scatt}$:

$$P(k', k) = \frac{2\pi}{\hbar} \left|\langle k' | \widehat{H}_{scatt} | k \rangle\right|^2 \rho(E_k) \tag{2.5}$$

However, it is important to note that such an approach to calculate the probability of transition from one state to another is valid only at sufficiently high momentum relaxation times between collisions.

As seen above, the Boltzmann transport equation is a differential equation containing an integral and in most cases can be solved only numerically. This makes transport analysis for particular scattering mechanisms difficult. However, making linear transport and average time approximations one can obtain the analytical expressions for mobility.

Linear transport approximation

The linear transport approximation is based on the assumption that external forces, perturbing the electron gas from an equilibrium state, are small enough. Then perturbed distribution function f_k can be expanded to the first order of perturbation[27,29]:

$$f_k = f_k^0 + g_k \tag{2.6}$$

where f_k^0 may be regarded as Fermi-Dirac distribution or Maxwell distribution for non-degenerate gas and g_k is the expansion term of the first order, dependent on the applied Force $\boldsymbol{F}$.

Momentum relaxation time approximation

The collision integral *(2.4)* can be approximated as a g_k divided by momentum relaxation time τ that is in general dependent on energy[27]:

$$\left(\frac{\partial f}{\partial t}\right)_{scatt} \approx -\frac{g_k}{\tau} \tag{2.7}$$

The *expression (2.7)* constitutes the momentum relaxation time approximation. The collision integral vanishes in the Boltzmann *equation (2.3)* within momentum relaxation time approximation.

The momentum relaxation time approximation implies that if the force $\boldsymbol{F}$ is applied to distribution function f_k and brings it out of equilibrium, then when the force is removed, the distribution function will relax to its equilibrium with some relaxation time as:

$$g_k(t) = g_k(0)\exp\left(-\frac{t}{\tau}\right) \tag{2.8}$$

Equation (2.8) can be simply obtained by substitution of linear transport approximation *(2.6)* into *equation (2.7).* The time derivative of steady state distribution function $\left(\frac{\partial f_k^0}{\partial t}\right)_{scatt} = 0$ and solution of differential *equation (2.7)* yields exponential decay $g_k$that represents change of the equilibrium distribution function after perturbation.

Elastic scattering

The momentum relaxation time approximation simplifies the relation between the scattering rate $1/\tau$ and the probability of transition. Within the momentum relaxation time, an

approximation of the scattering rate can be simply obtained by knowing the probability of scattering of charge carriers from a state *k* to an unoccupied state k'. If the initial momentum state is *k*, the final momentum state k', the scattering angle between *k* and k' is equal to θ, and the scattering occurs with conservation of energy. Then the scattering rate $1/\tau$ within momentum relaxation time approximation is given by[34]

$$\frac{1}{\tau} = \int P(k', k)(1 - \cos\theta)dk' \qquad (2.9)$$
$$= \frac{2\pi}{\hbar}\int |M_{kk'}|^2 \rho(E - E_k - E_{k'})(1 - \cos\theta)dk'$$

The equation after the equality sign takes into account the Fermi's golden rule for probability $P(k', k)$ with transition matrix elements $|M_{kk'}|$. As it is seen from *equation (2.9)* that the forward scattering $\theta \approx 0$ results in very low scattering rates (almost zero) and to high extent the scattering at high scattering angles θ contribute to the scattering, e. g. backward scattering.

The scattering can be regarded elastic for scattering at impurities due to their heavier masses compared to the masses of charge carriers and the scattering at acoustic phonons due to phonons low energies.

Inelastic scattering

If the scattering occurs with change of momentum and of the energy (inelastic scattering), then the scattering rate $1/\tau$ cannot be determined so straightforward from the probability of the transitions. In this case, the scattering rate within the momentum relaxation time approximation time is written as [34]

$$\frac{1}{\tau} = \int P(k', k)\left(1 - \frac{g_{k'}}{g_k}\frac{f_k^0}{f_{k'}^0}\right)dk' \qquad (2.10)$$

The charge carriers undergo inelastic scattering at optical phonons as the latter ones have considerable energy.

Average momentum relaxation time and mobility

If we know the scattering rate $1/\tau$ from the probability that charge carriers undergo a transition from one to another momentum state, then the effective scattering time, reverse to scattering rate, can be found by averaging all scattering times in energy E_k as follows

$$\tau_{eff} = \frac{\int \tau(E_k) E_k f(E_k) dE_k}{\int f(E_k) dE_k} \tag{2.11}$$

If the charge carrier gas is non-degenerate, then Boltzmann distribution can be taken as a distribution function $f(E) = \exp\left(-\frac{E_k}{kT}\right)$.

By knowing the effective, or average, scattering time the mobility can be found simply as a product of electron charge carrier and effective scattering time divided by effective mass of charge carrier in the material of interest.

$$\mu = \frac{e\tau_{eff}}{m} \tag{2.12}$$

The dependence of the distribution function on temperature *T* allows finding the dependency of mobility on temperature that is specific for various scattering processes at phonons, impurities and the alloys.

To sum up, considering the linear transport approximation and the momentum relaxation time approximation simplifies, to high extent, the solution of the scattering problem of charge carriers. In the most cases, the problem of charge carrier transport reduces to calculation of scattering rates and mobility by knowing the transition probability for particular scattering mechanism. In addition, other assumptions are often considered such as band structure, inter- or intra-valley scattering, elastic or inelastic scattering and etc.

In the next sections of this chapter, a detailed description of the scattering mechanisms will be given and the mobility for scattering at optical and acoustic phonons and impurities will be described taking into account these approximations without detailed solving the Boltzmann equation.

Polar optical phonons

The phonons are associated with collective motions of atoms at the lattice nodes in the crystal. In case of polar materials, the charge is non-uniformly distributed within the lattice cell even in the absence of an electrical force, i. e. there are parts of the cell with positive and negative charges and the lattice cell has a dipole moment, but the charge is in total balanced and the charge of the lattice cell is zero. The collective motion of the atoms in this case can be regarded as vibrations of dipoles at the lattice nodes and such vibrations are associated with polar optical phonons. The electrostatic interaction of mobile charge carriers in the crystal with vibrating diploes at the nodes is regarded as scattering at polar optical phonons.

The energy of the optical phonons is in the range of a few tens of meV[35] for many compound semiconductors and the free charge carriers in the crystal undergo inelastic scattering at polar optical phonons with a change of energy after scattering. Since the thermal energy *kT* is around 25 meV at room temperature, the scattering at optical phonons is efficient at room temperatures. It makes the scattering at optical phonons dominating for many standard semiconductive compounds like GaAs. As temperature goes down, the optical phonon population decreases, which lowers the chance for free charge carriers to emit or absorb a phonon at low temperatures and thereby limits the scattering at optical phonons.

The probability of scattering at polar optical phonons depends on static ε and high-frequency ε_∞dielectric constants, effective mass of charge carriers m and the energy of optical phonons $\hbar\omega_{LO}$ and is given by[27]

$$P(k,k') = \frac{\pi e^2}{V}\omega_{LO}\left[\frac{1}{\varepsilon_\infty}-\frac{1}{\varepsilon}\right]\binom{N_{LO}}{N_{LO}+1}\mathcal{G}\left(\frac{q}{q^2+q_0^2}\right)^2 \times \delta(E_{k'}-E_k \mp \hbar\omega_{LO}) \tag{2.13}$$

where e is the electron charge, N_{LO} is a phonon population density, that is taken in case of absorption of phonons and $N_{LO}+1$ – the factor that is taken in case of emission of phonons, $\mathcal{G}$ is an overlap integral, $\mathcal{G}$ is an overlap integral that is in general dependent on scattering angles, q is an optical phonon momentum, q_0 is an inverse screening length and $\delta(E_{k'}-E_k \mp \hbar\omega_{LO})$ shows the energy conservation after scattering.

Unlike to scattering at acoustic phonons, while scattering at optical phonons a charge carrier undergoes a change of its kinetic energy but the minor change of momentum, i. e. forward scattering is favored. In this case, the total scattering rate, defined by *equation (2.10)*, is equal to zero – no momentum relaxation time. Therefore, the mobility and average scattering time cannot be described within the momentum relaxation time approximation, described above in the previous section, and the solution of Boltzmann equation is required for the case of scattering at polar optical phonons.

However, the characteristic mobility expression for polar optical phonon was obtained by Stratton[36] and then by Conwell[37] by applying the scattering rates in a drifted Maxwell distribution:

$$\mu_{LO} = \frac{3(2\pi\hbar\omega_{LO})^{1/2}}{4m^{\frac{1}{2}}E_\circ n(x_\circ)(x_\circ)^{\frac{3}{2}}e^{\frac{x_\circ}{2}}K_1(x_\circ/2)} \tag{2.14}$$

where $E_\circ = \frac{me\hbar\omega_{LO}}{4\pi\varepsilon_0\hbar^2}\left[\frac{1}{\varepsilon_\infty}-\frac{1}{\varepsilon}\right]$, ,$\varepsilon_0$ – vacuum permittivity, $x_\circ = \frac{\hbar\omega_{LO}}{kT}$ and $n(x_\circ) = \frac{1}{e^{x_\circ}-1}$ - Bose-Einstein distribution and $K_1(x_\circ/2)$ – Bessel function.

The detailed description of application of *equation (2.14)* is given for perovskites in **chapter 4** of this thesis and it is shown there how the incoming parameters influence the mobility in a broad range of temperatures.

Acoustic phonons

In-phase movements of atoms in the lattice are associated with acoustic phonons. There are two distinctive mechanisms of charge carriers interaction with acoustic phonons: interaction via the **deformation potential** and via the **piezoelectric potential.** The acoustic phonons related to the deformation potential are associated with deformation of the lattice resulted from the thermal vibrations of the atoms. In polar crystals with a lack of inversion symmetry, the deformation of the lattice due to thermal vibrations results in the self-induced strain that is associated with acoustic phonons of the piezoelectric potential, i. e. both mechanisms of scattering exist simultaneously in polar crystals.

The energy of acoustic phonons is in the range of a few meV[29]. Such relatively low energies of acoustic phonons result in a large phonon population and significant scattering with charge carriers even at low temperatures. Therefore, the scattering at acoustic phonons is often dominating at low temperatures. For the reason of low energy of acoustic phonons, the scattering occurs with a very small change of energy, therefore, acoustic scattering is considered as quasi-elastic.

The scattering probability at acoustic phonons of deformation potential is given by[27]:

$$P(k,k')_{AD} = \frac{2\pi kTE_1^2}{\hbar V\rho v_s^2}\delta(E_{k'}-E_k) \tag{2.15}$$

where E_1- deformation potential, $\hbar$ – Plank constant, k – Boltzmann constant, ρ– mass density, v_s – speed of light in the material and m – effective mass of a charge carrier.

The further integration of probability over all possible scattering states k' by *equation (2.9)* yields the scattering rate $1/\tau$, and then the average relaxation time and mobility can be determined by *equations (2.11)* and *(2.12)*, respectively [27,28]

$$\mu_{AD} = \frac{2^{\frac{3}{2}}\pi^{\frac{1}{2}}e\hbar^4\rho v_s^2}{3m^{\frac{5}{2}}E_1^2}(kT)^{-\frac{3}{2}} \tag{2.16}$$

The scattering probability for acoustic phonons of piezoelectric potential is as follows[27]:

$$P(k,k')_{AP} = \frac{2\pi kTe^2p^2}{\varepsilon^2\hbar V\rho v_s^2}\left(\frac{q}{q^2+q_0^2}\right)^2\delta(E_{k'}-E_k) \tag{2.17}$$

where $p-$ piezoelectric coefficient, ε is a static dielectric constant, q- acoustic phonon momentum and q_0- inverse screening length.

The charge carrier mobility on acoustic phonons of piezoelectric potential is given by [27,28]

$$\mu_{AP} = \frac{16\sqrt{2\pi}}{3}\frac{\varepsilon_0^2\varepsilon^2\hbar^2\rho v_s^2}{p^2em^{\frac{3}{2}}F_{PE}(T,n_e,\varepsilon,m)}(kT)^{-\frac{1}{2}} \tag{2.18}$$

where $F_{PE} = 1-\frac{\epsilon_0}{4kT}\lg\left(1+\frac{8kT}{\epsilon_0}\right)+\frac{1}{1+8kT/\epsilon_0}$, where $\epsilon_0 = \frac{\hbar^2e^2\,n_e}{2m\varepsilon kT}$. The factor F_{PE}depends on temperature T, dielectric constant ε, electron effective mass m and electron density n_e in conductance band. This factor can be regarded as a constant in a broad range of temperatures.

The comparison of the mobility behavior for the two mechanisms of scattering at acoustic phonons reveals two distinct power-law dependencies on temperature: the scattering at acoustic phonon has more steep decay with temperature $\mu_{AD}\sim T^{-3/2}$ while the scattering at acoustic phonons of piezoelectric potential $\mu_{AP}\sim T^{-1/2}$.

Impurity scattering

The scattering may occur at charged or neutral impurities. Due to large masses of impurities in the crystal, the scattering of charge carriers can be regarded as elastic and the scattering rate may be calculated from *equation (2.9)* by knowing the scattering potential at impurities.

Charged impurity. The scattering at charged impurities occurs by means of electrostatic Coulomb interactions with the scattering potential

$$V = \frac{ze^2}{4\pi\varepsilon_0\varepsilon r} \tag{2.19}$$

where z is a charge number of an impurity.

However, this potential does not take into consideration the screening effect from the rest of electrons in the surrounding of the impurity atoms (ions). Brooks and Herring[27] proposed more general approach, based on solution of charge carriers scattering problem at Yukawa potential, that take into account the screening effect and it is given by

$$V = \frac{ze^2 \cdot \exp[-q_0 r]}{4\pi\varepsilon_0\varepsilon r} \tag{2.20}$$

where $q_0 = \sqrt{\frac{e^2 n_e}{\varepsilon_0 \varepsilon kT}}$ is an inverse screening length and n_e is the charge carrier concentration. The probability to be scattered from a state k to a state k', obtained from the Fermi's golden rule with given above the scattering potential, is given by[27]

$$P(k,k') = \frac{2\pi}{\hbar} n_{II} \frac{z^2 e^2}{\varepsilon_0^2 \varepsilon^2 V} \frac{1}{[q^2 + q_0^2]^2} \mathcal{G}\delta(E_{k'} - E_k) \tag{2.21}$$

where $z -$ charge number, $n_{II} -$ ionized impurity density.

The further integration over the states k' and the averaging over the energy, gives the mobility for Brooks-Herring method that is as follows[28]

$$\mu_{BH} = F_{BH}(T, n_I, \varepsilon, m, n_e) \frac{64\sqrt{\pi}\varepsilon_0^2 \varepsilon^2}{n_I z^2 e^3 \sqrt{m}} (2kT)^{\frac{3}{2}} \tag{2.22}$$

where the factor $F_{BH} = \log(1+\xi) - \frac{\xi}{1+\xi}$ where $\xi = \frac{24 m \varepsilon_0 \varepsilon (kT)^2}{\hbar^2 e^2 n_e}$ depending on temperature T, dielectric constant ε, effective mass m and excited charge carriers concentrations n_e.

Neutral impurity. The scattering at neutral impurities is often neglected due to weak interactions of charge carriers with neutral impurities. There are many approaches to calculate the electron mobility scattered at neutral impurity[28]. One of the pioneers was Erginsoy[28]. He considered the scattering of electrons with effective mass m at neutral hydrogen-like impurities and showed that the average relaxation time of charge carriers reversely depends on neutral impurity density n_{NI} and is constant with temperature[28]:

$$\tau_E = \frac{e^2 m^2}{80\pi\varepsilon_0 \varepsilon \hbar^3 n_{NI}} \tag{2.23}$$

Another approach was proposed by Sclar[38]. According to his approach, a charge carrier becomes trapped into a state E_T by neutral impurity and a problem of scattering at neutral impurity was considered as scattering at square-well potential. The average momentum relaxation time is [28]

$$\tau_S = \frac{m^{3/2}}{2^{3/2}\pi\hbar^2 n_{NI}}\left(\frac{E_k + E_T}{\sqrt{E_k}}\right) \tag{2.24}$$

where E_k is an electron kinetic energy, E_T is the trapping energy – energy, required for an electron to be added to neutral Hydrogen atom. This trapping energy can be estimated empirically from equation $E_T = 0.75\frac{m}{\varepsilon}$ [eV], where *m* is effective mass of a charge carrier in electron mass units m_0 and ε is dielectric constant[28].

The temperature dependency of Sclar mobility can be given by [38,39]

$$\mu_S = 0.82\mu_E\left[\frac{2}{3}\left(\frac{kT}{E_T}\right)^{\frac{1}{2}} + \frac{1}{3}\left(\frac{E_T}{kT}\right)^{\frac{1}{2}}\right] \tag{2.25}$$

where $\mu_E$is Erginsoy mobility obtained by integration over energy E_k in *equation (2.11).* As seen from the *equation (2.25),* the Sclar mobility represents a product of Erginsoy mobility and the temperature dependent term. Therefore, the equation can be regarded as temperature dependent extension of Erginsoy approach of scattering at neutral impurities. At high temperatures the mobility depends on temperature as $\mu_S \propto T^{0.5}$.

It is important to point out that charge carrier mobility at impurities increases with temperature, which is opposite to the behavior due to scattering at optical or acoustic phonons. Band transport implies that charge carriers while moving in the crystal undergo collisions at atoms (atomic nodes). Since the phonon density is increasing with increase in temperature, the collisions are happening often and the mobility is decreasing. The increasing mobility with temperature is similar to a hopping behavior when the charge carriers jump off one localized site to another with help of thermal energy that serves as an activation energy. Moreover, the temperature dependencies for charged and neutral impurities show different power law dependency on temperature. The scattering at charged impurities have $\sim T^{1.5}$ while the neutral impurities shows a more modest increase $\propto T^{0.5}$.

2.3. Matthiessen rule

Usually many scattering mechanisms are involved simultaneously. If we regard the scattering mechanisms at polar optical, acoustic phonons of deformation and of piezoelectric potentials, scattering at charged and neutral impurities, then the total mobility is defined by the Matthiessen rule as follows[27]:

$$\frac{1}{\mu_{tot}} = \frac{1}{\mu_{LO}} + \frac{1}{\mu_{AD}} + \frac{1}{\mu_{AP}} + \frac{1}{\mu_{II}} + \frac{1}{\mu_{NI}} \tag{2.26}$$

2.4. Polaron

As we know from the optical phonons section, the polar optical phonons are associated with collective motions of dipoles (atoms with non-zero dipole moment in polar crystal) in the lattice nodes. If the energy of those vibrations is sufficiently low, then a free electron, while moving in the crystal, may polarize the surrounding medium (atoms, dipoles) near itself and an electron may become coupled to low energy phonon modes, associated with dipole vibrations. An electron surrounded by phonon clouds is called a large polaron. Polaron formation was predicted by Landau in 1933 and the interaction of electrons with low energy optical phonons was studied by Fröhlich in 1954 for the first time. He considered the following Hamiltonian for electrons[30,31]:

$$H = -\frac{\nabla^2}{2m} + \sum_{\boldsymbol{q}} \omega_{\boldsymbol{q}}\left(a_{\boldsymbol{q}}^{\dagger} a_{\boldsymbol{q}} + 1/2\right) + \sum_{\boldsymbol{q}} \left(V_{\boldsymbol{q}} a_{\boldsymbol{q}} e^{i\boldsymbol{q}\cdot\boldsymbol{r}} + h.c.\right) \tag{2.27}$$

where the first term is Hamiltonian for free electrons, the second is for phonon with phonon population density $n_q = a_{\boldsymbol{q}}^{\dagger} a_{\boldsymbol{q}}$, where $a_{\boldsymbol{q}}^{\dagger}$ and $a_{\boldsymbol{q}}$ are annihilation and creation operators, and the third term is an interaction potential between electrons and phonons.

The potential $V_{\boldsymbol{q}}$was obtained based on the following assumptions[30]: 1) the polaron extension is larger than the lattice parameters; 2) spin and relativistic effects are neglected; 3) there is a parabolic electron band; 4) the energy of LO phonons is sufficiently low.

The potential $V_q \propto (4\pi\alpha/V)^{0.5}$, where α is a Fröhlich coupling constant, that shows the strength of electron-phonons coupling (interaction)[30]:

$$\alpha = \frac{1}{8\pi\varepsilon_0}\left(\frac{1}{\varepsilon_\infty} - \frac{1}{\varepsilon}\right)\frac{e^2}{\hbar\omega_{LO}}\sqrt{\frac{2m\omega_{LO}}{\hbar}} \tag{2.28}$$

where ε, ε_∞ are static and high-frequency dielectric constants, $\hbar\omega_{LO}$ is LO phonons energy, m is an electron(hole) effective mass.

Depending on values α, the polaron can be distinguished as a large polaron ($\alpha \approx 1-2$) or small polaron ($\alpha \gg 1$). The large polaron is spread over many lattice cells (sites) and may regarded as a free electron with enhanced effective mass called polaron effective mass that is within weak coupling can be given by:

$$m_p = m\left(1 + \frac{\alpha}{6}\right) \tag{2.29}$$

Small polaron in turn is strongly localized within a single lattice cell and reveals a hopping-like transport behavior. This results in specific behavior of mobility with temperature: mobility of large polarons decreases with increase in temperature $\frac{\partial\mu}{\partial T} < 0$ and vice versa for small polaron $\frac{\partial\mu}{\partial T} > 0$.

All coupling theory (Feynman theory)

The Fröhlich Hamiltonian describes the large polaron behavior within weak coupling regime when $\alpha\sim1$. In early 1960s, Feynman has developed more general theory of large polarons that covers all possible interaction regimes, therefore, it is often called all coupling theory.

The Feynman's approach was based on solution of path integral, introduced by Feynmam himself. The path integral was supposed to determine the evolution of the ground state of the system. If a ground state of the system is defined as $|0,0\rangle$ then a change in the ground state $|0,\tau\rangle$ in time τ will be given by[31]

$$\langle 0,\tau|0,0\rangle = \int \mathcal{D}\boldsymbol{r}(\tau)e^{-S(\boldsymbol{r},\dot{\boldsymbol{r}},\tau)} \tag{2.30}$$

where $S(\boldsymbol{r},\dot{\boldsymbol{r}},t)$ is an action functional that is defined via Lagrangian of the system $\mathcal{L}(\boldsymbol{r},\dot{\boldsymbol{r}},t) = T(\boldsymbol{r},\dot{\boldsymbol{r}},t) - U(\boldsymbol{r},\dot{\boldsymbol{r}},t)$: $S(\boldsymbol{r},\dot{\boldsymbol{r}},\tau) = \int_0^\tau \mathcal{L}(\boldsymbol{r},\dot{\boldsymbol{r}},t)dt$, $T(\boldsymbol{r},\dot{\boldsymbol{r}},t)$ and $U(\boldsymbol{r},\dot{\boldsymbol{r}},t)$ are kinetic energy and potential of the system, respectively. The *integral (2.30)* is called Feynman path integral.

Feynman has defined the action functional for free electrons, undergoing Coulomb interactions with surrounding environment [31]

$$S = \int_0^\tau \frac{\dot{\boldsymbol{r}}^2}{2} - \frac{\alpha}{2^{3/2}}\int_0^\tau\int_0^\tau \frac{e^{-|t-t_0|}}{|r(t)-r(t_0)|}dtdt_0 \tag{2.31}$$

The form of Coulomb potential should be understood as interaction of electron at time *t* with the electrostatic field induced by electron itself at the previous position at time t_0[31]. The first term represent a kinetic energy of a free electron. All the constants in *equation (2.31)* such as electron mass, charge and phonon energy are supposed to be equal to 1.

In order to find a bound energy of polaron, Feynman has introduced variation approach. Instead of true action *functional (2.31)* he used a trial action functional that was based on interaction of electrons with phonon clouds by means of harmonic oscillator with force constant *k* and the phonons were regarded as hypothetic particles of mass *M*. This trial action potential looks as follows[31]

$$S_0 = \int_0^\tau \frac{\dot{\boldsymbol{r}}^2}{2} - \frac{C}{2}\int_0^\tau\int_0^\tau |r(t)-r(t_0)|^2 e^{-w|t-t_0|}\,dtdt_0 \tag{2.32}$$

where *C* and *w* are variation parameters and the second term is a trial potential that represents harmonic potential. The relation between the variational parameters and force constant *k* and mass *M* can be written as $w = \sqrt{k/M}$, $k = 4C/w$ and $v^2 = w^2 + k$.

The variation parameters are varied in such a way that the error by using the trial action functional instead of the true one has a minor impact on upper bound energy for polaron ground state[31]:

$$E = E_0 - \lim_{\tau\to\infty}\frac{1}{\tau}\langle S - S_0\rangle \tag{2.33}$$

where E_0 is the energy of the ground state.

Polaron mobility

The different approaches were developed in order to derive the polaron mobility as function of temperature. All these techniques were obtained either within Feynman formalism or within Boltzmann transport equation and they have limitations depending on the coupling regime and temperature range.

One of the first who has found the polaron mobility was Feynman. He used his variation approach, based on path integral in 1962 and could estimate the impedance function from current, induced by alternating electric field. Following the Feynman approach, the polaron mobility is given by[40]

$$\mu_{FHIP} = \left(\frac{w}{v}\right)^3 \frac{3e}{4m_b} \frac{\exp(\beta)}{\omega_{LO}\alpha\beta} \exp\left[\frac{v^2 - w^2}{w^2 v}\right] \tag{2.34}$$

where $\beta = \hbar\omega_{LO}/kT$ is a ratio between the phonon energy $\hbar\omega_{LO}$ and thermal energy *kT*. The polaron mobility is valid for all coupling regimes but fails at low temperatures[20].

Alternatively, Kadanoff et al. [41] has applied Boltzmann transport equation for the Feynman polaron model and obtained the following expression for polaron mobility

$$\mu_K = \left(\frac{w}{v}\right)^3 \frac{e}{2m_b} \frac{\exp(\beta)}{\omega_{LO}\alpha} \exp\left[\frac{v^2 - w^2}{w^2 v}\right] \tag{2.35}$$

Kadanoff mobility for large polaron has limitations at low temperatures and may be exploited only for weak coupling regimes for low coupling constant α.

Relatively recently Hellwarth et al.[42] has derived the equation for polaron mobility that is valid also at low temperatures regardless of the coupling regimes (all coupling regimes).

$$\mu_H = \left(\frac{w}{v}\right)^3 \frac{3e}{m_b} \frac{\sinh(\beta/2)}{\omega_{LO}\alpha\beta^{5/2}} K^{-1} \tag{2.36}$$

where $K = \int_0^\infty du(u^2 + a^2 - b\cos(vu))^{-3/2}\cos(u)$ is polaron response to a change in driving force [20,31] $a^2 = (\beta/2)^2 + \left(\frac{v^2-w^2}{w^2 v}\right)^2 \beta\coth(\beta v/2)$ and $b = \left(\frac{v^2-w^2}{w^2 v}\right)^2 \frac{\beta}{\sinh(\beta v/2)}$.

2.5. Exciton

The bound state of electron and hole, attracted by Coulomb force, is called an exciton. The potential of interaction between holes and electrons is determined by the Coulomb potential[32]:

$$V(\boldsymbol{r}_e, \boldsymbol{r}_h) = -\frac{e^2}{4\pi\varepsilon|\boldsymbol{r}_e - \boldsymbol{r}_h|} \tag{2.37}$$

where $|\boldsymbol{r}_e - \boldsymbol{r}_h|$ is distance between an electron and hole, ε is dielectric constant and e is electron charge.

The dielectric properties of a material (the dielectric constant) have an enormous impact on exciton behavior. Lower values for the dielectric constant ε result in less sufficient screening of the electron and hole interaction and thereby results in stronger binding between electrons and holes. Depending on the strength of interaction between hole and electron one may distinguish between two types of excitons. Excitons with relatively strong coupling between electron and hole are called Frenkel excitons, while Wannier-Mott excitons are only weakly bound. The strength of interaction also influences how far electron and holes spread in the lattice. The size of Frenkel exciton is in the range of the size of a single lattice cell while Wannier-Mott exciton is spread over many lattice sites in the crystal.

The description of Wannier-Mott exciton is based on solving the Schrödinger equation for Hydrogen atom. Within this model an electron is considered to undergo the relative motion around the hole in the center of mass coordinate system. The Schrödinger equation for Wannier-Mott exciton, generalized for low dimensions $\alpha = 2, 3,$ is well known and is given by[32]:

$$\left[-\frac{\hbar^2}{2\mu\rho^{\alpha-1}}\frac{\partial}{\partial\rho}\left(\rho^{\alpha-1}\frac{\partial}{\partial\rho}\right) + \frac{l^2}{2\mu\rho^2} - -\frac{e^2}{4\pi\varepsilon\rho}\right]\Psi(\rho,\theta) = (E - E_G)\Psi(\rho,\theta) \tag{2.38}$$

where $\hbar$ is Planck constant, $\mu = (1/m_e + 1/m_h)^{-1}$is a reduced effective mass of exciton, $\rho = |\boldsymbol{r}_e - \boldsymbol{r}_h|$ and θ are polar coordinates, E_G is an energy gap of the material and l is angular momentum operator.

The discrete binding energies of excitons can be found after solving the Schrödinger *equation (2.38)* and they are given by [32]:

$$E_{b,n} = \frac{\mu}{\varepsilon^2} \frac{R_y}{\left(n + \frac{\alpha - 3}{2}\right)^2} \tag{2.39}$$

where n =1, 2, 3, …, α = 2, 3 is the dimension and R_y is Rydberg constant, which depends on dielectric permittivity of the material.

Quantum confinement

For an infinite extended semiconductor, the charge carriers occupy continuous energetic bands. However, if charge carriers are squeezed in dimensions comparable to Bohr radius, then the density of states changes and can become discrete in energy. The phenomenon of spatial confinement with resulted quantization of energy levels is known as quantum confinement.

The quantum confinement has an enormous impact on electronic and optical properties of the semiconductive materials, such as an increase of the band gap energy and the rise in the density of states with decrease of dimensionality. Furthermore, the charge carrier transport is lowered, the exciton binding energy increases, and the radiative recombination is enhanced[32].

Later in this thesis the charge carrier transport and dynamics in two-dimensional multilayered perovskites are studied, where one of the dimensions is confined. For layered materials, the effect of quantum confinement on the exciton binding energy is given by *equation (2.39)*. In this case the dimensionality α is regarded as function of layer thickness $\alpha = 3 - \exp(-L/a_B)$ [32], where a_B is Bohr radius and L is layer thickness. For thick materials, L is quite large, the exponential term in α can be neglected. However, in two-dimensional layered structures like multilayered 2D perovskites, the thickness of layers approaches the Bohr radius values and the exponential term should be taken into consideration. For such a case one the dimensionality α is between 2 and 3.

Dielectric confinement

Dielectric confinement occurs in layered structures when the layers have different dielectric constants. A neighboring layer with a lower dielectric constant results in less sufficient screening of the electron-hole interaction and thereby results in an increase of the binding energy of excitons in two-dimensional structures.

Similarly to quantum confinement, the dimensionality α can expressed as follows[43]:

$$\alpha = 3 - \gamma \exp(-L/a_B) \tag{2.40}$$

where γ is a factor responsible for dielectric confinement, $\gamma = 1$ if no dielectric confinement and $\gamma > 1$ if dielectric confinement is taken into account. If the thickness of layers is much larger than Bohr radius, then contribution from dielectric confinement is negligible.

Saha equation

In general excitons exist along with unbound electrons and holes. Relationship between the thermal energy *kT*, determined by temperature, and exciton binding energy defines the stability of the excitons. One of the requirements for stable existence of excitons is that thermal energy must be lower than exciton binding energy. If the thermal energy is higher than binding energy, then the exciton is likely to dissociate. Alongside with temperature and the exciton binding energy, the charge carrier concentration influences the fraction of excitons over free charge carriers. A larger concentration of photoexcited charge carriers results in a higher probability that electrons and holes meet each other and form an exciton. The Saha equation governs the equilibrium of free electron—holes pairs and excitons [33]:

$$\frac{\beta^2}{1-\beta} = \frac{n_{eq}}{n_{tot}} \tag{2.41}$$

where $\beta = n_{free}/n_{tot}$ is a fraction of free charge carriers to the total injected charge carriers n_{tot} and $n_{eq} = \left(\frac{m^* kT}{2\pi\hbar^2}\right)^{3/2} \exp\left(-\frac{E_b}{kT}\right)$ is a equilibrium concentration, where m^* is a reduced effective mass of exciton and E_b is a binding energy of exciton.

3. Experimental method and data analysis

3.1. Introduction

The Optical Pump THz Probe (OPTP) Spectroscopy is a unique technique that allows investigating the transport properties of charge carriers in the THz frequency range. Another often used name for OPTP Spectroscopy is time resolved THz Spectroscopy (TRTS). This chapter is based on several reviews on THz Spectroscopy applications: Ulbricht , *"Carrier dynamics in semiconductors studied with time-resolved terahertz spectroscopy"* [44]; Joyce, *"A review of the electrical properties of semiconductor nanowires: Insights gained from terahertz conductivity spectroscopy"* [45] and S. Dexheimer, *"Terahertz spectroscopy. Principles and Applications"* [46].

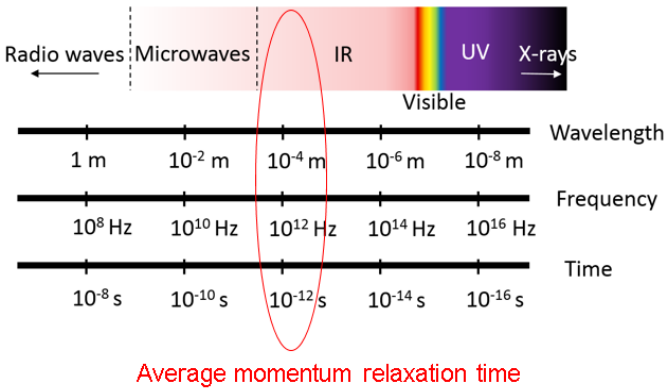

Figure 3.1. The relative position of THz radiation in the electromagnetic spectrum.

The THz range is in the far infrared region on the border with microwave region. 1THz is equal to 10^{12} Hz and corresponds to the processes that occur in the time scale of ~1 ps, with energies of ~ 4 meV, typical wavelength of ~300 μm or wave number of ~ 33 cm^{-1} (*figure 3.1*). The time scale ~ 0.1-1ps is typical relaxation time (scattering time)[47,48]for many compound semiconductors, the energies of a few meV are comparable to binding energies of excitons in many semi-conductive materials[49], also these energies are typical for plasmons[45]. Furthermore, optical and acoustic phonons energies, associated with collective vibrations of atoms and molecular oscillations, lay in the range of a few meV. Thus, THz radiation is an ideal tool to probe low energy electronic processes, occurring in the fs-ps time scale[50,51].

The THz Spectroscopy exists in two different modifications: *THz time-domain Spectroscopy (THz - TDS)* and the *OPTP*. The *THz-TDS* probes the material of interest in the

equilibrium state and yields the dielectric function, refractive index and/or phonon absorption in THz frequency range. The *OPTP* is in turn conducted under photoexcitation of the sample and thereby it probes the photoexcited state, yielding the real and imaginary parts of photoconductivity or mobility spectrum. Additionally, this technique is time resolved and allows recording photoconductivity transients. Thereby the various kinetics processes such as polaron and exciton formation, charge carrier cooling and also lifetimes of charge carriers, can be studied with a time-resolution of up ~100 fs [45,52–54]. Thus, THz Spectroscopy in both modifications is a powerful method that characterizes transport and opto-electronic properties of the material of interest including the sum of electron and holes mobility μ_Σ, and lifetimes τ of charge carriers, which together determine the diffusion length. Moreover, the frequency-dependence of the mobility allows determining some transport properties including effective masses of charge carriers, scattering times, localization length in nm-scale and etc., which will be detailed in this chapter.

The OPTP is the main technique, that is used in this thesis to characterize the charge carrier transport properties in the perovskite materials of various dimensions. Therefore, this chapter is dedicated to the principles of the THz Spectroscopy. Further, in this chapter, detailed description of the set-up is given as well as principles of data analysis and interpretation models are introduced.

3.2. Basic principles of THz spectroscopy

THz-TDS. As stated above, the THz-TDS is steady state technique and probes the sample without preliminary photoexcitation. In order to perform the THz-TDS measurements two different kind of samples are needed, first a bare substrate, used as a reference sample, and the substrate with the thin film deposited onto it. The properties of the thin film are probed. For example, in this thesis the charge carrier properties of various perovskites materials are studied which were deposited on quartz substrate.

The basic principles of THz-TDS technique are shown in *figure 3.2 (a)*. First, a few ps long THz pulse $E_{THz}(t)$ is incident onto the reference substrate and the electric filed of the transmitted THz pulse $E_{ref}(t)$ is detected. Secondly, the THz pulse transmits through the substrate with thin film deposited onto it, and again the transmitted electric field $E_{tf}(\omega)$ is recorded. The THz pulse $E_{tf}(\omega)$, transmitted through the thin film and substrate, is attenuated due to absorption in

the thin film and delayed due to the longer optical path length transferring through the additional thin film. The frequency dependency of the transmitted pulses is obtained by Fourier transform and the final transmission function is defined as follows:

$$T(\omega) = \frac{E_{tf}(\omega)}{E_{ref}(\omega)} \tag{3.1}$$

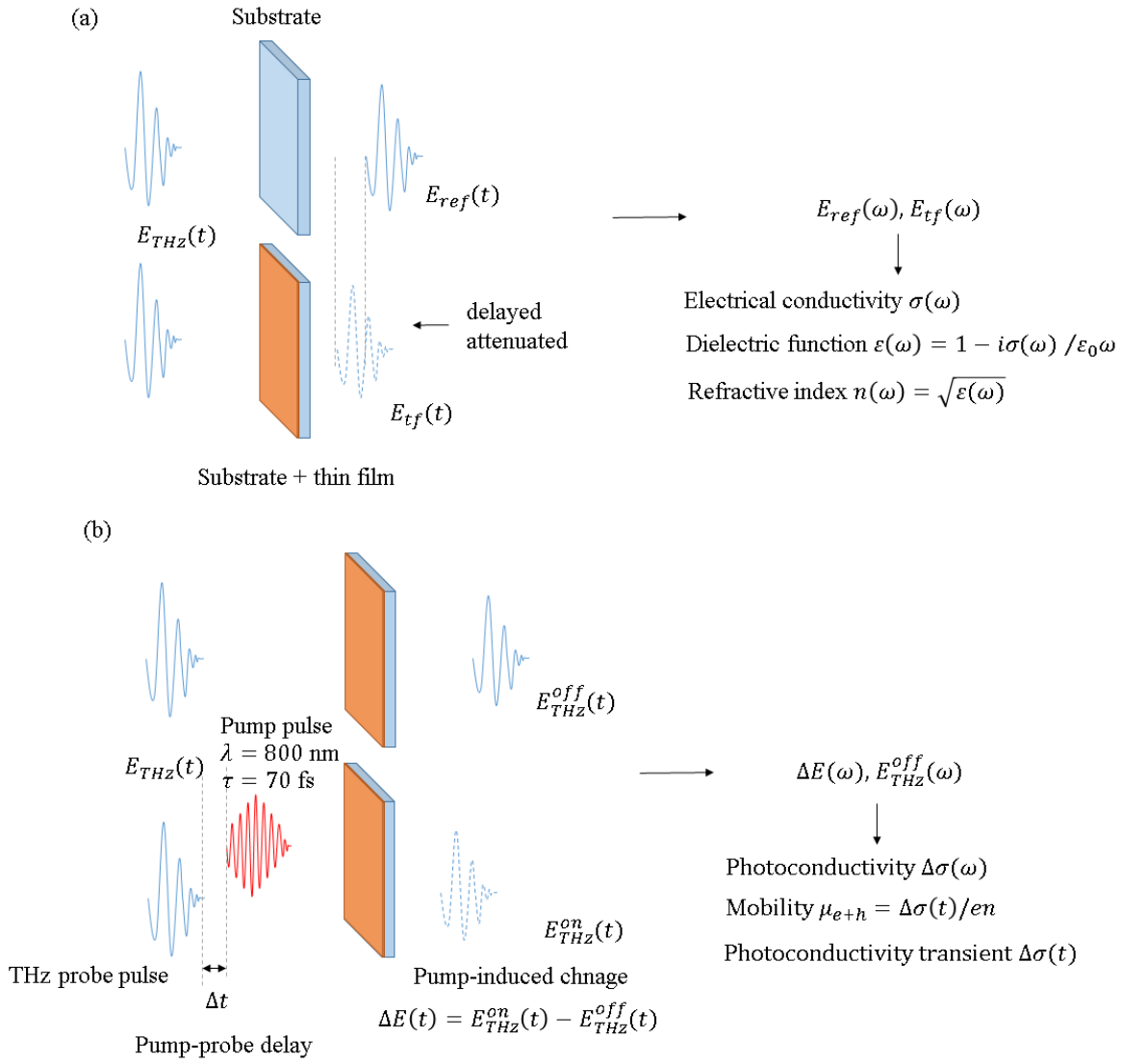

Figure 3.2. Principle of THz Spectroscopy in two different modifications: (a) Scheme of THz- Time domain Spectroscopy (THz-TDS) modification; (b) Scheme of OPTP Spectroscopy.

Within thin film approximation, the transmission function is related to the conductivity $\sigma(\omega)$, that in turn allows to determine the dielectric function of the material of interest by

$\varepsilon(\omega) = 1 - i\,\sigma(\omega)/\omega\varepsilon_0$, where $\varepsilon_0 = 8.9{\cdot}10^{-12}$ Fm^{-1} is vacuum permittivity, and refractive index by $n(\omega) = \sqrt{\varepsilon(\omega)}$ in the low THz range (*figure 3.2 a*). The frequency dependent real part of dielectric function $\varepsilon(\omega)$ in turn allows to determine the static ε_{st} and high-frequency ε_∞ dielectric constants while the imaginary part of dielectric function allows to find the frequency positions of TO optical phonon modes excited by THz radiation.

OPTP (TRTS). The OPTP Spectroscopy is a modification of the THz-TDS, as shown in *figure 3.2 (b)*. This method probes the photoexcited state in the material of interest. The photoexcitation of the sample results in pump-induced change of electrical conductivity, called photoconductivity$\Delta\sigma(\omega) = en\mu_\Sigma$, where *e* is the elementary charge, *n* is the concentration of excited charge carriers (photoelectrons and photoholes) and μ_Σ is a sum of the effective electron mobility and the effective hole mobility.

The measurement is performed similar to THz TDS. First, a short THz pulse is incident onto the thin film that is not photoexcited and the transmission of the THz pulse is detected. Then the thin film is photoexcited by optical pump pulse with energy above the band gap energy in order to transfer the charge carriers from the valence to conductance band (electron-hole pairs excitation). After some delay time the short THz pulse is transmitted through the photoexcited sample and the THz field is recorded. This THz pulse is attenuated and delayed compared to the one before photoexcitation. The transmitted THz pulses with (pump on) and without (pump off) photoexcitation is converted into the frequency domain by Fourier transformation. The difference between THz pulses in equilibrium and photoexcited states is called pump-induced change in THz pulse $\Delta E(\omega) = E_{THz}^{off}(\omega) - E_{THz}^{on}(\omega)$. The transmission function in this case is given by:

$$T(\omega) = \frac{\Delta E(\omega)}{E_{THz}^{off}(\omega)} \tag{3.2}$$

By knowing the transmission function it is possible to determine the photoconductivity and consequently the mobility as a function of frequency.

Since the OPTP Spectroscopy is a time-resolved method, it is possible to record the photoconductivity transients by varying the delay time between the THz and pump pulses. The analysis of the photoconductivity transients yields information about charge carrier kinetics in the material of interest.

3.3. Set-up

In this work, the OPTP setup is based on a Ti-Sapphire laser system that delivers 70 fs long pulses centered at 800 nm wavelength with repetition rate 150 kHz. The pulses from this laser are split into three branches by a beam splitter BS1 and BS2: a beam for THz generation beam, a beam for THz detection beam and a pump beam for photoexcitation of the sample. The scheme of the setup, exploited in this work, is shown in *figure 3.3*.

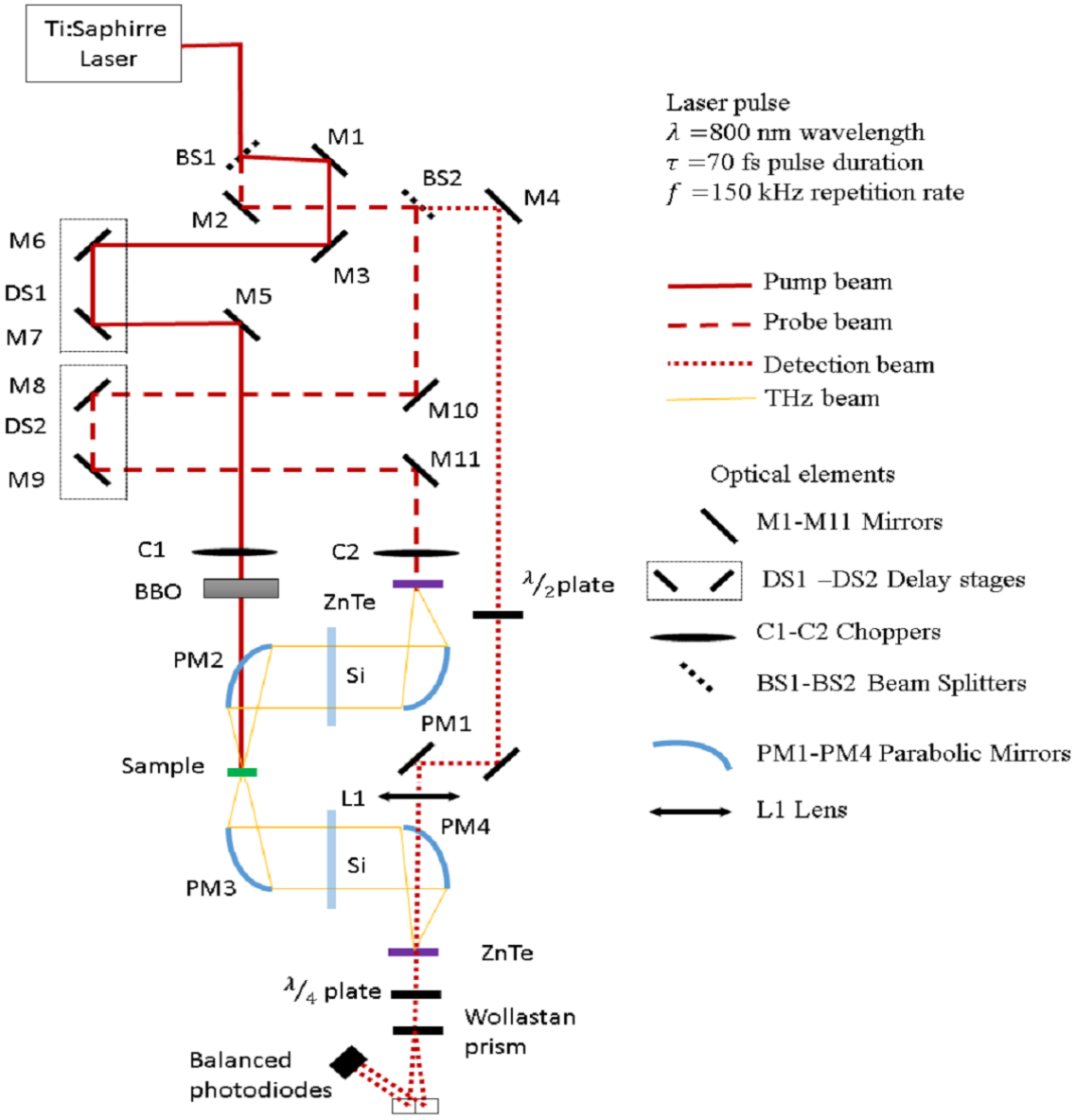

Figure 3.3. The scheme of the OPTP set-up used in this work.

THz generation beam. The generation beam is focused onto the THz emitter after passing the delay stage DS1. THz emitter is a ZnTe crystal, which generates the THz pulses by optical rectification in the frequency range from 0.5 THz to 2.5 THz. Optical rectification is non-linear

optical process that generates the difference between the frequencies in the bandwidth of the optical laser pulse. Since a Si or PTFE-based filter is used to filter out residual infrared light from the path and the only THz pulse is focused by off-axis parabolic mirror onto the sample surface. Then the focused THz pulse transmits through the sample. Another pair of off-axis parabolic mirrors collimates and refocuses the transmitted THz pulse onto a second ZnTe crystal for pulse detection.

THz detection beam. The detection beam is also focused onto the detection ZnTe crystal. The THz detection path length should be equal to THz generation path length to assure that both beams temporarily overlap at the detection crystal. Since the duration of the laser pulse is much shorter than the duration of THz pulse (70fs vs ~ 1ps), the laser pulse can sample individual parts of the THz pulse. Varying the delay time by moving the delay stage DS1, it is possible to scan the full THz pulse and to measure its electric field as a function of time. The detection of the electric field of the THz pulse occurs due to changes in the polarization of the detection beam. The electric field of the THz pulse induces the changes in refractive index of the ZnTe crystal via electro-optic effect and makes the detection crystal birefringent. This birefringence rotates the polarization of the detection pulse, which is proportional to the amplitude of the electric field of the THz pulse. The polarization of the detection beam is turned into circular (or elliptic when modulated by the THz beam) by passing a $\lambda/4$ plate. A Wollaston prism splits the beam into two beams of two orthogonal polarizations to each other (s- and p-polarization). They are guided to a pair of balanced photodiodes afterwards that yields no signal if the THz pulse is not overlapping with the detection pulse in the ZnTe crystal. However, if the THz pulse does overlap with the detection pulse, the two beams incident on the balanced diode are not equal anymore and the generated electric current is proportional to the electric field of the THz pulse.

Pump beam. The pump beam is an optical pulse, which is used to excite the charge carriers in the sample from the valence band to the conductance band. The pump pulse with an initial wavelength of 800 nm (pump beam) passes through the delay stage DS2 and a BBO crystal that converts the pump beam into photons with wavelength of 400 nm by second harmonic generation. The delay stage DS2 allows to control the arrival time between the pump pulses and the THz pulse. After passing through the delay stages and BBO crystal, the pump beam is guided onto the surface of the sample. It is important that the pump photoexcites the sample homogeneously in the area larger than the area probed by the THz pulse, which has FWHM of ~1mm. Therefore, the pump beam is expanded by a lens to a FWHM of around 3 mm. A part

of the pump beam may be transmitted through the sample, therefore, the second silicon filter is required behind the sample so as to avoid the incidence of the optical pump beam onto the balanced diodes. In order to avoid the absorption of the THz radiation in the air, the measurement is normally carried out in the nitrogen atmosphere.

Dual phase lock-in amplifier. In order to minimize the measurement noise, the dual phase lock-in amplifier is exploited in the OPTP system. To this end, pump and probe beams are both chopped by mechanical choppers C1 and C2 at different frequencies, respectively. The chopper C1 transmits and blocks the pump pulse and thereby alternates the excitation of the sample (pump off and pump on). Consequently, the transmitted THz pulse through excited $E_{THz}^{on}(t)$ and unexcited $E_{THz}^{off}(t)$ sample is detected. The first lock-in amplifier of the pump beam is locked to the frequency of chopper C1 and delivers half of the difference in the THz pulse of excited and unexcited sample (pump-induced change $\Delta E(t)$) into the channel $X_1 = 0.5\Delta E(t) = 0.5(E_{THz}^{off}(\omega) - E_{THz}^{on}(\omega))$. The second lock-in amplifier, locked to the THz beam chopper C2, records the difference between unexcited sample $E_{THz}^{off}(t)$ and the channel X_1 into the channel $X_2 = E_{THz}^{off}(t) - X_1$. Thus, by knowing the signals in the channels X_1 and X_2 one may calculate the transmission function according to $T(t) = \frac{\Delta E(t)}{E_{THz}^{off}(t)} = \frac{2X_1}{X_2 + X_1}$ [55].

Photoconductivity spectra and transients. The photoconductivity spectra are recorded at fixed pump-probe delay (the mechanical stage DS2 does not move) and the stage DS1 is scanning the electric field of the THz pulse. The recorded pump-induced change $\Delta E(t)$ and THz field $E_{THz}^{off}(t)$ are converted into frequency domain by Fourier transform and are analyzed by the so-called thin film approximation to retrieve the photoconductivity spectra in the frequency domain. *Figure 3.4* illustrates the THz signal in time domain (*figure 3.4 (a)*) and Fourier transform of the transmitted THz pulse in the frequency domain (*figure 3.4 (b)*).

The photoconductivity transient is recorded by moving the stage DS 1 and thereby changing the time of excitation of the sample. Before starting the measurement, the DS2 is shifted to the position that the optical detection pulse samples the THz pulse at its peak. Then the stage DS2 is fixed, which guarantees the same arrival time for THz pulse. The maximum pump-probe delay time is limited by the length of the delay stage. For the set-up in this work the maximum delay time is around 1850 ps.

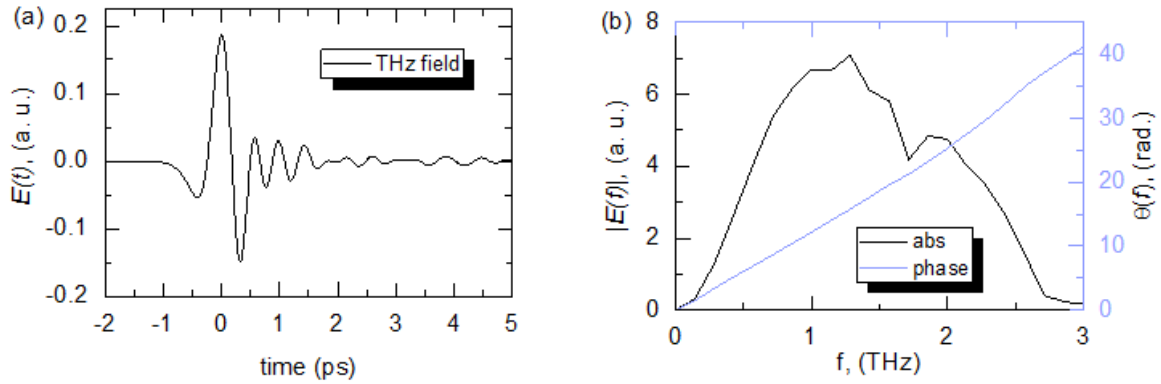

Figure 3.4. The THz pulse in the time domain (a) and the amplitude and phase of the same pulse in the frequency domain (b).

3.4. Thin film approximation and mobility spectra calculation

As stated above, the transmission of THz pulse through the unexcited sample $E_{THz}^{off}(t)$ and its pump-induced change $\Delta E(t)$ are measured as a function of time. This allows calculating the transmission function $T(\omega)$ *(3.2)* by performing the Fourier transform. The transmission function can in general to be connected to the photoconductivity by transfer matrix method[44]. However, for thin films, usually the thin film approximation *(3.3)* is used, where n_s is refractive index of the substrate, d is a thickness of the thin film, c is a speed of light and ε_0 is vacuum permittivity. It can be applied if the thin film is excited homogeneously, if the thickness of the thin film is small compared to the wavelength of the THz pulse ($d \ll n\lambda_{THz}$), and if the thickness of the underlying substrate is larger than wavelength of the THz pulse ($d_s \gg \lambda_{THz}$). All these conditions are satisfied for the samples probed in this thesis.

$$\Delta\sigma(\omega) = -c\varepsilon_0(1+n_s)\frac{\Delta E(\omega)}{E_{THz}^{off}(\omega)} \tag{3.3}$$

The negative sign in *equation (3.3)* reflects the attenuation of the transmitted THz pulse after photoexcitation: $\Delta E(t) < 0$.

By knowing the photoconductivity $\Delta\sigma(\omega)$ and the concentrations of the photoexcited charge carriers n, the complex mobility can be determined:

$$\mu_\Sigma(\omega) = \frac{\Delta\sigma(\omega)}{en} \tag{3.4}$$

It is important to point out that mobility measured in the THz set-up is a sum of electron and hole mobility. The photocarriers concentration is equal to absorbed photon flux (number of absorbed photons per area and time) $\phi = A \cdot P/(fSE_{ph})$, where f is the laser repetition rate, P is the power of incident pump pulse, S is the area of the incident pump pulse and E_{ph} is the photon energy at the wavelength λ and A is the fraction of absorbed photons (absorbance). If the reflectance of the optical pump pulse at the sample surface is R and the transmittance is T, then the absorbance is $A = (1 - R - T)$. In this case the photo-carrier concentration is equal to a number of absorbed photons $n = A\phi$. Finally, the analytical expression for mobility within thin film approximation is given by

$$\mu_{\Sigma}(\omega) = -\frac{c\varepsilon_0(1+n_s)}{e\phi(1-R-T)}\frac{\Delta E(\omega)}{E_{THz}^{off}(\omega)} \tag{3.5}$$

The further analysis of mobility spectra is based on applying the appropriate models (Drude, Drude-Smith and etc.), which are described in detail bellow. They allow to obtain the further transport parameters such as DC mobility (mobility at ω= 0 THz, mobility when no external force field), effective mass of charge carriers, scattering rates and localization parameters and etc.

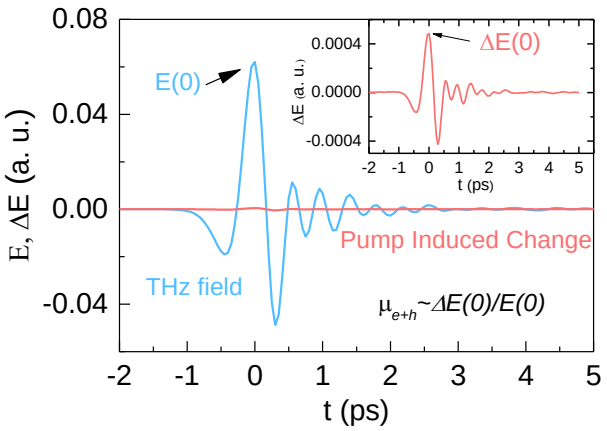

Figure 3.5. The illustration of the calculation of the mobility form the peaks of the THz and pump-induced pulses (inset) in the time domain.

The DC mobility may be not always assigned from the mobility spectra for some reasons (i. e. the spectra is overload with phonon features and etc.). For some cases, when the mobility spectra exhibit a weak frequency dependency and real part of mobility may be approximated as a constant within the measurement frequency range while imaginary part of mobility is close to zero, than the mobility may be assigned form the peak of THz pulse (*figure 3.5*) in the time domain as it is given by

$$\mu_{\Sigma} = -\frac{c\varepsilon_0(1+n_s)}{end}\frac{\Delta E(t_{THz}=0)}{E_{THz}^{off}(t_{THz}=0)} \tag{3.6}$$

3.5. Data analysis

After obtaining the mobility spectra (real and imaginary parts), the various models may be applied in order to interpret the data. They can reveal information about the transport such as effective mass, DC mobility, scattering time, localization parameters and the localization area size and etc..

Drude model

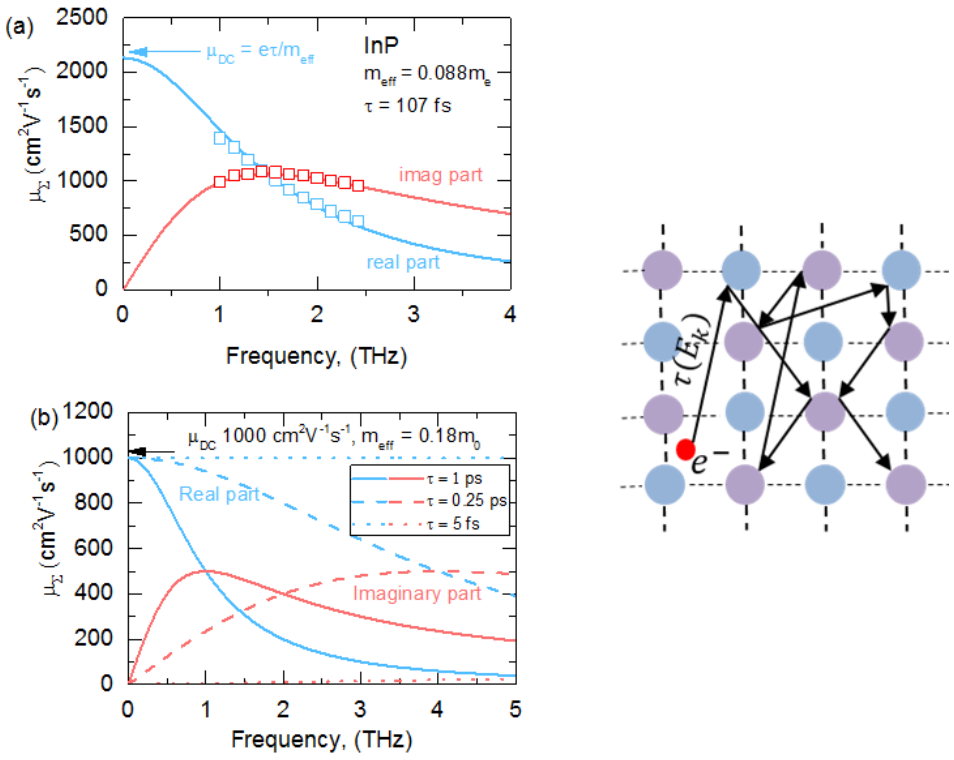

Figure 3.6. The THz spectrum, measured for InP wafer, and applied Drude model that yields the effective mass $m_{eff} = 0.088m_0$, τ = 108 fs and DC mobility μ_{DC} = 2200 cm^{2}V^{-1}s^{-1} (a); The behavior of Drude mobility at various scattering times τ = 1 ps, 250 fs, 5 fs (b); the schematic illustration of origin of Drude mobility, coming from scattering of charge carriers at lattice nodes (c).

This model describes the behavior of the charge carriers that undergo the scattering events at some scattering centers at the rate γ or scattering time $\tau = 1/\gamma$. Within this model the charge carriers are regarded as the free charge carriers. The frequency dependent mobility is given by:

$$\mu(\omega) = \frac{e\tau}{m}\frac{1}{1 - i\tau\omega} \tag{3.7}$$

where $\mu_{DC} = e\tau/m$ is DC mobility at $\omega = 0$, m is a charge carrier effective mass.

Figure 3.6 (a) shows the real and imaginary parts of the mobility spectrum for an example of InP. It can be seen that real part of the mobility spectra starts at zero frequency with its maximum and gradually decreases while the imaginary part is always positive for free charge carriers. The application of this model to experimental results may yield the scattering time, the effective mass of charge carrier, as well as the DC mobility. However, in some cases, the real part is almost constant and imaginary part is around zero, then the scattering time and effective mass of charge carriers from a fit are rather ambiguous. In such a case the analysis is limited by only DC mobility by extrapolation the spectra to *y* axis ($\omega = 0$) (*figure 3.6 (b)*).

Moreover, Drude model does not account for charge carrier localization. Such localization has a distinct frequency-dependence, which can be described by the Drude-Smith model or the Lorentzian oscillator model.

Truncated Drude-Smith model

Smith et al.[56] proposed a modified Drude model in order to describe the transport properties of the localized charge carriers. According to this approach, the charge carriers undergo typical Drude scattering, where they are preferentially scattered backwards. The mobility is given by *equation (3.8)*. In this model the phenomenological parameter c_1 is introduced that can vary from 0 to -1. For c_1= 0, the Drude mobility *(3.7)* of free charge carriers is derived. For c_1= -1, the charge carriers are totally localized and the DC-mobility is zero. The negative values of the parameter results in suppression of the DC mobility $\mu_{DC} = e\tau(1 + c_1)/m$ and the imaginary part of the mobility is becoming negative in the low frequency range. The negative imaginary part is the most distinctive feature, indicating the presence of charge carrier localization. *Figure 3.7 (a)* illustrates the behavior of the Drude-Smith mobility compared to Drude model, described in the previous section, and the application of Drude-Smith fit (*figure 3.7 (b)*) to the mobility spectra of perovskite thin film at low temperatures with extracted fir parameters: scattering time τ =80 fs and the phenomenological parameter c_1=-0.7.

$$\mu(\omega) = \frac{e\tau}{m}\frac{1}{1-i\tau\omega}\left[1+\frac{c_1}{1-i\tau\omega}\right] \tag{3.8}$$

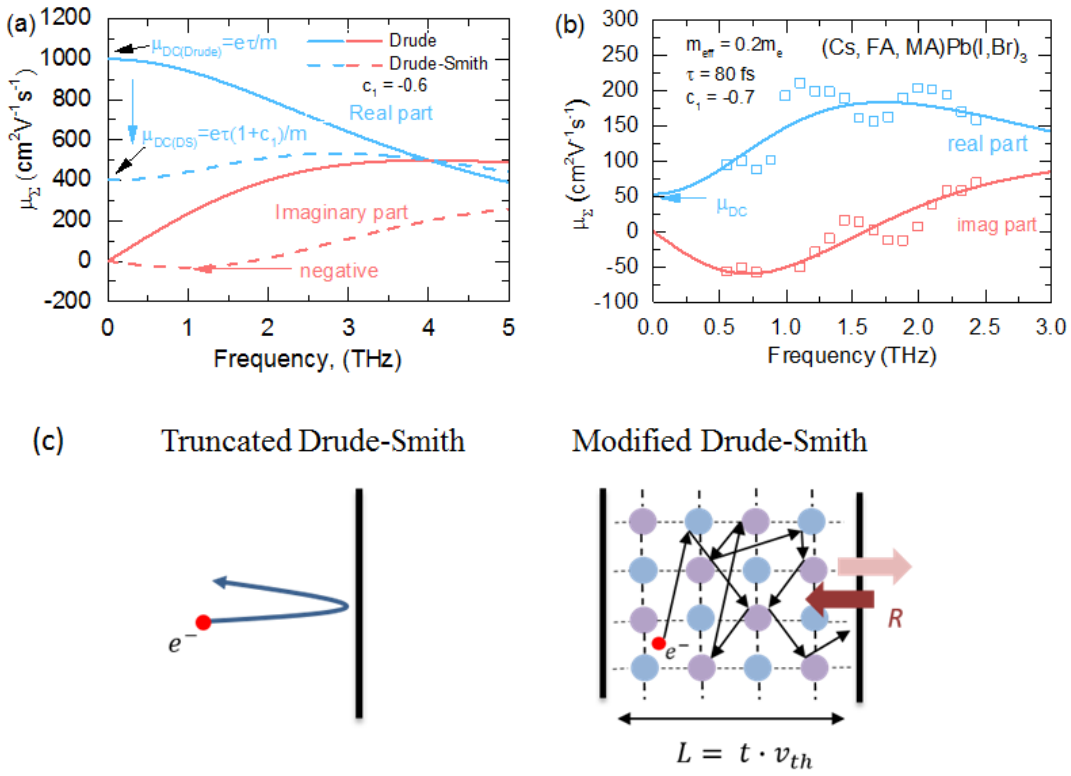

Figure 3.7. Illustration of suppression of real part of mobility and negative imaginary part within Drude-Smith model at c_1 = -0.6 (a); application of Drude-Smith model to mobility spectra of triple cation (Cs,FA,MA)Pb(I,Br)$_3$ thin film: fit parameters $m_{eff} = 0.2m_0$, c_1 = -0.7, τ = 80 fs (b); Explanation of differences in truncated and modified by (Cocker at al, 2017)[57] Drude-Smith models (c).

However, the Drude-Smith model has a number of disadvantages. Firstly, this model was derived by considering preferential backscattering only in the first scattering event, which is has not been motivated. Regrading backscattering for all events even leads again to the Drude-model, which is irritating. Therefore, the parameter c_1 will be used as a phenomenological merit for charge carrier localization in the material of interest. But the clear physical meaning of this parameter is questionable.

Modified Drude-Smith model

(Cocker et al, 2017)[57] has recently modified the Drude-Smith formula and showed a good agreement of his approach by Monte-Carlo Simulation. He considered a charged particle that is localized in a box of size L with walls with reflectivity R =1 and this particle undergoes the

scattering events at effective scattering time $\tau = 1/\tau_D + 2Rv_{th}/L$, where $\tau_D$is scattering time, derived by Drude model. Alongside with scattering, a charge carrier travels between the walls of the box at the rate$1/t = v_{th}/L$, where $v_{th}$is a thermal velocity $v_{th} = \sqrt{3kT/m}$. He also generalized the formula for the case when the reflectivity of the walls is lower than 1 and introduced the modified Drude-Smith formula as follows:

$$\mu_{DS}(\omega) = \frac{e\tau}{m}\frac{1}{1 - i\tau\omega}\left(1 + \frac{c_1(R)}{1 - i\omega/a}\right) \tag{3.9}$$

where

$$a = \frac{12}{t}\left(\frac{\tau}{t + 2\tau}\right) \tag{3.10}$$

The phenomenological parameter $c_1$depends only on walls reflectivity *R* and *L* shows the localization scale of charge carriers. Figure 3.7 (c) illustrates the differences in modified and truncated Drude-Smith models.

Thus, compared to the truncated Drude-Smith approach, all parameters, encountered in the modified version of the Drude-Smith model, obtain the physical meaning: first, a charge carrier is treated as localized in a space, restricted by two walls with some probability to be transmitted through the walls or be reflected back; phenomenological parameter $c_1(R)$ is now dependent only on the reflectivity of the walls *R*, *t* is a diffusion time between the walls and *L* is localization length - the travelling distance for charge carriers between the walls.

Lorentzian oscillator

Another approach, used to describe the charge carrier localization, is Lorentzian oscillator response. The Lorentzian oscillator represents localization of a charge carrier in a parabolic potential. The mobility for Lorentzian oscillator looks like a resonance at the frequency ω_0 and it is given by the following equation:

$$\mu(\omega) = \frac{e}{\gamma m}\frac{i\omega}{\omega^2 - \omega_0^2 + i\gamma\omega} \tag{3.11}$$

where $\gamma = 1/\tau$ is the scattering rate, defining the width of the resonance, $\omega_0$is the frequency position of the resonance.

In case of Lorentzian oscillator, the DC mobility is zero and the imaginary part is negative at low frequencies. The typical mobility spectra for charge carriers localized in a parabolic potential is shown in *figure 3.8*.

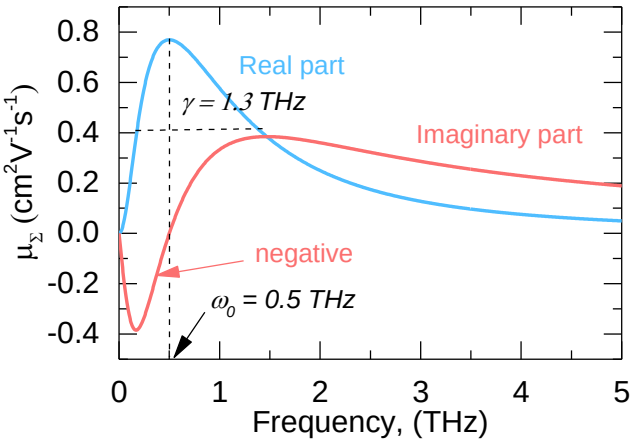

Figure 3.8. Lorentzian mobility calculated for γ =1.3 THz, ω_0 =0.5 THz.

4. Charge carrier transport in 3D Halide Perovskites

4.1. Introduction

Metal-halide perovskites have generated an enormous interest in photovoltaic applications due to their outstanding optoelectronic properties. These materials have strong absorption coefficients, μm-long diffusion length, long minority carrier lifetimes, low defect concentrations, low non-radiative recombination rates and energy gap in the visible range that can be tuned by varying the composition of the perovskite[5]. Moreover, within only about 10 years of active research, the efficiency of perovskite-based solar cells has reached very high levels of 25.2 %[58] and, thus, comparable to the best, more established inorganic solar cells.

Despite many outstanding optoelectronic properties of halide perovskites, they suffer from light segregation and composition instability in the air. Also the studies on charge carrier transport by Hall measurements, Microwave and THz Spectroscopies have shown that halide perovskites have modest mobilities ranging between 1 - 100 $cm^2V^{-1}s^{-1}$ [8,59–63]. These values are almost two orders of magnitude lower than in standard semiconductors such as InP or GaP under comparable charge carrier effective masses.

To explain the limitation of charge carrier mobility in halide perovskites, several models were introduced. So, for instance, some of the authors[20–22,64] proposed the polaron formation and scattering at LO optical phonons as the main scattering mechanisms at room temperatures. The studies of mobilities at low temperatures have shown that scattering at acoustic phonons is unlikely to play an important role at low temperatures as measured mobilities are too low compared to expected ones from theory[22,23]. The low temperatures are rather influenced by scattering at charged impurities[65]. Also many authors measured mobility in a broad range of temperatures and perform the power law fit T^m, where m = -2.8 – -0.52[8,64,66–69]. However, this approach makes an unambiguous assignment difficult and indicates that likely various scattering processes superimpose, thus leading to a rather complex temperature-dependence.

Along with stated above models, there are some other approaches to explain the limitation of charge carriers mobility in halide perovskites, i.e. dynamic disordering theory[26],[70] Rashba effect[25] and dielectric dragg[24].

In this chapter we analyze and discuss the mobility spectra of various halide perovskites thin films samples measured by OPTP that is in details described in the previous **chapter 3**

"Experimental Method and Data Analysis". We also calculate mobilities regarding various scattering mechanisms with the focus on low temperatures. We show the mobility at low temperatures can be modelled by scattering at both charged and neutral impurities. Additionally, we analyze the impact of exciton formation on mobility at low temperatures. Finally, we discuss the influence of cation compound on charge carrier transport in a broad range of temperatures.

4.2. Sample preparation

In this chapter charge carrier transport properties of polycrystalline 3D perovskite thin films with various cation compounds $MAPbI_3$, (Cs, FA)PbI_3, (Cs, FA, MA)Pb(I, Br)$_3$ and $CsPbI_3$ are discussed.

The thin films with stoichiometry $MAPbI_3$, $[CsPbI_3]_{0.05}[FAPbI_3]_{0.95}$ and triple cation $[CsPbI_3]_{0.05}[(FAPbI_3)_{0.83}(MAPbBr_3)_{0.17}]_{0.95}$ were provided for measurements from Potsdam University by Dr. Martin Stolterfoht from the research group of Prof. Dr. Neher. The thin films were prepared and spin coated as it is described in the following papers[71,72]. (Cs,FA)PbI_3 sample was prepared similar to triple cation thin film with only difference that thin film preparation was done without adding $MAPbBr_3$ and 120 μl of 1.5M CsI was dissolved in DMSO and then it was mixed with 3 ml $FAPbI_3$ solution. The thin films were deposited on the quartz substrate.

The polycrystalline perovskite thin film $CsPbI_3$ was prepared by physical vapor deposition at the Helmholtz Zentrum Berlin as described in Becker, et al[73] and deposited on quartz substrate and encapsulated (glued) on the top with another quartz substrate.

4.3. Phonon modes in the low THz frequency range

OPTP measures the change in the transmission $\Delta T/T$ of a terahertz pulse after photoexcitation of the sample by optical pump. Under known excitation conditions, the analysis derives the sum mobility μ_Σ of the electron mobility and hole mobility that is given by *equation (3.5)*.

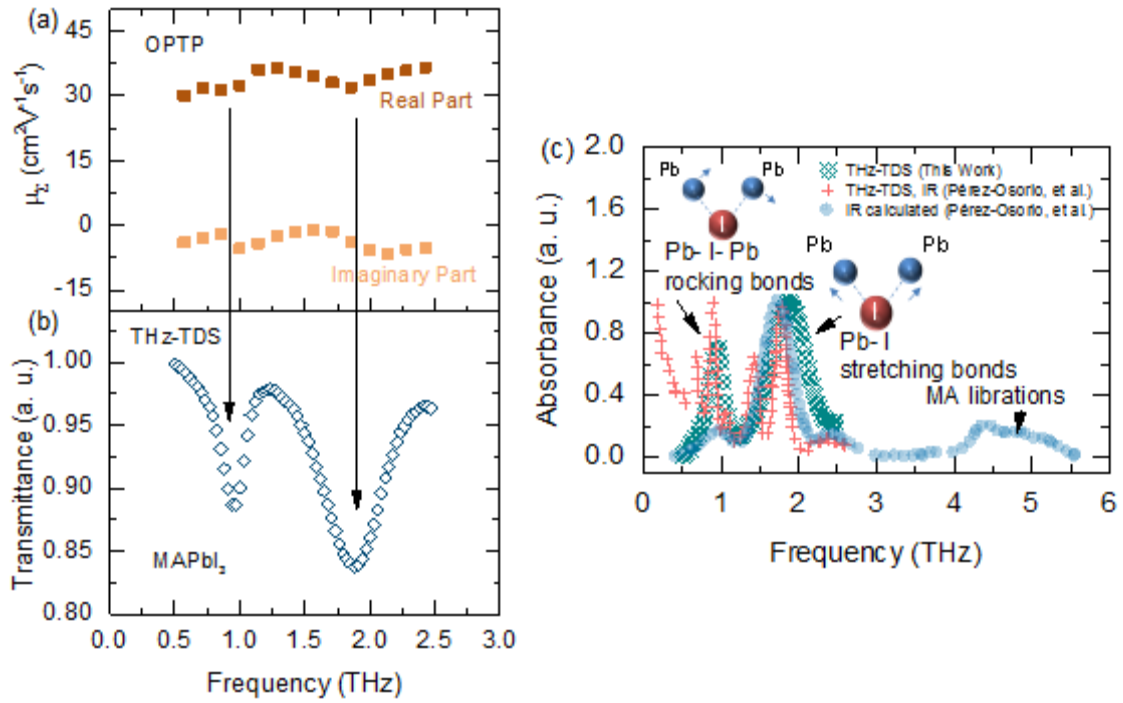

Figure 4.1. Real and Imaginary part of mobility spectrum measured by OPTP (a), THz transmission spectrum measured by THz-TDS (b) and comparison of measured THz- TDS results in this work with calculated IR active modes intensities in the work Perez-Osorio et al.[74](c). The arrows in the (a) and (b) show the correlation between phonon features in mobility spectrum and excited phonon modes in $MAPbI_3$.

Figure 4.1 shows the frequency-dependent AC mobility and THz transmission spectra for measured polycrystalline thin film $MAPbI_3$. The mobility spectrum exhibits an imaginary part close to or slightly below zero and a relatively constant real part, which are overlaid by two features at 1 THz and 1.8 THz.

These absorptive features in *figure 4.1 (a)* should not be attributed to the mobility of photoinduced charge carriers, but arise from a shift or attenuation of the phonon absorption modes upon photoexcitation. Phonon transitions are also visible in the transmission spectra of the unexcited sample, which were measured by static time-domain THz spectroscopy (THz-TDS) and are shown in *figure 4.1 (b)*.

The origin of these features was studied in a number of works[21,74]. In the work (Perez-Osorio et al)[74] frequencies and intensities of Raman and IR active modes in $MAPbI_3$ by density functional perturbation theory were calculated and compared with measurements performed by THz-TDS in the low THz frequency range and Fourier Transform Infrared Spectroscopy at

above 1.8 THz. *Figure 4.1 c)* shows the comparison of reverse THz transmission spectrum, done in this thesis, with results obtained by (Perez-Osorio et al, 2015)[74]. T*able 4.1* shows the some calculated IR active modes intensities relevant in the low THz frequency range, adopted from the same paper.

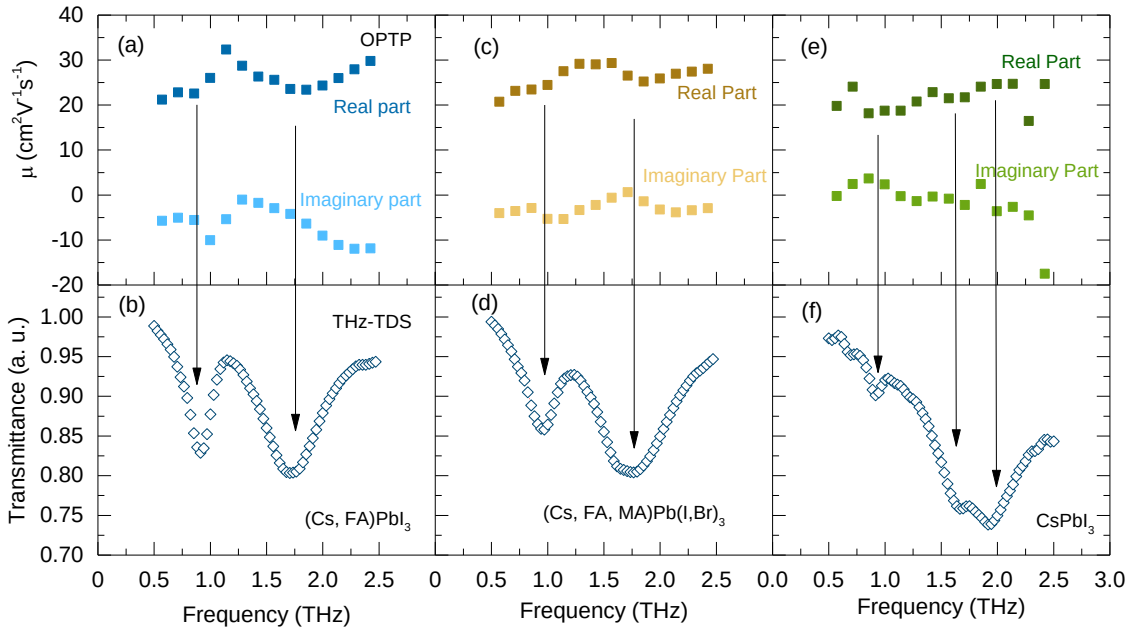

Figure 4.2. (a), (c), (e) real and imaginary parts of mobility spectra in polycrystalline thin films (Cs,FA)PbI_3, (Cs, FA, MA)$Pb(I, Br)_3$ and $CsPbI_3$ respectively and (b), (d), (f) their THz transmission spectra.

According to the calculations (see *table 4.1*), several modes result from vibrations of Pb-I bonds. The mode at 1.9 THz results from MA librations in the measurement range between 0.5 and 2.5 THz. The peak at around 1 THz correlate well with ones calculated at 0.93 and 0.96 THz that result from vibrations of Pb-I-Pb rocking bonds. Thus, one may conclude that the peak at 1THz is an overlap of these two at 0.93 and 0.96 THz. In the upper THz range from 1.5 to 2.5 THz there are some intense modes at 1.5 THz and 1.8 THz resulted from Pb-I-Pb blending bonds and Pb-I stretching modes respectively. Also, there is a single mode at 1.9 THz that originates from MA librations. This indicates, that at around 1.8 THz all these modes overlapp and the Pb-I-Pb blending and Pb-I stretching modes as well as MA librations can be assigned to the peak at 1.8 THz. Thus, it can be concluded that the features in the mobility spectrum originate from Pb-I lattice vibrations excited by the THz field.

As most of the excited modes result from metal-halide network vibrations, the perovskites with various cations compositions show similar features at the same frequencies in their

mobility spectra, displayed in *figure 4.2*. Similar to $MAPbI_3$, clear correlation between the features in the obtained mobility spectra in *figure 4.2 (a, c, e)* and the phonon modes in *figure 4.2 (b,d,f)* can be seen. Indeed, the THz transmission spectra of the (Cs, FA)PbI_3 thin film exhibits identical behavior as in MAPbI3 thin film. Also, the THz transmission of triple cation (Cs, FA, MA)Pb(I, Br)$_3$ sample look similar as in MAPI with slightly broadened second peak at around 1.8 THz. The broadening is assumed to be due to complex halide composition of two different atoms: iodine and bromine.

The transmission spectrum for fully inorganic $CsPbI_3$ thin film shows two split peaks at around 1.5 and 1.8 THz. Such splitting was previously observed in the work (Damle et al, 2018)[75]. In this work the low frequency Raman spectra of pure $MAPbI_3$, $CsPbI_3$ thin films and mixed (Cs, MA)PbI_3 thin films with various concentrations of Cs in the low frequency range 0 – 200 cm^{-1} (0 - 6 THz) were studied. It was shown that $MAPbI_3$ reveal broadened and smoothed Raman spectra while the increase in Cs concentrations in perovskite makes the peaks from metal-halide vibrations more distinctive and better resolved. As explained in this work, the increase of content of Cs atoms in the perovskites material results in suppression of anharmonic motions of cations and local thermal phonon fluctuations. Therefore, we assume that splitting in transmission spectrum of the inorganic $CsPbI_3$ thin film comes from less broadening of the transmission lines due to rather fixed position of Cs atoms in lattice cage than in case of fully organic perovskites containing MA.

Table 4.1. Frequency positions and calculated IR intensities of rocking, blending and stretching modes of Pb-I network and MA librations in $MAPbI_3$ adopted from (Perez-Osorio et al)[74].

Group Symmetry	Frequency position, (THz)	Calculated IR intensity, $[(D/A)^2/amu]$
$\boldsymbol{B_{1u}, B_{2u}, B_{3u}, B_{2u}, B_{3u}}$ **(Pb-I-Pb rock)**	0.82, 0.85, 0.93, 0.96, 1	0.1, 0.2, 1.3, 2.6, 1.0
$\boldsymbol{B_{2u}, B_{1u}, B_{3u}, B_{2u}}$ **(Pb-I stretch)**	1.6, 1.7, 1.8, 1.9	7.8, 14.1, 14.3, 9.3
$\boldsymbol{B_{1u}, B_{3u}, B_{1u}}$ **(Pb-I-Pb blend)**	1.4, 1.5, 2.5	0.7, 2.1, 3.1
MA librations	1.9, 4.4, 4.8	2.6, 6.1, 4.2

4.4. Charge carrier mobility at room temperature

Drude Model

The motion of free charge carriers can be described by the Drude-model[44], which is described in details in the **chapter 3 Experimental Method and Data Analysis**. The mobility μ_D is given by the Drude *equation (3.7)*, in which the first factor determines the DC-mobility and the second factor determines the frequency-dependence of the mobility.

To model the OPTP-derived sum mobility of electrons and holes, the individual effective masses and scattering times of electrons and holes should be regarded in principle. However, the effective masses for electrons and holes have been found to be similar in perovskites $m_e \approx m_h$ [20,76] and we also assume here similar scattering times $\tau_e \approx \tau_h$. Under such assumtions, the sum of electron and hole mobility can be described by *equation (3.7)* if the effective mass is regarded as half of the effective mass for electron or holes.

Figure 4.3 shows the modeling of the measured terahertz mobility in the thin films by Drude formula (dashed dot lines), yielding DC mobilities as it is specified in *table 4.2*. However, the effective mass and scattering time are somewhat ambiguous, as the frequency-dependence is rather weak in the measured 0.5 to 3 THz range. Still a lower limit of $\tau < 4$ fs can be obtained from the fit by Drude model for all thin films, if the effective masses of electrons and holes are set to the average literature value of ~0.2 m_e[76–78]. This result is in good agreement with the scattering time 4fs obtained by Karakus et al.[61]. However, negative imaginary mobilities, as slightly observed for all thin films in *figure 4.3*, cannot be modeled by the Drude-model and indicates the presence of localized charge carriers.

Truncated Drude-Smith model

Localized charge carriers can be caused by exciton formation or small polaron formation, atomic disorder, or potential barriers on the nm-scale. These phenomena have been discussed using individual models such as oscillator-like behavior, hopping transport or backscattering and can be phenomenologically described by the Drude-Smith model[44,45,56] that is in details described in the **chapter 3 "Experimental Methods and Data Ananlysis"**. The *equation (3.8)* gives the mobility formula for Drude-Smith model.

The Drude-Smith *equation (3.8)* models the frequency-dependence of the mobility much better than the Drude model, as shown in *figure 4.3*. It derives a localization parameter c_1 of

around -0.7 and the scattering time 7.3 fs for $CsPbI_3$ and 12.6 fs for $MAPbI_3$, which indicates a significant mobility reduction by charge carrier localization. There are a few works[79,80,81]

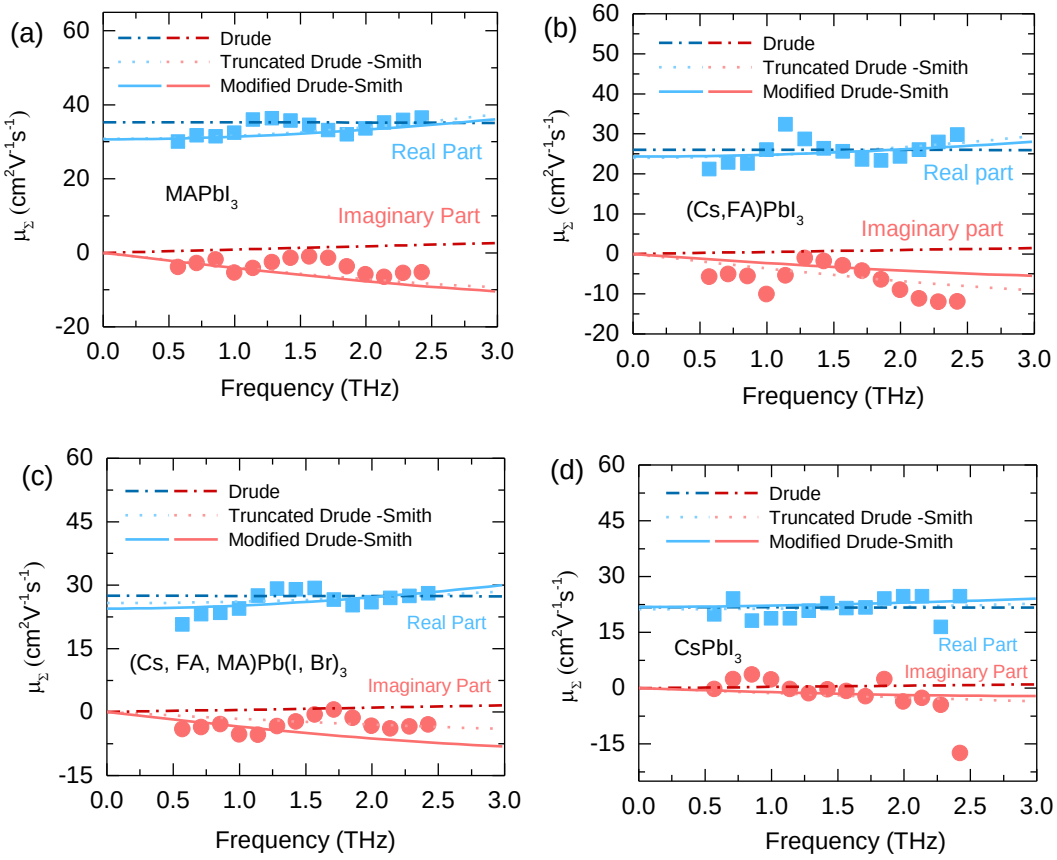

Figure 4.3. The real and imaginary parts of mobility spectra for $MAPbI_3$ (a), $(Cs,FA)PbI_3$ (b), $(Cs, FA,MA)Pb(I,Br)_3$ (c) and $CsPbI_3$ (d) respectively and imposed Drude(dashed dot line), truncated Drude-Smith(dot line) and modified Drude-Smith (straight line) fits above the spectra.

using the Drude-Smith model and discussing charge carrier localization in halide perovskites. For instance, in the work (Ruf et al. 2019)[79] the localization parameter c_1= - 0.63 and the collision frequency Γ = 2.29 THz , corresponding to the scattering time τ = 69 fs, were obtained for $MAPbI_3$ and this localization parameter $c_1$agrees well with our results. The fit results for all thin films are shown in *table 4.3*. The origin of charge carrier localization may be attributed to charge carrier – phonon coupling or polaron formation at room temperatures.

Only a few works[81,82] measured at THz frequencies above 3 THz. However, at such higher THz frequencies difference between the Drude model and the Drude-Smith model will bemore pronounced that would allow more accurate determination of scattering times. Therefore, such measurements are highly desired.

Modified Drude-Smith model

The applied so far Drude-Smith model has several disadvantages, described in the previous **chapter 3 "Experimental method and data ananlysis"**. Therefore, the modified Drude-Smith model, developed by Cocker et al.[57], was applied as well to compare the results. The *equation (3.9)* yields the formula for mobility in modified Drude-Smith model. The fit results for thin films are given in *table 4.2* and are shown in *figure 4.3* (straight line).

The modified Drude-Smith model describes the mobility spectra similarly to truncated Drude-Smith model with signs of localization of charge carriers ($c_1 \approx -0.6$). Interestingly, the localization parameter *L*, that shows the localization scale of charge carriers, is around 5 nm for the thin films what is very close to the specified in the literature polaron radii (5 nm) in halide perovskites[21].

Compared to truncated Drude-Smith model, modified DrudeSmith model, introduced by Cocker[57],allows to estimate not only presence of localization but also estimate the scale of charge carriers localization as well as the phenomenological parameter c_1 becomes more clear physical meaning and depends only on the reflectivity of the scattering walls (see chapter 3). Therefore, the further analysis of mobility spectra in this thesis is performed by modified Drude-Smith model, since it gives more insight into localization of charge carriers

However, regardless of the applied models, the derived DC-mobilities are quite close to each other for all methods as it is seen from *figure 4.3* and *table 4.2*. Also, the derived scattering times are in the range of 2.5 - 4 fs for Drude model, 7.3 - 12.6 fs and 3.5 - 8.4 fs for truncated and modified Drude-Smith models, respectively. All these approaches yield relatively short scattering times compared to conventional high-mobility semiconductors such as GaAs and Si that have 165 fs[83] and 200 fs[84], respectively. Therefore, short scattering times can be identified as one of the origins of the relatively small DC-mobilities in perovskites.

The thin films in this work reveal extremely low scattering times lower than 10 fs for most of the thin films regardless of the applied fit models, resulting in the weak frequency dependency of the mobility. This allows an approximation of the DC mobility from the THz pulse in the time domain as given by *formula (3.6)*. We calculated the mobilities in the thin films according to this approach and we obtained the following values of mobility (33.0 ± 3.0) $cm^2V^{-1}s^{-1}$ for $MAPbI_3$, (25.4 ± 2.5) $cm^2V^{-1}s^{-1}$ for (Cs, FA)PbI_3 and (Cs, FA, MA)$Pb(I, Br)_3$, (21.5 ± 2.2) $cm^2V^{-1}s^{-1}$ for $CsPbI_3$. These mobilities are in good agreement with the estimated

mobility values by Drude, truncated and modified Drude-Smith models. *Table 4.2* summarizes the mobilities and fit parameters for all thin films at room temperature.

Table 4.2. Drude, truncated and modified Drude-Smith fit parameters at room temperature.

Material	Drude			Truncated Drude-Smith				Modified Drude-Smith					Time Domain
	Mobility μ, $cm^2V^{-1}s^{-1}$	Effective Scattering time τ, fs	Effective mass m/m_0 (fixed)	Mobility μ, $cm^2V^{-1}s^{-1}$	Effective Scattering time τ, fs	Effective mass m/m_0 (fixed)	c_1	Mobility μ, $cm^2V^{-1}s^{-1}$	Effective scattering time τ, fs	Effective mass m/m_0 (fixed)	c_1	Localization scale L, nm	Mobility μ, $cm^2V^{-1}s^{-1}$
$MAPbI_3$	33	4.0	0.2	30.8	12.6	0.2	-0.72	30.2	8.4	0.2	-0.6	5	33.0
$(Cs, FA)PbI_3$	26	2.9	0.2	23.5	9.6	0.2	-0.7	24.3	5.7	0.2	-0.5	4.7	25.4
$(Cs,FA,MA)Pb(I,Br)_3$	27.5	3.1	0.2	29.7	10.7	0.2	-0.66	24.5	6.9	0.2	-0.6	5.1	25.4
$CsPbI_3$	21.7	2.5	0.2	15.7	7.3	0.2	-0.7	21.9	3.5	0.2	-0.3	4.7	21.5
Literature ($MAPbI_3$)	27[61]	4[61]	0.2[61]	28.4[85]	69[85]		-0.63[85]						

Injection dependent mobility

The OPTP measurements that were presented in the previous section, were conducted at pump beam excitations around 21 μJcm^{-2} that corresponds to injected charge carrier concentration $6.4 \cdot 10^{17}$ cm^{-3} in $MAPbI_3$. These charge carrier concentrations are above the concentrations of charge carrier generated in solar cells operating normally under AM 1.5G illumination conditions what is about $3 \cdot 10^{16}$ cm^{-3} for $MAPbI_3$. Therefore, it is essential to investigate the charge carrier transport properties under various excitation levels.

The mobility spectra for all thin films were recorded at fluences between 0.5 and 21.1 μJcm^{-2}. The fluence F is in turn determined by power of pump beam P_{pump} per an area S and a laser repetition period $T = 1/f_{rap}$. The corresponding photo-excited charge carrier concentrations (density) Δn are determined according to the following formula:

$$\Delta n = \frac{A \cdot F}{W} \frac{\lambda}{\hbar c} \tag{4.1}$$

where A is absorbance, W is a thin film thickness, λ is a wavelength, $\hbar$ - Planck constant and c is the speed of light.

Figure 4.5 shows the mobility spectra (*figure 4.5 a, c, e*) and the DC mobilities determined from time domain THz spectra at various excitations (*figure 4.5 b, d, f*) for different perovskite thin films. It is seen from these graphs that the mobility spectra of all thin films have similarities. The imaginary part does not undergo any significant changes and remain close to zero or negative at various excitations. The real part in turn shifts upwards while the excitation level decreases. The phonon features and the shape of the spectra remain unchanged regardless of excitation levels. Thus, the transport properties qualitatively do not change in halide perovskites at various injection conditions and the changes occur only due to changes in DC mobilities that vary from 33.3 to 42.6 cm^{2}V^{-1}s^{-1} for $MAPbI_3$, from 25.6 to 34 cm^{2}V^{-1}s^{-1} for (Cs, FA)PbI_3 and from 25.4 to 38.3 cm^{2}V^{-1}s^{-1} for (Cs, FA, MA)$Pb(I,Br)_3$. Thus, all thin films reveal the decrease of mobility with increase in excitation intensity. The same tendency of reduction of mobility with increase in injection level was shown in some other works[63,86] (see *figure 4.5 b*).

We see two possible mechanisms explaining the reduction of mobility with increase in injection levels: (1) enhanced interaction between photo-excited charge carriers (electron-electron scattering) or (2) enhanced scattering at optical phonons due to hot phonon bottleneck effect or due to heating the sample by optical pump pulse at high fluences.

In order to estimate the impact of electron-electron scattering on charge carrier mobility at high injections we may use the empirical formula $1/\tau = 10^{-5} \cdot n$, provided in the book (Ridley, 1999)[28]. This relation shows the connection between the scattering time τ and the threshold charge carrier concentration n, at which the electron-electron scattering has an impact on mobility. As shown in the previous section , the scattering time for MHPs is around 5 fs, the substitution of this value into the relation yields the charge carrier concentration $n = 2 \cdot 10^{19}$ cm^{-3}. This is 1 order of magnitude higher than concentrations that we excite in our thin films. Therefore, based on the obtained result, we may conclude that scattering between the charge carriers is unlikely to be responsible for mobility reduction at high fluences.

Enhanced scattering of electrons and holes at optical phonons may occur by means of hot phonon bottleneck effect and/or heating of the sample by optical pump pulse. After photoexcitation, the charge carrier have an excess energy. The loss of the energy usually occurs within a few ps by emitting the optical phonons. This process is usually called charge carriers cooling. At high injection there are many excess charge carriers, each of them emit the optical phonons while cooling. The high population density of optical phonons during charge carriers cooling may strongly limit the mobility of photo-excited charge carriers in the first picosecond after photoexcitation. In some cases the charge carrier cooling may last up to 10-100 ps. It happens when the energy of optical phonons is much higher than energy of acoustic phonons, the thermal energy from optical phonons can not be transferred to acoustic phonons that transfer the heat further into the crystal. In this case the optical phonons will become absorbed by electrons again. The constant absorption and emission of optical phonons result in increase of average cooling time of charge carriers. This phenomenon constitutes the hot phonon bottleneck effect. A number of work have shown that charge carriers cooling in MHPs occur within ~ 100 ps[87,88]. Since the spectra for the thin films were recorded at pump-probe delay 10 ps, it could be that the charge carriers were not yet cooled down to the band edge and, therefore, enhanced scattering at hot optical phonon could limit the mobility at high fluences. Based on this discussion, we may conclude that the decrease of mobility with increase of injection levels happens rather due to enhanced scattering at optical phonons.

The charge carrier concentration, excited under AM 1.5G illumination conditions, is $3 \cdot 10^{16}$ cm^{-3} for $MAPbI_3$. The mobilities, corresponding to these concentrations, are around 43 $cm^2V^{-1}s^{-1}$ for $MAPbI_3$, 34 $cm^2V^{-1}s^{-1}$ for (Cs, FA)PbI_3 and 33 $cm^2V^{-1}s^{-1}$ for (Cs, FA, MA)$Pb(I,Br)_3$.

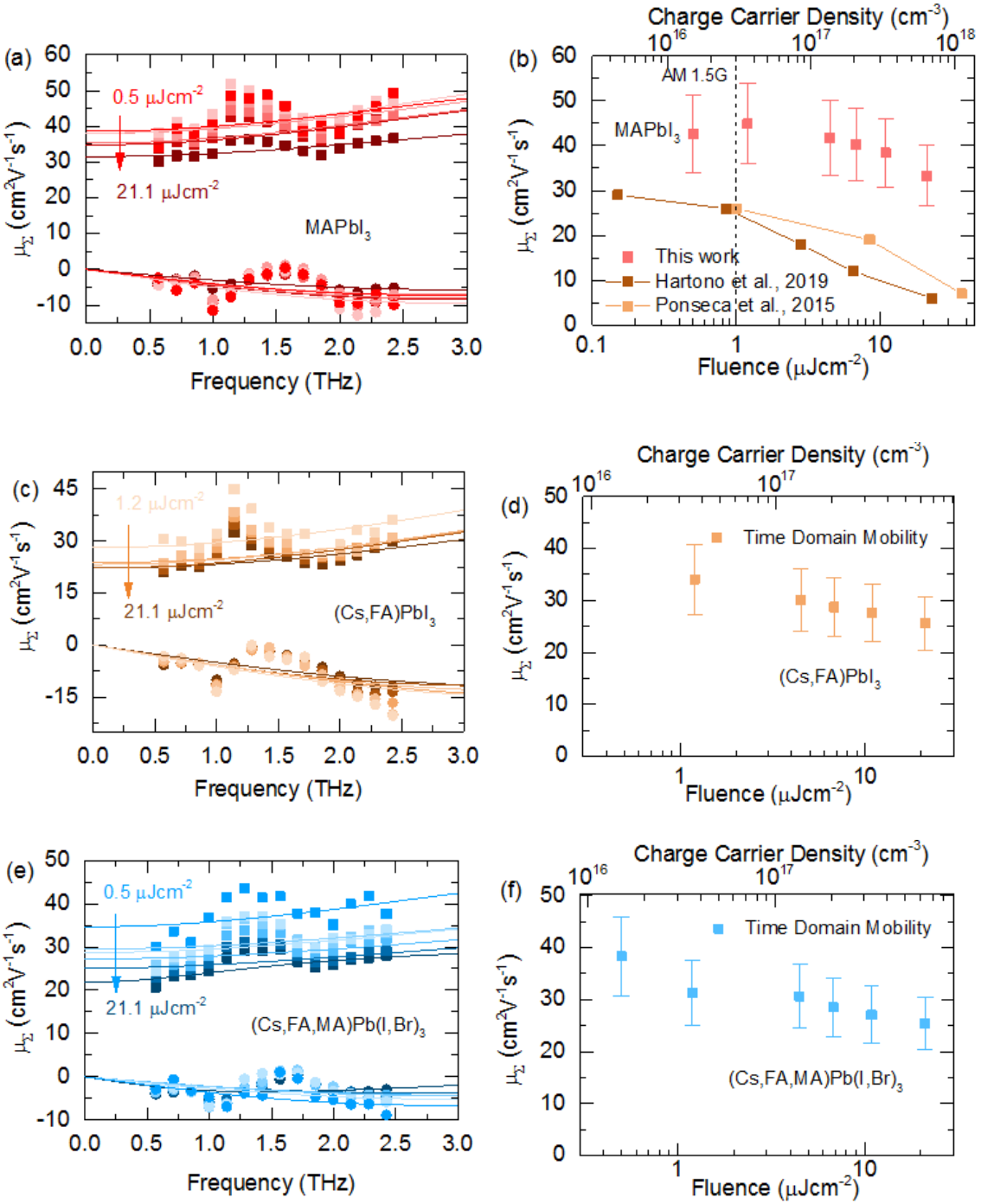

Figure 4.5. The mobility spectra measured at various fluences and time domain mobility versus fluences (injected charge carriers densities) for $MAPbI_3$ (a,b), $(Cs,FA)PbI_3$ (c,d), $(Cs, FA,MA)Pb(I,Br)_3$ (e,f) respectively.

4.5. Temperature dependent charge carrier mobility

Charge carriers in a crystal can scatter at optical and acoustic phonons, at impurities (dopants or defects) or/and at other charge carriers (electrons and holes). In some cases, such interactions may result in formation of quasiparticles such as polarons or excitons. These

scattering mechanisms have specific temperature dependencies as discussed in the theoretical **chapter 2 "Charge carrier transport Theory"**. Thus, the study of the temperature dependent mobility can shed light on the scattering mechanisms that rule out the charge carrier transport properties in a broad range of temperatures.

In this section we perform analysis of mobility spectra for $MAPbI_3$ measured in a broad range of temperatures. Then we model the temperature dependence of the mobility for several scattering mechanisms including scattering at various phonons, impurities and finally excitons by using available in the literature parameters for $MAPbI_3$. These results are compared to previous works. Also, we study the impact of cation on charge carrier mobility in halide perovskites for other thin films with different cation composition.

Time Domain and DC Mobility at various Temperatures

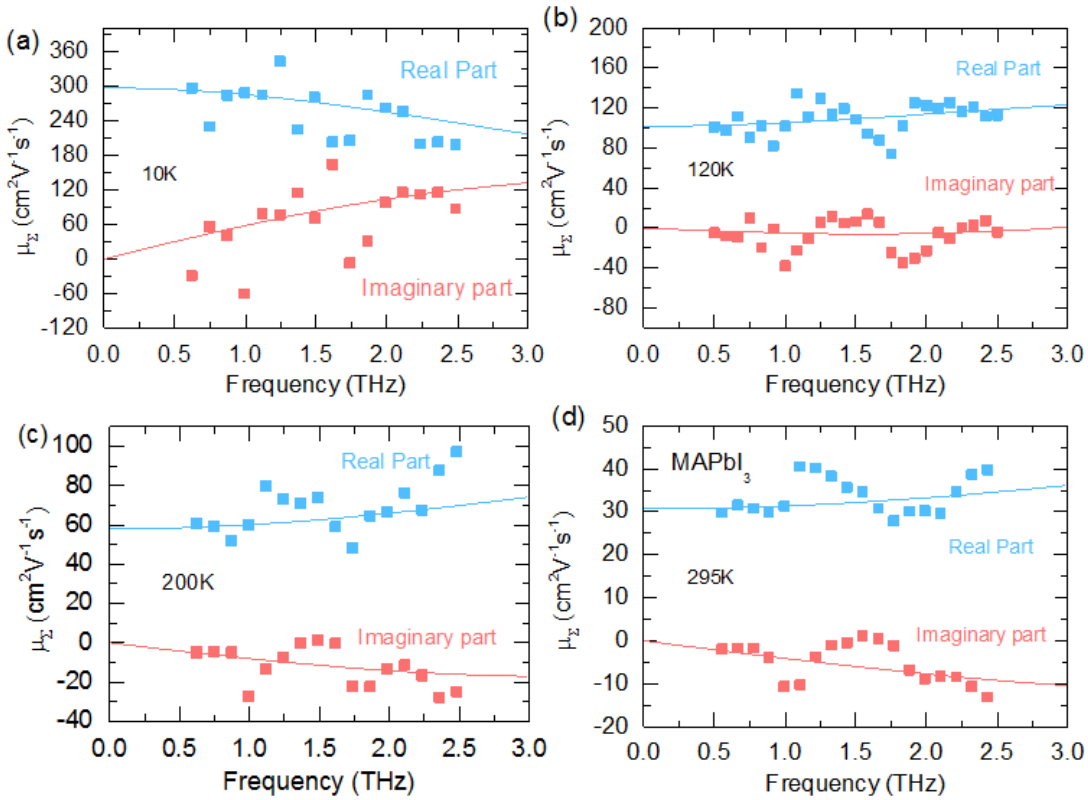

Figure 4.6. The real and imaginary parts of mobility spectra for $MAPbI_3$ with imposed above fitting curves at temperatures 10K (a), 120K (b), 200K (c)and 295K (d).

To investigate the transport properties in $MAPbI_3$ further in more detail, we recorded the mobility spectra in the range of temperatures between 10 and 295 K. The mobility spectra for $MAPbI_3$, recorded at 10 ps after excitation at temperatures 10 K, 120 K, 200 K and 295 K with

imposed fits above are shown in *figure 4.6*. The mobility spectrum at 10 K reveals signs of Drude-like behavior: the imaginary part is positive and it keeps growing with frequency while the real part of mobility exhibits a decrease. Furthermore, the applied Drude model suits well the experimental data thereby supporting the idea of free charge carrier motion at low temperatures. However, with increase in temperature the real part of mobility starts increasing with frequency and the imaginary part becomes negative, indicating a presence of localized charge carriers at higher temperatures. Furthermore, the phonon features, described in the **section "Phonons modes in the low THz range"**, are becoming more prominent with increase of temperatures.

In order to describe quantitatively the mobility behavior, we applied the modified Drude-Smith model for mobility spectra at 120 K, 200 K and 295 K. The modeling was performed by varying the scattering time τ, parameter c_1, localization length L and diffusion time t. The effective mass was set to the literature value $m_{eff} = 0.2m_0$ [76–78]. The fit results are given in *table* 4.3. The negative values of the parameter c_1 stand for the localization of charge carriers. Also the signs of localization reveal the localization length (parameter) L, that gradually drops from 7.4 nm at 120 K to 5 nm at 295 K.

*Table 4.3. Parameters of Drude and modified Drude-Smith for $MAPbI_3$ with **fixed** effective mass $m_{eff} = 0.2m_0$.*

T, K	*τ, fs*	c_1	μ_{DC}, $cm^2V^{-1}s^{-1}$	μ_t(time-domain), $cm^2V^{-1}s^{-1}$	*t, fs*	*L, nm*
10	34	0	299.2	279	-	-
120	28.2	0.6	93.4	103	70.1	7.4
200	18.7	-0.65	57.3	61.1	53.5	6.6
295	8.4	-0.6	30.2	33.5	36.9	5

The DC mobilities obtained from the modeling (fit) μ_{DC} and the THz pulse in time domain μ_t are also shown in *table 4.3* and in *figure 4.7 (a)*. As it is possible to see from the table, the mobility values determined by two different methods are in good agreement in a broad range of temperatures. Although it is known that at approximately 160 K the perovskite structure in $MAPbI_3$ undergoes a transition from the orthorhombic phase into the tetragonal phase, no clear influence of this transition on the mobility can be observed. The decreasing character of mobility with temperature indicates band-like transport in the materials, i. e. the scattering at phonons is a source of mobility reduction with temperature. Thus, summing up all above, if the

scattering at phonons is likely to be main scattering mechanism that limits the mobility in HPs, then we may conclude that localization of charge carriers at room temperatures may occur due to charge carriers-phonon coupling or polaron formation in $MAPbI_3$ thin film. The detailed analysis of scattering at phonons will be given in the next section.

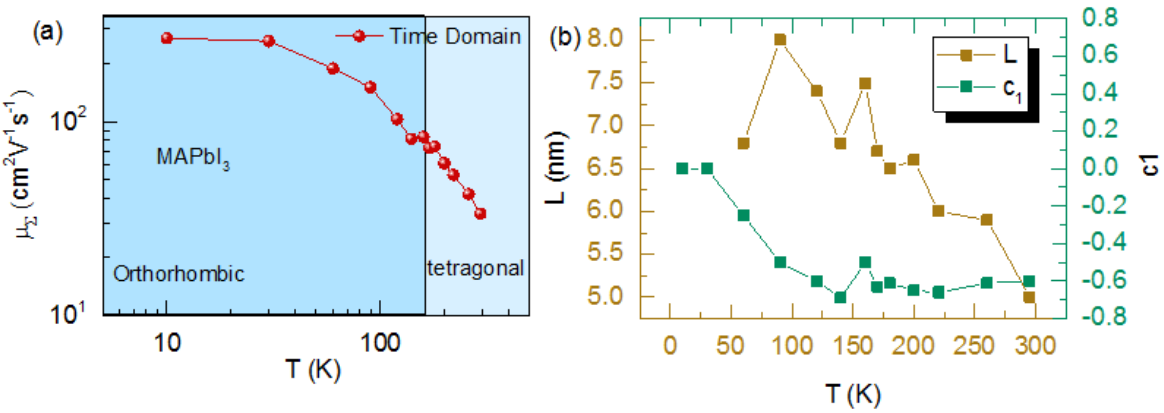

Figure 4.7. The dependence of mobility (a) and modified Drude-Smith fit parameters (b) in $MAPbI_3$.

4.6. Modeling of charge carrier mobility

The further sections represent the analysis of temperature dependent mobility in halide perovskites. The analysis is split into two parts: the analysis of temperatures at room temperatures by scattering at LO optical phonons and polaron formation and then analysis of mobility at low temperatures by scattering at acoustic phonons, impurities, and exciton.

Scattering at LO optical phonons

Charge carrier transport at room temperatures in many well studied polar semiconductors such as InP and GaAs is strongly impacted by scattering at LO optical phonons that are associated with vibrating dipoles at lattice nodes. Therefore, to explain the limitations of charge carrier mobility in halide perovskites, a number of authors applied Boltzmann transport theory for scattering at LO optical phonons [22,25,89]or the polaron theory[20,21,90,91] that is also based on interactions of charge carriers with LO optical phonons. The basic background of Boltzman transport and polaron theories are given in **chapter 2**.

The characteristic mobility for optical phonons is given by *equation (2.14)* in the **chapter 2**. As seen from *equation (2.14)*, the dielectric properties, LO optical phonons energy and effective mass of charge carriers are the key quantities that determine the electron- phonon

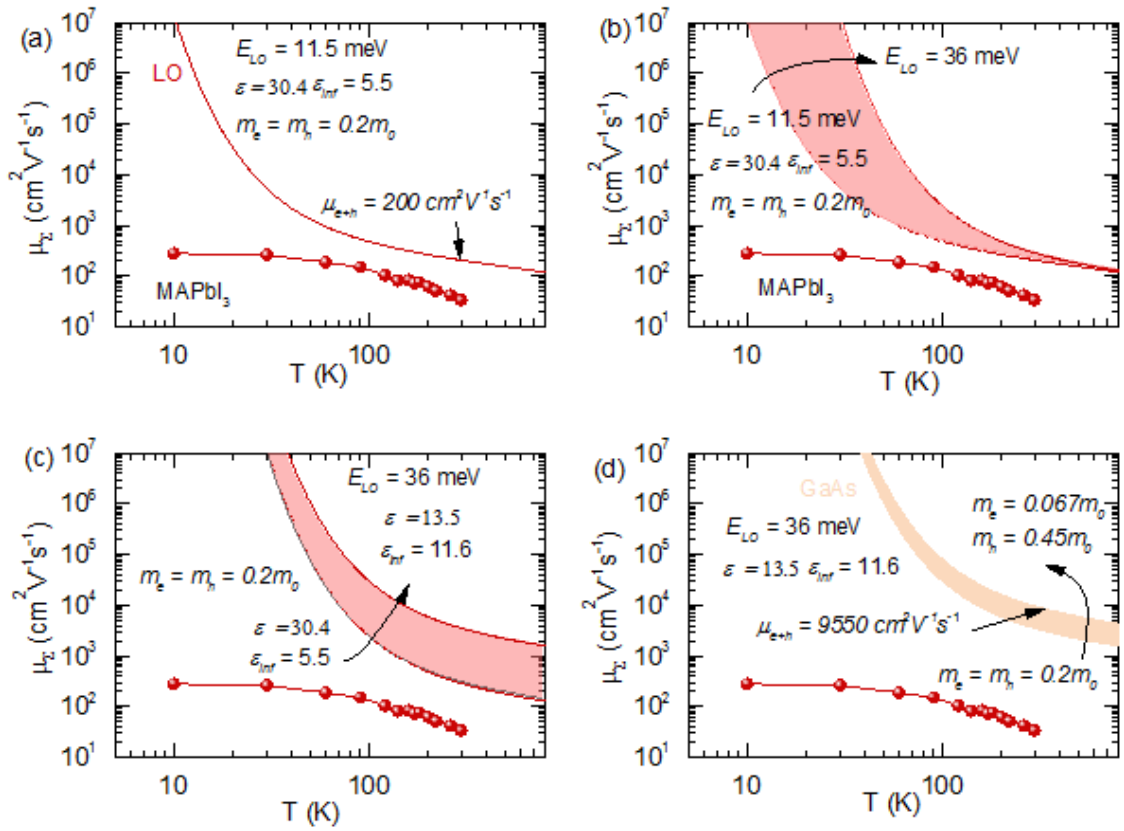

Figure 4.8. Sum of electron and hole mobility in $MAPbI_3$ scattered at LO optical phonons (a) and transformation of mobility at LO optical phonons from $MAPbI_3$ to GaAs by varying the LO phonon energy (b), by varying the dielectric constants (c), by varying effective mass (d).

interactions and thereby strongly influence the mobility. Many studies on dielectric properties in MHPs have revealed the large aspect ratio between static and high-frequency dielectric constants[21,64]: average static (ionic) dielectric constant ε = 30.4 and high-frequency (electron) dielectric constant ε_∞ = 5.5. Furthermore, the LO optical phonon energy is around 11.5 meV[64] what is several times lower than in standard semiconductors such as InP ($\hbar\omega_{LO}$= 38.2 meV)[51] and GaAs ($\hbar\omega_{LO}$ = 36)[35]. Also some works[76,92,93] deal with DFT calculation of the band structure in HPs and determined the effective masses from the curvature of the band minima of the conductance band for electrons and from maxima of the valence band for holes. The results show identical effective masses for electrons and holes, varying from $0.1m_0$ to $0.3m_0$.

For calculation of mobility on LO optical phonons we set the following values from the literature[64]: static (ionic) dielectric constant ε = 30.4, high-frequency (electron) dielectric constant ε_∞ = 5.5, energy of LO optical phonons $\hbar\omega_{LO}$ = 11.5 meV and average effective mass m =$0.2m_0$ for electrons and holes. All of the parameters are also summarized in *table 4.4*. Since we measure the sum of electron and hole mobility in the OPTP experiment and the incoming

parameters, specified above, are common for electrons and holes, then final sum of mobility is just doubled mobility given by *equation (2.14).*

Figure 4.8 (a) illustrates the calculated results. The LO optical phonon mobility decreases with temperature and starts approaching the experimental data at temperatures above ~ 130 K when the LO optical phonon density starts increasing at $T \geq \hbar\omega_{LO}/k$. The obtained sum of electron and hole mobility at room temperature is around 200 $cm^2V^{-1}s^{-1}$.

The problem of modest mobilities in MHPs compared to standard compound semiconductors was of large concern so far. However, the difference in mobilities may be quite easily explained within the concept of electron – LO optical phonon interactions by comparing available in the literature dielectric constants, optical phonon energies and effective masses for MHPs, given above, and for any standard semiconductor, for instance, GaAs.

The LO optical phonon energy determines the phonons density $n(\hbar\omega_{LO}/kT) = 1/\left(e^{\frac{\hbar\omega_{LO}}{kT}} - 1\right)$ and threshold temperature $T_{th} \geq \hbar\omega_{LO}/k$ below which the phonon density starts drastically decreasing. It is known that the LO optical phonon energy for GaAs is $\hbar\omega_{LO}$ = 36 meV[35] what exceeds several times the LO optical phonon energy 11.5 meV for MHPs. Larger energies results in lower phonon density and higher mobilities for GaAs at fixed temperatures as it shown in the *figure 4.8 (b).* At temperatures $T_{th} \geq \hbar\omega_{LO}(GaAs)/k$ = 418 K the difference in mobility is not so prominent anymore. Thus, LO optical energy has a stronger impact on mobility at lower temperatures and the difference vanishes at higher temperatures, when the phonon densities for both materials become rather equal.

While the energy of optical phonons affects the low temperature range of mobility, dielectric constants and effective mass have an impact on mobility rather at room (higher) temperatures. So, for instance, the static and high-frequency dielectric constants in GaAs are ε = 13.6 and $\varepsilon_\infty = 11.5$[35], respectively. The further substitution of the dielectric constants for GaAs into *equation (2.14)* shows (see *figure 4.8 (c)*) that high temperature mobility are strongly impacted by the dielectric properties and the lower aspect ratio between static and high-frequency dielectric constants (the lower difference in dielectric constants) leads to increase in mobilitiy.

The effective masses of electrons and holes in GaAs are $m_h = 0.45m_0$ and $m_e = 0.067m_0$[35], respectively. Even though the holes are much heavier than electrons, the total mobility tends to increase at fixed temperature after substitution of these values into *equation (2.14)* as shown in

the *figure 4.8 (d)*. Hence, since the effective masses in MHPs vary between 0.1 and 0.3 m_0[76–78] in in literature, these discrepancies also result in deviations of mobility.

Table 4.4. Parameters used for calculation of mobility in $MAPbI_3$.

Quantity	**$MAPbI_3$**
Dielectric constant ε	30.4 [64]
High frequency dielectric constant ε_∞	5.5 [64]
LO Phonons energy $\hbar\omega_{LO}$	11.5 meV [64]
Electron effective mass m_e/m_0	0.2 [78]
Hole effective mass m_h/m_0	0.2 [78]
Density ρ	4.15 g/cm^3 [94]
Sound velocity v_s	3100 m/s [22]
Deformation potential E_1	2.5 eV [95]
Piezoelectric constant p	0.38 C/m^2 [96]

The obtained LO optical mobility in GaAs at room temperatures is around 9550 $cm^2V^{-1}s^{-1}$ that is very close to experimental results 8900 $cm^2V^{-1}s^{-1}$ [35]. The good agreement between experimental and theoretical results thereby suggests that the charge carrier mobility in GaAs is limited by scattering of charge carrier – LO optical phonons at room temperatures.

On one hand, the large aspect ratio in dielectric constants, low LO optical phonon energy and higher effective masses explains why the mobility in halide perovskites are expected to be at least one order of magnitude lower than in standard compound semiconductors. However, on another hand, the calculated mobility from scattering at only LO optical phonons in $MAPbI_3$ is around 200 $cm^2V^{-1}s^{-1}$what is still much higher than the ones obtained from the experiment 33.5 $cm^2V^{-1}s^{-1}$. The lower values of mobility from experiments suggests that alongside with

interaction with LO optical phonons some other mechanisms or effects should be taken into consideration in order to completely explain the reduction of charge carrier mobility at room temperatures. For instance, the polaron formation, Rashba effect and anharmonicity in perovskites structure are examples of such mechanisms. Therefore, the next sections are aimed to give an insight into these mechanisms in details.

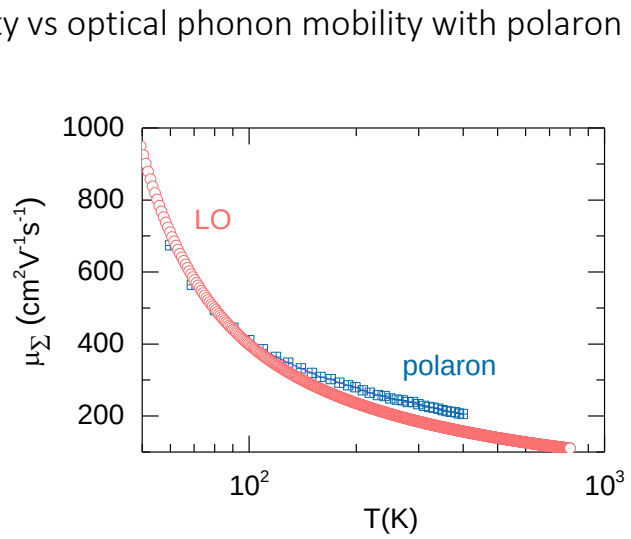

Figure 4.9. Comparison of polaron and LO optical phonon mobility calculated with parameters taken from paper (Frost, 2017)[20].

The theoretical background of polaron theory is given in **chapter 2**. Polaron theory was one of the first models proposed to explain the limited mobilities in MHPs. According to polaron theory electron (hole) by moving in the polar crystal polarizes medium near itself and start interacting (or get trapped in) with self-induced electric field. The strength of these interactions may be described by Fröhlich coupling constant α and given by *equation (2.28).*

Our studies of the temperature dependency of mobility in thin films reveal a clear tendency of decrease in mobility with temperature. Also, our results are supported by other authors[8,61,64,66–69] who showed the same mobility behavior with temperature. Moreover, recent studies[20,21,64] reveal the modest values of coupling constants. Such a mobility behavior and modest coupling constants values indicate that large polaron formation is likely to form in MHPs.

There are several authors[20,21,91], who calculated the polaron mobility in halide perovskites. All of these works are based on the calculation of mobility by Hellwarth equation, given by *equation (2.36)*, that is in general based on solving the Feynman path integral and minimization of variation parameters. This is in general a complicated method.

Table 4.5. Summarizing Polaron parameters calculated in the (Frost, 2017)[20] and in this thesis.

Materials	m/m_0	ε	ε_∞	$\hbar\omega_{LO}$, **meV**	m_p/m_0	α	μ_H, **$cm^2V^{-1}s^{-1}$**	μ_{LO} **with polaron effective mass, $cm^2V^{-1}s^{-1}$**
$MAPbI_3$ (Frost, 2017)[20]	0.12 (e) 0.15 (h)	4.5	24.1	9.30	0.16 (e) 0.21 (h)	2.39 (e) 2.68 (h)	136 (e) 94 (h)	184 (this work)
$MAPbI_3$ (this work)	0.20[78] (e and h)	5.5[64]	30.4[64]	11.50[64]	0.28	2.35	-	131 (this work)

Since a large polaron is regarded as a free electron (hole) with enhanced effective mass, given by *eq. (2.29)*, and undergoes the scattering at LO optical phonons in the crystal, we assume that Hellwarth equation of polaron mobility can be approximated by *equation (2.14)* of LO optical phonons mobility, obtained within Boltzmann transport theory, provided the charge carrier effective mass is regarded as a polaron effective mass according to *equation (2.29)*. To validate this assumption, we took the dielectric properties, effective masses and LO optical phonon energies as they were used for calculation of the polaron mobility in the work (Frost, 2017)[20]: static ε = 4.5 and high-frequencyε_∞= 24.1 dielectric constants, effective mass $m_e = 0.12m_0$ for electrons and $m_e = 0.15m_0$ for holes, optical phonon energies $\hbar\omega_{LO}$ = 9.30 meV. Then we substituted them into *equation (2.14)*. Instead of charge carrier effective mass we used the polaron effective mass m_p with coupling constants α_e= 2.39 for electrons and α_h= 2.69 for holes calculated by Frost[20].

In *figure 4.9* we show the results. As seen, the mobilities calculated by two different approaches yields rather similar results at lower temperatures and with increase in temperature the mobilities start deviating from each other, wherein mobility at the LO optical phonons yields lower values at room temperatures. The estimated polaron mobility by Frost is 240 $cm^2V^{-1}s^{-1}$ [20]and the mobility at LO optical phonons with polaron effective mass is 184 $cm^2V^{-1}s^{-1}$ what is a bit lower than predicted by Hellwarth equation. Nevertheless, the mobilities, estimated by these two approaches at the same incoming parameters, yield quite close results in a broad range

of temperatures and despite the deviations at room and higher temperatures the mobility at LO optical phonons can be used to estimate the polaron mobility without involving complicated calculations of Feynman path integral and variation of parameters in Hellwarth formula. For that reason, for the further calculation of the polaron mobility we will for simplicity use the polaron effective mass, approximated by *equation (2.14)*.

Since the parameters, used by Frost for polaron mobility, differ from the ours, that we use for mobility calculation in this thesis, we also calculate the polaron mobility for parameters from *table 4.4*. . For electron and hole effective masses $m = 0.2m_0$, static $\varepsilon = 30.4$ and high-frequency dielectric constants $\varepsilon_\infty = 5.5$ and LO phonon energy $\hbar\omega_{LO}$= 11.5 meV, the resulting mobility is 131 $cm^2V^{-1}s^{-1}$. *Table 4.5* summarizes the parameters, used for calculations in the thesis and in the work (Frost, 2017)[20] as well as obtained mobilities.

Even though the polaron model describes better the mobility at room temperatures than Boltzmann theory of scattering at LO optical phonons, but the resulted mobility is still far from experimental values. Alongside with interaction of charge carriers with LO optical phonons the further mechanisms such as Rashba effect[25], Dynamic Disorder[26] or Dielectric Dragg[24] were considered. *Figure 4.10* shows the comparison of results in this work and other approaches available in the literature for $MAPbI_3$. It is clearly seen from figure that including of additional effect, whether polaron with enhanced effective mass, Rashba effect or Dynamic Disorder, to the scattering at LO optical phonons, results in further reduction of mobility. In spite of all of the discrepancies due to the input parameters in calculations all these models still set upper limit of mobilities above 100 $cm^2V^{-1}s^{-1}$ at room temperature with the lowest mobilities obtained for Dynamic Disorder 135 $cm^2V^{-1}s^{-1}$ and for scattering at LO optical phonons with polaron effective mass in this work 131 $cm^2V^{-1}s^{-1}$. *Table 4.6* summarizes the mobility values obtained by various theoretical approaches.

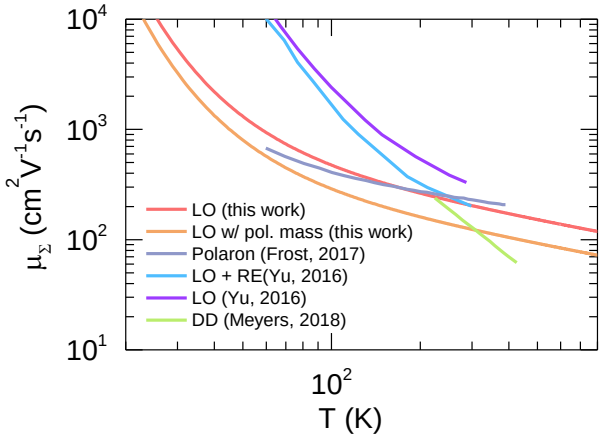

Figure 4.10. Comparison of temperature dependencies of mobility in $MAPbI_3$ in this work and in literature. The abbreviations RE stands for Rashba effect and DD stands for Dynamic Disorder.

Table 4.6. The mobilities in $MAPbI_3$ at room temperatures estimated by various approaches .

Mechanism	*Mobility, $cm^2V^{-1}s^{-1}$*
LO (this work)	200
LO w/ polaron effective mass (this work)	131
Polaron	240[20]
LO + Rashba Effect	200[25]
Dynamic Disorder	135[26]
Experiment (this work)	33.5

Scattering at acoustic phonons

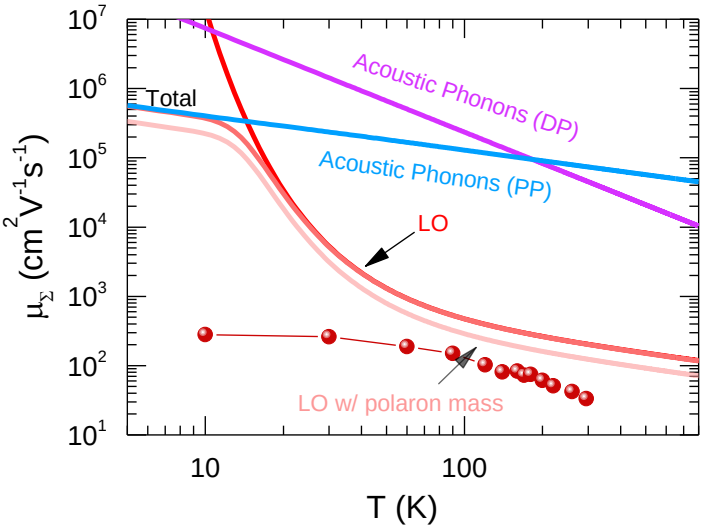

Figure 4.11. The sum of electron and hole mobility calculated on polaron, LO optical and acoustic phonons.

The early studies[61,97,98] on charge carrier transport in MHPs in a broad range of temperatures were based on power law modeling of the temperature dependent mobility T^m with m = -1.6 - -1.4 what is very close to m = -1.5, typical mobility behavior of charge carrier scattered at acoustic phonons of deformation potential. However, more recent research works[22,64,99], and it is also supported with our results from the previous section, show that room temperature mobility is rather influenced by electron – LO optical phonons interaction. However, acoustic phonons have usually low energy of a few meV and therefore it does not have such a steep decay with temperature, compared to optical phonons. Therefore, they may have an impact on charge carrier mobility at lower temperatures. There are only a few works[23,65,25] conducted by considering the scattering at acoustic phonons of deformation potential and, to our best knowledge, there are no any studies on acoustic phonons of piezoelectric potential. That is why, in this section we provide with mobility on acoustic phonons of both types by using the quantities known from literature.

For the calculation of mobility according to *equations (2.16)* and *(2.18)* we took the following parameters from literature for $MAPbI_3$: deformation potential E_1 = 2.5 eV[95], density ρ = 4.15 g/cm^3 [94], speed of sound v_s = 3100 m/s [22], piezoelectric constant p = 0.38 C/m^2 [96], dielectric constant ε = 30.4 [64], electron and hole effective mass m = 0.2m_0 [64]. *Table 4.4* summarizes the used for calculation quantities from literature and references for them.

Figure 4.11 shows the temperature dependency of mobility, calculated on optical and acoustic phonons and their total mobility, calculated according to Matthiessen rule, given by

equation (2.26). The resulting temperature-dependent mobility on acoustic phonons of both potentials predicts the room temperature mobility of around 10^4 $cm^2V^{-1}s^{-1}$ what is more than 2 orders of magnitude higher than measured values. Due to the low energies of acoustic phonons, the density of acoustic phonons does not decay so fast with temperature compared to optical phonons and thereby the scattering at acoustic phonons is not prohibited even at very low temperatures. However, considering only scattering at optical and acoustic phonons, the total mobility, dominated by acoustic phonons, is of 10^6 $cm^2V^{-1}s^{-1}$ for piezoelectric potential and 10^7 $cm^2V^{-1}s^{-1}$ for the deformation potential at 10 K. These values also exceed far the measured experimental values. The scattering at acoustic phonons piezoelectric potential results in lower mobility at low temperatures compared to scattering at deformation potential due to weaker dependency on temperature $\mu_{APP} \sim T^{-1/2}$ vs $\mu_{ADP} \sim T^{-3/2}$for piezoelectric constant p = 0.38 C/m^2 [96]. There are also some other works[22,23,65] that considered the scattering at acoustic phonons. So, for instance in the work (Mante et al., 2016)[23] the estimated mobility is 2800 $cm^2V^{-1}s^{-1}$ for electrons and 9400 $cm^2V^{-1}s^{-1}$ for holes at room temperature. The sum of these values is in good agreement with our results.

All stated above suggests that scattering at acoustic phonons does not seem to be the dominating scattering mechanism in $MAPbI_3$ neither at room temperature nor at low temperatures. The total mobility at room temperatures is likely to be limited mostly due to Fröhlich interactions and the mobility at low temperatures should be impacted by some other mechanisms such as impurities and/or exciton formation that will be discussed in detail in the next sections.

Scattering at ionized impurities

A number of studies have shown the presence of charged point defects in halide perovskites[100,101] that may be treated as charged impurities and thereby may be considered as scattering centers for mobile charge carriers. The scattering at impurities has a specific temperature behavior compared to scattering at phonons. As it was shown in the previous section, the scattering at phonon has band-like transport properties and the mobility, or scattering time, decreases with increase in temperature. Scattering at impurities is controversial: it reveals rather hopping transport (charge carrier hop off from one scattering site to another) and thereby the mobility is growing with temperature. The mobility for charge carrier scattered at charged impurities is given by *equation (2.22)*. Therefore, scattering at ionized impurities limits the charge carrier transport at low temperatures when the phonon population density is

low (no scattering at phonons). To our best knowledge, only a few authors[65,89] performed the calculation at ionized impurities.

In this work we use the Brooks-Herring approach as the one that takes into account the screening of the surrounding environment. The theoretical background is described in the **chapter 2**.

For calculation of mobility at ionized impurities we have used effective masses and static dielectric constants as specified in the previous sections and varied the impurity densities n_I =10^{16}, 10^{17} and 10^{18} cm^{-3}. We assumed charge number $z = 1$. Moreover, it is important to point out that factor F_{BH} is dependent on charge carrier concentrations n_e and it has usually a weak dependency with temperature under constant charge carrier concentrations and dielectric properties. However, at low temperatures the charge carrier concentration may drastically drop due to exciton formation and thereby may strongly influence the factor F_{BH}. Therefore, we took into account the reduction of charge carrier concentration with temperature that obey to Saha equation given in the **chapter 2** of this thesis by *equation (2.41)*. The detailed description of exciton on mobility is given in the next section.

Figure 4.12 (a) shows the mobility for ionized impurities at various impurity density, optical LO phonons and their total mobility, obtained according to the Mattheissen rule. As expected, the decrease in the impurity density results in reduction of mobility. At impurity concentration n_I =10^{16} cm^{-3} the mobility is around 9900 cm^{2}V^{-1}s^{-1} and it decreases up to 100 cm^{2}V^{-1}s^{-1} at impurity concentrations n_I =10^{18} cm^{-3} at 10 K. Hence, the impurity density 8·10^{17} cm^{-3} fits well the experimental value of mobility 280 cm^{2}V^{-1}s^{-1} at 10 K. However, if the scattering at low temperatures were impacted only by scattering at ionized impurities, the mobilities at 40 K would constitute roughly 1000 cm^{2}V^{-1}s^{-1} what is not observed in the experiment. Thus, it makes highly unlikely scattering only at ionized impurities at low temperatures and some other mechanisms should be taken into account. Therefore, to explain the mobility behavior at low temperatures we took into account the scattering at neutral impurities.

Scattering at neutral impurities

Scattering at neutral impurities was neglected so far mostly due to low scattering cross-section compared to ionized impurities. However, due to its relatively weak dependency on temperature, the neutral impurities together with ionized impurities may explain the mobility

behavior in the low temperature range. The scattering at neutral impurities is described in detail in the **chapter 2**.

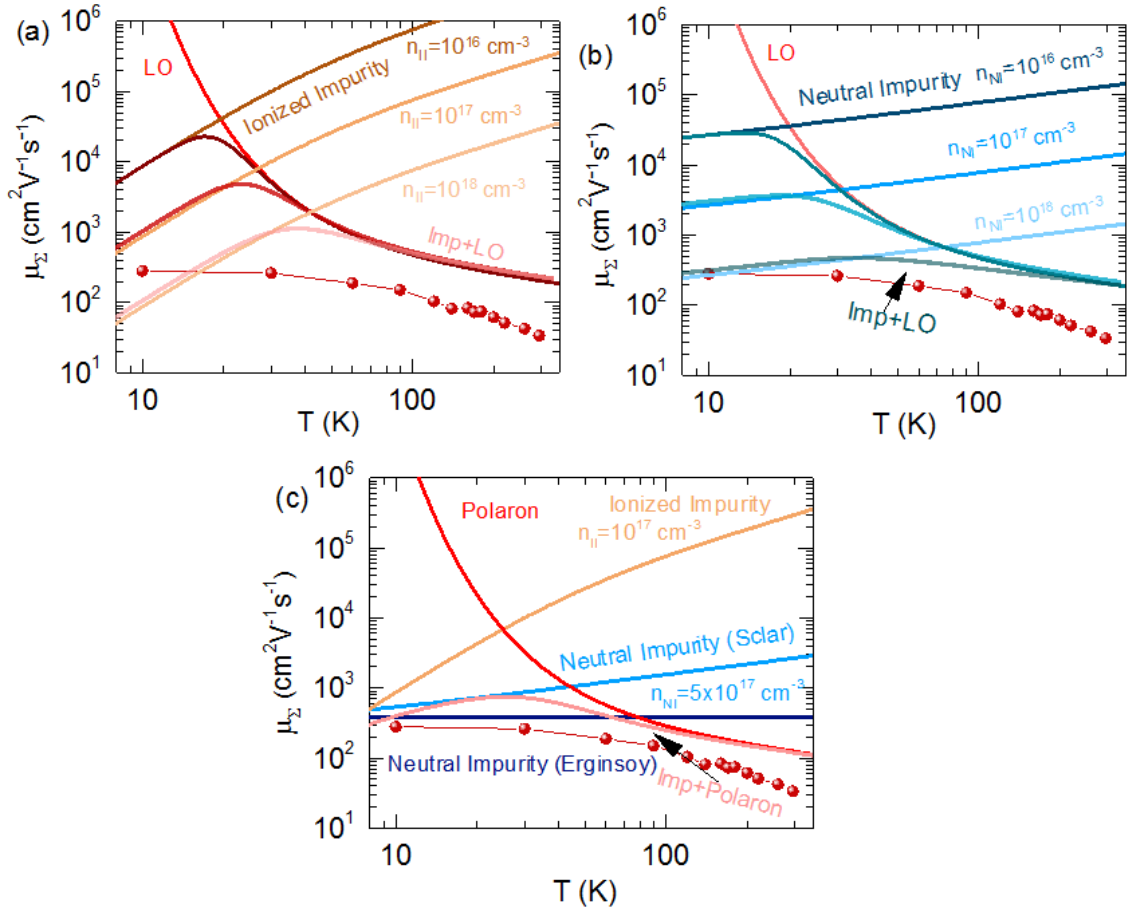

Figure 4.12. The electron and hole mobility in $MAPbI_3$ scattered at ionized and LO optical phonons (a), at neutral impurities and LO optical phonons (b) and at ionized, neutral and polaron (LO optical phonons with polaron effective mass) (c) at various impurity concentrations.

In *figure 4.12 (b)* we show the calculated Sclar mobility, given by *equation (2.25)*, at various neutral impurity densities n_{NI}. As it is seen from the figure, the mobility ranges from 10^2 to 10^4 cm^{2}V^{-1}s^{-1} for densities 10^{16} – 10^{18} cm^{-3} and has the same range of magnitude as for ionized impurity scattering by Brooks-Herring formula. The mobility temperature behavior $\sim T^{0.5}$ increases less steeply with temperature compared to ionized impurity scattering $T^{1.5}$ and it fits well the mobility in the range 20 - 80 K at $n_{NI} \cong 10^{18}$ cm^{-3}. Moreover, the estimated charged and neutral impurity densities ~10^{18} cm^{-3} are in good agreement with point defect concentrations 10^{18} cm^{-3} in halide perovskites obtained by Polyakov[102]. Thus, both ionized and neutral impurities together seem to explain the mobility behavior at low temperatures at impurity concentrations in the range between 10^{17} - 10^{18} cm^{-3}. The *figure 4.12 (c)* demonstrates the total mobility in $MAPbI_3$ calculated at ionized, neutral impurities and LO optical phonons with polaron effective mass that guarantees the best fit to the experimental values of mobility

in a broad temperature range. The dark blue curve in the *figure 4.12 (c)* indicates the Erginsoy mobility that does not depend on temperature.

Exciton influence on mobility

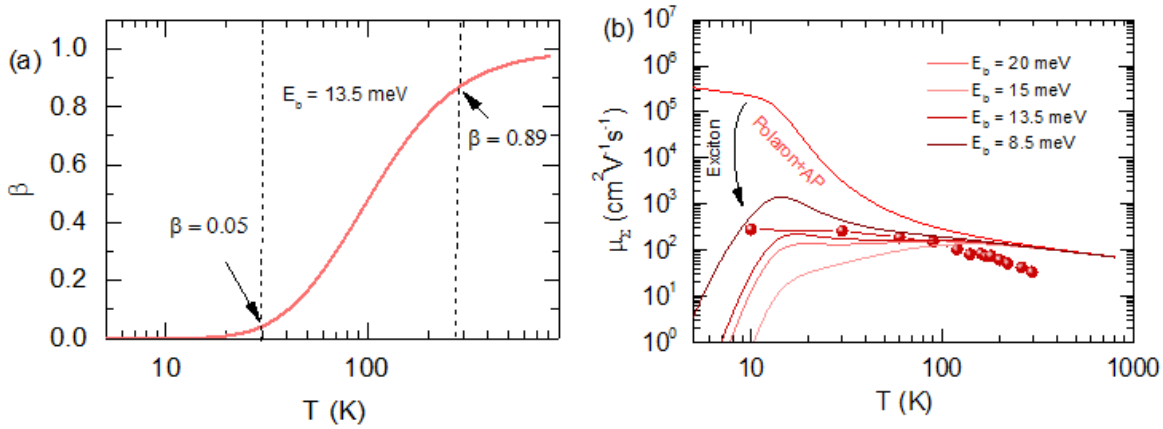

Figure 4.13. (a) The reduction of free charge carrier concentration β with temperature at exciton binding energy E_b = 13.5 meV according to Saha equation. (b) charge carrier concentration – mobility product $\beta\mu_\Sigma$ at various exciton binding energies. The mobility μ_Σ is calculated by scattering at acoustic (AP) and LO optical phonons with polaron effective mass (Polaron).

Band edge excitation of electrons in semiconductors may result in bound electron-hole states, called excitons, that interact via Coulomb interactions. The binding energy of excitons is determined by effective mass of exciton and the relative dielectric constant of the medium where the exciton was formed. In the literature one may find a great deal of various values of the binding energies for $MAPbI_3$ that may vary from a few meV to some tens of meV[33,103,104]. This is due to that the dielectric function for halide perovskites in the low THz range has many resonances[105,106] resulting from metal-halide vibrations that were described in the first section of this chapter and thereby it reveals a large aspect ratio between static and high-frequency dielectric constants. The average values of binding energy in $MAPbI_3$ is around 11-16 meV[33,103] at room temperatures. At such binding energies the exciton at room temperatures and low injection levels will dissociate into free electron and holes.

However, with decrease in temperature the phonon population and energy is decreasing and the exciton becomes more stable leading to increase of exciton fraction at low temperatures. Thus, the population of free charge carriers and excitons must be carefully taken into account especially at low temperatures and it may strongly influence the charge carrier mobility, that is

a merit of difference in transmission of THz field of excited and unexcited thin film in the OPTP experiment.

The population density (faction of free charge carrier to total injected density) may be calculated according to Saha formula[33], given by *equation (2.41)*.

First, we can estimate the total injected electron-hole density after excitation $n_{tot} = AN_{ph}/d$ where A is an absorbed fraction of incident light at excitation wavelength λ, $N_{ph} = P_{pump}f_{rep}\lambda/S\hbar c$ is a photon density per area S at the excitation wavelength λ for excitation pump power P_{pump} at the laser repetition rate f_{rep} and d is a thickness of the thin film. For excitation power $P_{pump} = 6$ mW with f_{rep} =150 kHz repetition rate, wavelength λ =400 nm, thin film thickness d =500 nm, pump beam radius 0.15 cm and absorbance A =0.72 for $MAPbI_3$, obtained from UV-vis measurements, the total injected charge carrier density yields n_{tot} =3.4·10^{16} cm^{-3}. For these concentrations and binding energy $E_b = 13.5$ meV, a fraction of free charge carriers is $\beta = 0.89$ at room temperature and $\beta = 0.05$ at 30 K as it is shown in the *figure 4.13 (a)*. It means that at low temperatures free electrons and holes may get into bound states and form excitons.

Since THz Spectroscopy is sensitive to free charge carriers, then we assume that THz mobility of exciton is approximately equal to zero $\mu_{exc} \approx 0$. Therefore, we assume that only free charge carriers (electrons and holes) contribute to mobility and, thus, in this case the total THz mobility is proportional to the charge carrier concentration $\beta(T)$, determined from Saha *equation (2.41)*: $\mu_{\Sigma}(T) \approx \beta(T)\mu_{e+h}(T)$.

In order to prove the concept, we calculated the mobility scattered at acoustic and optical phonons according to Matthiessen rule and multiplied to charge carrier concentration: $\beta(T)[1/\mu_{AP}(T) + 1/\mu_{LO}(T)]^{-1}$. The number of electron – hole bound pairs (excitons) starts drastically increasing at temperatures below 100 K and thereby it may result in reduction of charge carrier mobility of around two orders of magnitude up to 10^2 – 10^3 cm^{2}V^{-1}s^{-1} at low temperatures. We also analyzed the mobility at various exciton binding energies. *Figure 4.13 (b)* demonstrates the total electron and hole mobility for optical and acoustic phonons at exciton energies 8.5, 13.5, 15 and 20 meV. It is quite clear that at higher binding energies and fixed temperature the concentration of free charge carriers is lower and thereby the mobility is lower according to our model. Thus, higher binding energies results in lower mobilities at low temperatures.

At room temperatures the exciton is unstable at calculated binding energies and the mobility is $\beta\mu_\Sigma$ does not differ from μ_Σ, calculated without taking into account the exciton formation.

4.7. Impact of cation compound on charge carrier transport

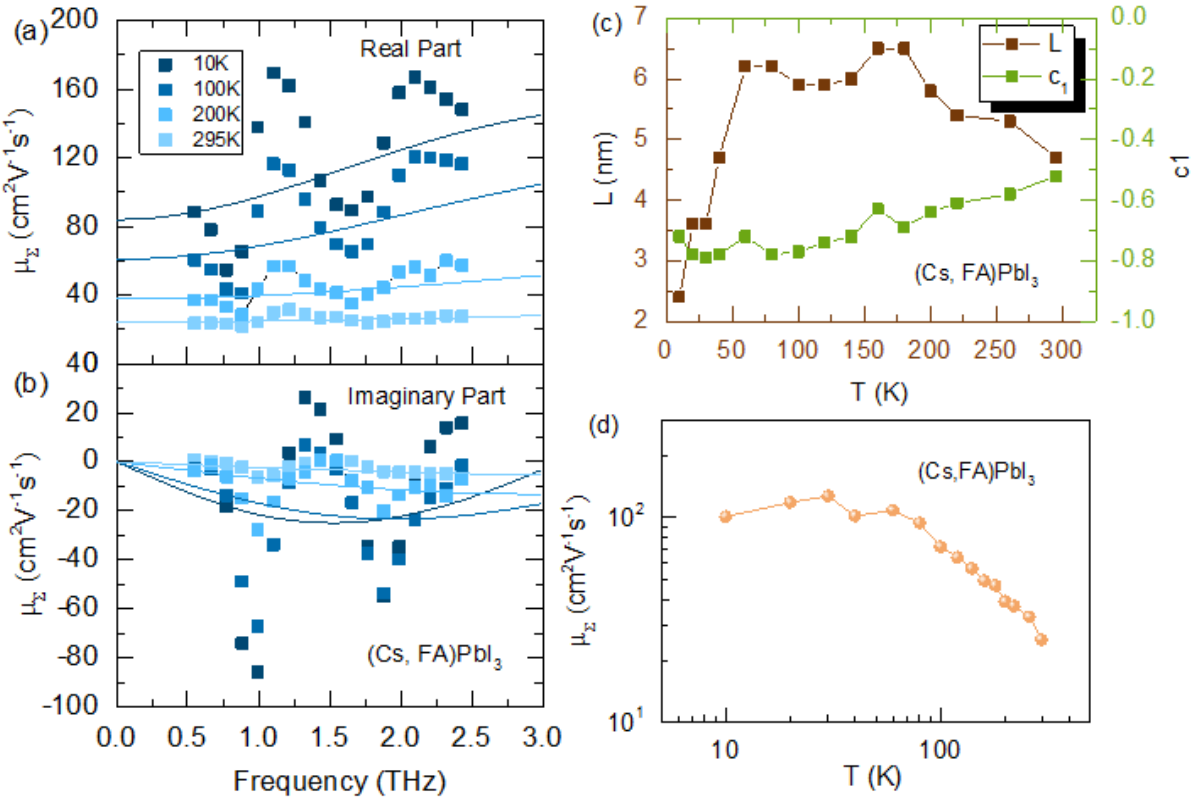

Figure 4.14. Real and imaginary parts of sum of electron and hole mobility in (Cs, FA)PbI$_3$ with imposed modified Drude-Smith fit on them at 10 K, 100 K, 200 K, 295 K ; (c) Variation of modified Drude-Smith localization length L and phenomenological parameter c_1 with temperature; (d) Sum of electron and hole mobility in (Cs, FA)PbI$_3$ with temperature.

The analysis of temperature-dependent charge carrier mobility in the previous section was conducted on $MAPbI_3$ thin film as the most well studied halide perovskite material. However, it is known that $MAPbI_3$ suffers from thermal stability, degradation and light-induced halide segregation, undergoes phase transition at near room temperatures and the record efficiency for $MAPbI_3$ single crystal solar cells is now 21.092 %[107]. In order to overcome these issues for the last years of active research some other halide perovskites counterparts with organic,

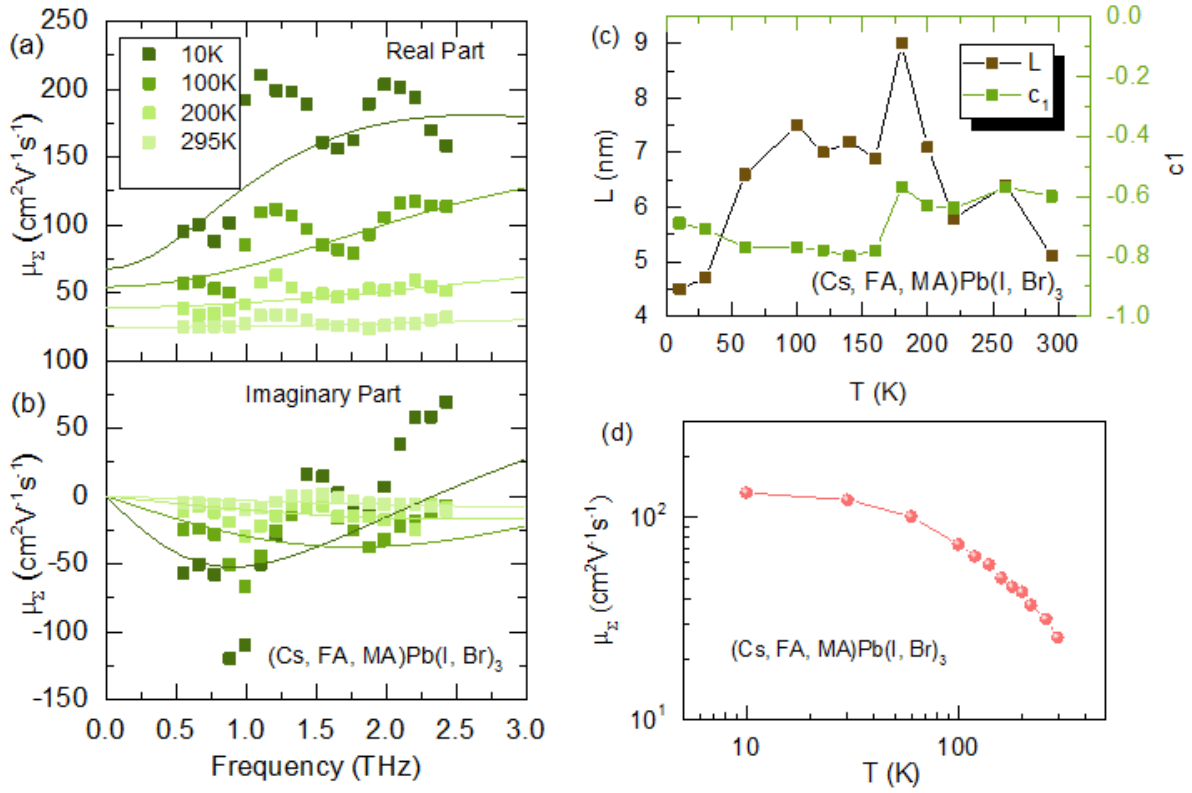

Figure 4.15. Real and imaginary parts of sum of electron and hole mobility in (Cs,FA,MA)Pb(I,Br)$_3$ with imposed fit on them at 10 K, 100 K, 200 K, 295 K ; (c) Variation of modified Drude-Smith localization length L and phenomenological parameter c_1 with temperature; (d) Sum of electron and hole mobility in (Cs,FA,MA)Pb(I,Br)$_3$ with temperature.

inorganic and mixed cations were developed with enhanced optoelectronic properties, thermal stability and higher efficiency[108]. In this section we aim to investigate the impact of cation on charge carrier mobility in MHPs. Along with $MAPbI_3$ thin film we had the following polycrystalline thin films: $(Cs,FA)PbI_3$, $(Cs,FA,MA)Pb(I,Br)_3$ produced by Dr. Martin Stolterfoht in the group Prof. Neher at Potsdam University and $CsPbI_3$ prepared in the group of Dr. Unold at the Helmholtz Zentrum Berlin. The detailed description and references on preparation are given in the section sample preparation of this chapter.

The THz mobility spectra for thin films were recorded at temperatures in the range from 10 K to 295 K. The spectra at 10 K, 100 K, 200 K, 295 K for $(Cs,FA)PbI_3$ and triple cation $(Cs, FA, MA)Pb(I,Br)_3$ are shown in the *figures 4.14 (a, b)* and *4.15 (a, b)* respectively. The mobility spectra for both of the thin films reveal similar behavior. The imaginary and real parts of

mobility at low temperatures are strongly dominated by phonon resonances at low temperatures, excited by THz field,

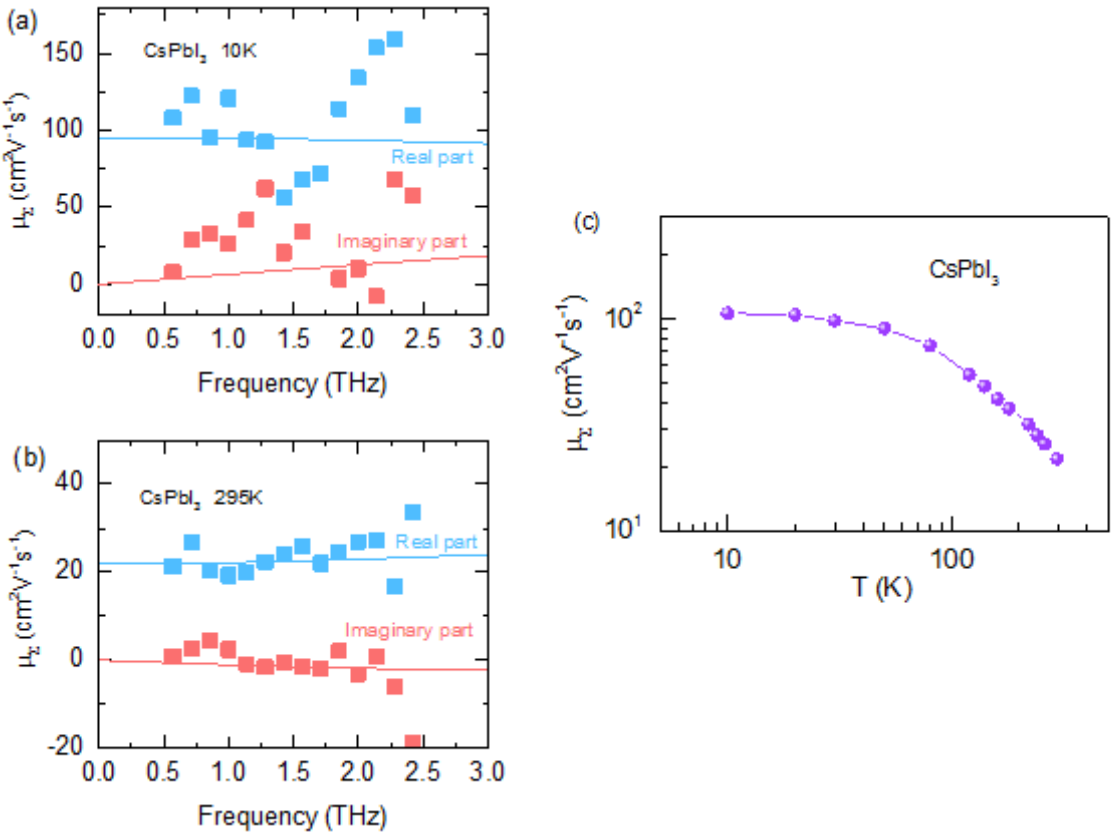

Figure 4.16. The real and imaginary parts of THz mobility in $CsPbI_3$ at 10 K (a) and 295 K (b), the temperature dependency of mobility (c).

what makes complicated the analysis of mobility spectra. However, despite the phonon features in the spectra, the upward shift of mobility spectra at low temperatures clearly indicates the increase of mobility with decrease in temperatures for both thin films. In contrast to $MAPbI_3$, applied modified Drude-Smith modeling of the mobility spectra in (Cs, FA)PbI_3 and (Cs, FA, MA)$Pb(I, Br)_3$ thin films shows more evident signatures of localization in a broad range of temperatures. It is seen from the values of phenomenological parameter c_1 that is negative for both thin films for all mobility spectra and with its maximum -0.52 for (Cs, FA)PbI_3 and -0.6 for (Cs, FA, MA)$Pb(I, Br)_3$ at room temperatures. Moreover, the localization at low temperatures is stronger and reaches its minimum -0.72 for (Cs, FA)PbI_3 and -0.69 for (Cs, FA, MA)$Pb(I, Br)_3$ at 10K. Such a different behavior of c_1 at low temperatures compared to $MAPbI_3$ may be explained by more complicated compound content of the thin films, when the uneven distribution of cation atoms may serve as additional scattering centers. The presence of localization at higher temperatures in turn may be explained by increasing electron-phonon

interactions or polaron formation. Interestingly, the values of localization length *L* are in range of 6-8 nm for the thin films and they start decreasing at 130-160 K with increase of temperature and reach 4.7- 5 nm at room temperatures what is very close to polaron radii calculated in some other works[20,21,90].

The mobility spectra for CsPbI3 were fully recorded at 10 K and 295 K, the rest of the OPTP measurement was performed by measuring at the THz pulse maximum due to large level of noise in the set-up. And then the mobility was determined from maximum of THz pulse in time domain. The *figure 4.16* shows the mobility spectra and the dependency of mobility on temperature. The noisy THz signal makes complicated the analysis of the mobility spectra at 10 K. However, it is seen from the *figure 4.16 (a)* that real part shows the slight decrease of mobility and imaginary part of mobility slight increase with imposed phonon features at around 1 and 1.6 THz. Also the analysis of the spectra by modified Drude-Smith model indicates rather Drude behavior of mobililty at 10 K, close to the mobility behavior in $MAPbI_3$ (free charge carrier motion). The room temperature mobility shows rather the fingerprints of localization with phenomenological parameter c_1 = -0.28 and very low relaxation time 3.5 fs. Thus, mobility behavior of fully inorganic $CsPbI_3$ and fully organic perovskite $MAPbI_3$ is quite identical and it shows the signs of free charge carrier motion at low temperatures, what is controversial for mixed cations thin films.

The mobilities for the thin films were calculated from the maximum of the THz pulse in time domain as it is described in the **chapter 3 "Experimental Method and Data Analysis"**. *Figures 4.14 (d), 4.15 (d), 4.16 (c)* show the temperature dependency of mobility in thin films. The mobilities at room temperatures are quite similar for the thin films, yielding the highest mobility for $MAPbI_3$ and the lowest for $CsPbI_3$ as it is described in the section charge carrier transport at room temperature. However, at low temperatures, under 133K, the differences in mobility are more remarkable. The highest mobility of 280 $cm^2V^{-1}s^{-1}$ is observed for $MAPbI_3$ at 10 K while mobility values for the rest of thin films are significantly lower and constitute 100 $cm^2V^{-1}s^{-1}$ for $CsPbI_3$, 133 $cm^2V^{-1}s^{-1}$ for (Cs, FA, MA)Pb(I, Br)$_3$ and 100 $cm^2V^{-1}s^{-1}$ for (Cs, FA)PbI_3 at 10 K. The temperature dependent mobility for $CsPbI_3$ and triple cation (Cs,FA,MA)Pb(I,Br)$_3$ thin films shows clear reduction of mobility with temperature and thereby it has band-like charge carrier transport. However, the mobility in (Cs, FA)PbI_3 is not continuously increasing with decrease in temperature. First, the mobility increases up to 128 $cm^2V^{-1}s^{-1}$ at 30 K and then it reduces up to 100 $cm^2V^{-1}s^{-1}$ at 10 K. Such a decrease of mobility is not typical for band-like transport behavior (transport due to phonon scattering) and is likely

to result from scattering at impurities that are key scattering mechanism at low temperatures. The temperature mobility behavior is very similar for inorganic $CsPbI_3$ and triple cation thin film (Cs, FA, MA)Pb(I, Br)$_3$. *Table 4.7* summarizes the charge carrier mobility and fit parameters in various halide perovskites.

*Table 4.7. Parameters of modified Drude-Smith in thin films with **fixed** effective mass $m_{eff} = 0.2m_0$.*

Material	**T, K**	**τ, fs**	**c_1**	**μ_{DC}, cm^{2}V^{-1}s^{-1}**	**μ_t(time-domain), cm^{2}V^{-1}s^{-1}**	**t, fs**	**L , nm**
(Cs, FA)PbI$_3$	10	34.7	-0.72	83.9	101	85.8	2.4
	100	29.5	-0.77	60.8	72.2	67.7	5.9
	200	12	-0.64	37.6	39	46.9	5.8
	295	5.7	-0.52	24.3	25.4	31.4	4.7
(Cs, FA, MA)Pb(I, Br)$_3$	10	24.8	-0.69	67.4	132.9	163.3	4.5
	100	27.2	-0.77	54.3	73.9	86.7	7.5
	200	12.2	-0.63	39	42.9	57.7	7.1
	295	6.9	-0.6	24.5	25.6	34.4	5.1
CsPbI$_3$	10	10.8	$2\cdot10^{-18}$	95.3	105.2	52.5	7.9
	295	3.5	-0.28	21.9	22.2	31.4	4.7

As it was shown in the transport modeling section for $MAPbI_3$, the mobility at room temperatures is limited either by scattering at polar optical phonons or by polaron formation. Moreover, we have shown that polaron mobility may be defined by mobility on LO optical phonons with enhanced effective mass equal to polaron effective mass. Regardless of polaron or optical phonon scattering, both of mechanisms are fully described by the following quantities: charge carriers effective masses m, low – ε and high-frequency dielectric constants ε_∞ and LO optical phonon energy $\hbar\omega_{LO}$. The provided in literature values of electron and hole effective masses are in the range ~ 0.1 – 0.3m$_e$ for many perovskites[76–78,109,110]. The effective masses are defined from the curvature of conductance band minima (for electrons) or valence band maxima (for holes). It is known that the minima and maxima of band structure in halide perovskites are formed by metal-halide bonds[5]. Also reported values of low-frequency ε and high-frequency ε_∞ dielectric constants in $CsPbI_3$ and $MAPbI_3$ are quite similar: ε = 18 - 33[20,21,106] and ε_∞ = 4.5 – 6.5[20,21,106,109], revealing large aspect ratio between the dielectric constants. Furthermore, the LO optical phonons energies lay in the low THz frequency range and are also determined by bending and stretching modes associated with vibrations of metal-halide bonds[74,111]. Thus, the most important parameters that limit mobility at room temperatures

are determined by metal-halide network but not the cation compound in halide perovskites. Therefore, we obtain the mobilities for various compositions relatively similar and may conclude that the cation has a minor impact on mobility in halide perovskites at room temperature.

At temperatures below $T = \hbar\omega_{LO}/k$ = 133 K the population density of polar optical phonons is rapidly decreasing resulting in increase of mobility with temperature. At these temperatures the mobility for many semiconductors are normally influenced by charge-carrier-acoustic phonon interactions or by scattering at charged or neutral impurities. As we have already shown in the Modeling section for $MAPbI_3$ the mobility obtained for scattering at acoustic phonons at low temperatures is around 10^7 $cm^2V^{-1}s^{-1}$, what is 5 orders of magnitude higher than measured mobility for all thin films ~10^2 $cm^2V^{-1}s^{-1}$. The mobility of charge carriers, scattered at acoustic phonons, depends on elastic constant C= ρv_s^2, given as a product of material density ρ and squared sound speed v_s in the material of interest[28] ,as well as deformation potential E_1 as follows $\mu_{AD} \sim C/E_1^2$ for acoustic phonons of deformation potential, or piezoelectric coefficient p as $\mu_{AP} \sim C/p^2$ for acoustic phonons of piezoelectric potential. The deformation potential for holes and electrons for the most of semiconductors is in range of a few eV[23,64,94] and the elastic constants are 2.7 GPa[112] for $FAPbI_3$ and 7.3GPa[112] for $MAPbI_3$. Thus, one may conclude that a cation in metal halide perovskites do not have a large impact on elastic constants and deformation potential and, therefore, the mobility for thin films with various cation composition is expected to be similar to mobility at acoustic phonons, calculated for $MAPbI_3$.. Hence, if one excludes the scattering at acoustic phonons, the scattering at impurities is the only scattering mechanism that limits the mobility in MHPs at low temperatures. The conducted in this work simulation on scattering at impurities in $MAPbI_3$ showed, that the scattering at charged impurities seems not to explain completely the mobility values at low temperature mostly due to steep increase with temperature $T^{1.5}$. However, taking into account scattering at neutral impurities that have a mobility temperature dependency ~$(T^{0.5} - T^{-0.5})$ we obtained the mobility values that fit well to measured mobility at impurity concentrations ~10^{18} cm^{-3} for $MAPbI_3$ and this is in good agreement with measured donor concentrations in perovskites by Polyakov[102]. Thus, mobility in other perovskites are also likely limited by scattering at impurities.

Another important aspect that may limit the mobility at low temperatures is exciton formation. At low temperatures when the phonon population density is low, the free (mobile) charge carriers may get bound into an exciton state. The exciton formation results in reduction

of mobile charge carriers and thereby resulting in reduction of mobility. *Figure 4.17* shows the mobility for all thin films measured in this work and summarizes the calculation of mobility at LO optical phonons and impurities (a) and LO optical and acoustic phonons taking into account the exciton formation at low temperatures (b).

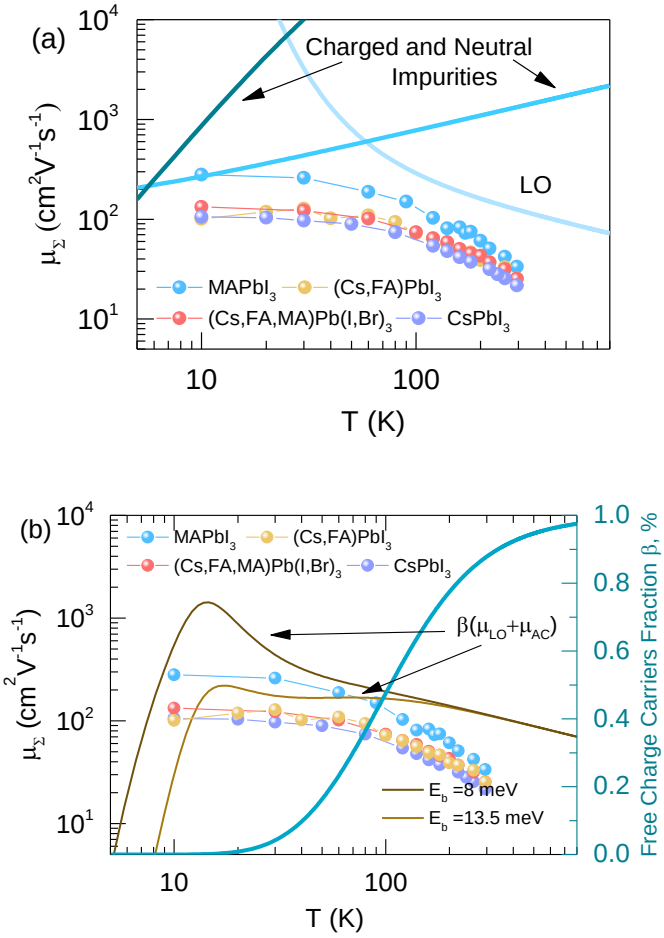

Figure 4. 17. The temperature dependent mobility for polycrystalline halide perovskite thin films and calculated mobilities at LO optical phonons and impurities (a) and LO optical and acoustic phonons taking into account the exciton formation (b).

4.8. Conclusions

The following polycrystalline metal halide perovskites thin films $MAPbI_3$, $(Cs,FA)PbI_3$, $(Cs,FA,MA)Pb(I,Br)_3$ and $CsPbI_3$ were investigated by THz spectroscopy. The thin films reveal very similar transport behavior, regardless of cation composition, and have the mobility in the range from 21.5 $cm^2V^{-1}s^{-1}$ for $CsPbI_3$ and 30 $cm^2V^{-1}s^{-1}$ for $MAPbI_3$. The room temperature mobility shows the signs of localization of charge carriers that may result from charge carriers-phonon coupling, the phenomenological parameter c_1, defined from the modified Drude-Smith fit, is in the range from -0.6 – -0.3. The recorded mobility spectra in the temperature range from

10 K to 295 K show the reduction of mobility with temperature, indicating thereby the band-like transport in MHPs. The detailed analysis of mobility from scattering at phonons and impurities show that the room temperature mobility is rather affected by scattering at optical phonons, while scattering at charged and neutral impurities are dominating in the low temperature range. Furthermore, it was shown that exciton formation may have a drastic impact on charge carrier mobility in MHPs at low temperatures.

5. Charge carrier transport in two-dimensional halide perovskites.

5.1. Introduction

Despite many outstanding optoelectronic properties of 3D halide perovskites and record power conversion efficiencies (PCE), that reached 25.1 % over the last 10 year of active research, a lack of stability is the main hurdle on the way to industrial application of 3D MHPs. To overcome this difficulty and improve stability, several approaches were proposed[113]. One of them is to implement large organic hydrophobic molecules such as phenethylammnium (PEA) and butylammonium (BA) into perovskite structure that result in formation of metal-halide octahedral layers separated by layers of organic bulky cations (PEA, BA). Such a structure is known as two-dimensional (2D) organic-inorganic hybrid perovskites. The layer of spacer cations is aimed to block the penetration of moisture into the halide perovskites layer and thereby it improves stability.

The general structure formula of 2D perovskites is $A'_2A''_{n-1}B_nX_{3n+1}$ where A' is a large spacer cation (PEA, BA and etc.), A'' is a cation (MA, FA, Cs), *B* is a metal cation (Pb, Sn) and *X* is a halide anion (Cl, I, Br), *n* specifies the number of perovskite octahedral $[BX_6]^{4-}$ sheets in perovskite layer, what is determined by composition of the solution precursor. Depending on the number *n*, one may distinguish between pure 2D (n=1), quasi-2D ($1 < n < 6$) and quasi-3D (n>6), 3D (n=∞) perovskites. The schematic structure of 2D perovskites for various values *n* is depicted in *figure 5.1*.

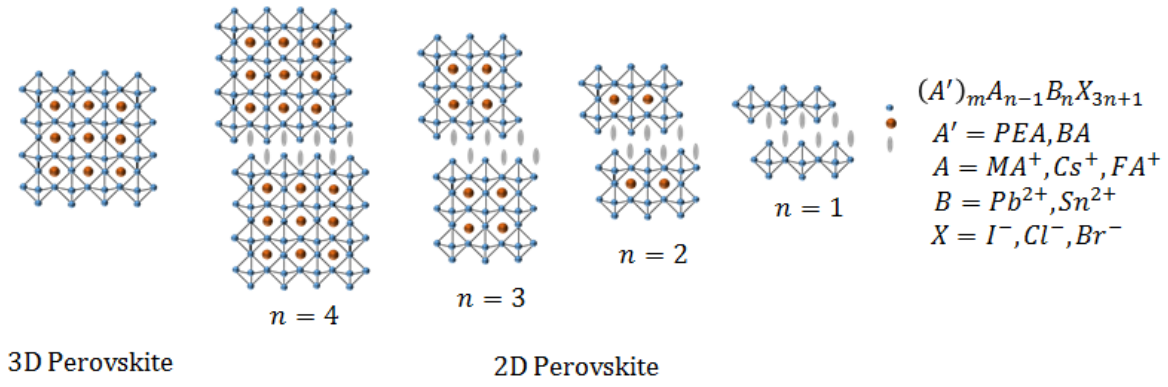

Figure 5.1. Schematic structure of 3D (n > 4), quasi-2D (n < 4) and 2D perovskites (n = 1)

.

In spite of the enhanced stability, the efficiency of 2D MHPs solar cells has increased from 4.73 % to 17.25 % for the last a few years[114–117]. However, the performance of the SCs based on 2D MHPs is still lower than 3D counterparts. The low PCE in 2D MHPs is attributed to poor

charge carrier transport, arising from dielectric and quantum confinement in the multilayered structures[32]. Another factor limiting the solar cells performance is larger band gaps in 2D perovskites[113,115].

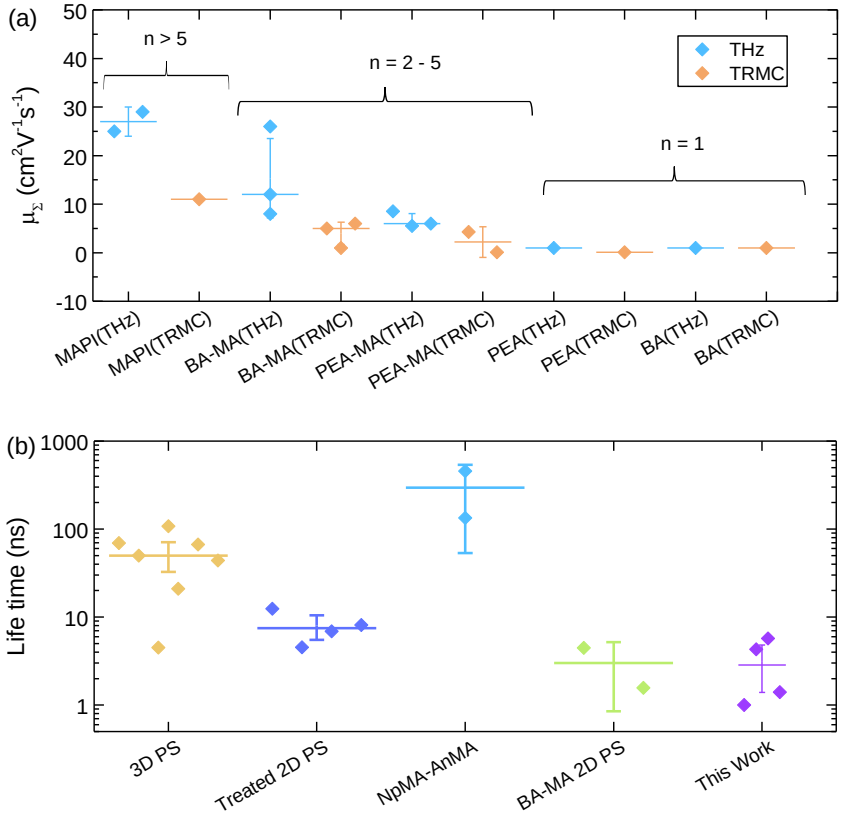

Figure 5.2. Comparison of mobility measured by TRMC or THz Spectroscopy (a) and life (decay) times obtained from TRPL measurements (b) provided in literature for various 2D hybrid perovskites.

The charge carrier mobility in 2D perovskites was previously studied by time resolved microwave spectroscopy (TRMC), optical pump THz probe spectroscopy (OPTP) and space charge limited current approach (SCLC). The mobility values vary in the range ~1 - 15 $cm^2V^{-1}s^{-1}$ (*figure 5.2 (a)*)[86,118–126,127,128] depending on measurement methods and number of metal-halide sheets *n* (perovskite layer thickness). Furthermore, a number of studies[120,121] have shown that mobility in 2D perovskites depends on the orientation of the layers: metal-halide layers show better conductivity than bulky cations layers and thereby the layers separation prohibits the charge carriers migration from one layer to another. Thus, in order to collect the generated charge carriers properly, vertical growth of layers (perpendicular to a substrate) is preferential for better solar cell performance. Hence, improvement of charge carrier transport was achieved so far with focus on 1) reducing the dielectric confinement by development of new spacer organic cations[117] or by modifying BA, PEA cations[129,130] or by mixing them with other materials[131]; 2) reducing the quantum confinement by reducing spacing between bulky

cations[121,132] or by increasing the *n* value (increasing 3D:2D ratio)[133,134]; or 3) the preferential (vertical) growth of layers by hot-casting tenchnique[135–139] or by using some extra additives[126,127,140,141] like NH_4SCN or MACl during thin film preparation.

Alongside with poor charge carrier transport, quantum and dielectric confinement in 2D perovskites lead to exciton formation with high binding energies of hundreds of meV[142,54,143]. At such high binding energies, the exciton is stable at room temperatures and should have an enormous impact on charge carrier dynamics in 2D perovskites. The behavior of excitons depends on the number of $[PbI_6]^{4-}$ sheets[118,119,142] and excitation densities[54]. Several studies[118,119] have shown that low concentrations (large *n*) of bulky organic cations results in reduction of monomolecular recombination rates due to passivation of traps at layer interfaces. However, the further increase in the content of spacer cations leads to increase in monomolecular, bimolecular and Auger recombination rates due to exciton recombination. In another work[142] two distinctive kinetic mechanisms of exciton (charge carriers) recombination were proposed, depending on the number of $[PbI_6]^{4-}$ layers *n*. According to this work[142], 2D perovskites with $n \leq 2$ the exciton decays via a non-radiative channel associated with trap states, resulting in shorter lifetimes, while for thin films with n>2 the dominating mechanisms is dissociation of exciton to long-lived free charge carriers that recombine via lower energy state by emission of photon, leading in turn to longer lifetimes. The lifetimes (decay times), estimated from different techniques, are in the range from a few ns to tens of ns (*figure 5.2 (b)*)[117,123,127,131,142,144], depending on number of $[PbI_6]^{4-}$ sheets *n*, treatment methods during thin films preparation or types of organic spacer cations. The largest lifetime is ~ 100 ns obtained for multiple aromatic ring ammoniums[117]. Furthermore, a number of authors proposed existence of polaronic excitons[145–147] and biexcitons[54] in 2D perovskites.

This chapter is dedicated to the investigation of charge carriers transport and dynamics in various 2D Ruddlesden – Popper perovskites polycrystalline thin films (RPP) $BA_2MA_{n-1}Pb_nI_{3n+1}$ (n = 2 - 4) by means of OPTP Spectroscopy. In this study, we perform a detailed analysis of charge carrier mobility spectra by the modified Drude-Smith model, explain the behavior of fit parameters and mobility depending on the number and orientation of octahedral sheets *n* in the thin films. Finally, we study the charge carrier dynamics and show its sensitivity to exciton formation in 2D perovskites with low number of $[PbI_6]^{4-}$ layers *n*.

5.2. Sample preparation

Four thin films $BA_2MA_{n-1}Pb_nI_{3n+1}$ (n = 2 - 4) were provided by Shanshan Zhan from the group of Prof. Neher at Potsdam University. Three samples $BA_2MA_{n-1}Pb_nI_{3n+1}$ (HC) (n = 2 - 4) were prepared by hot-casting technique and one sample $BA_2MA_{n-1}Pb_nI_{3n+1}$ (RT) (n = 4) was spin coated at room temperature. The thin films were deposited on quartz substrate. The detailed description of thin films preparation is given in Shanshan Zhan's paper[148]. The performed out-of-plane and in-plane X-ray Diffraction by Shanshan Zhan has shown the parallel and perpendicular orientation of the octahedral layers to substrate for $BA_2MAPb_2I_7$ (n = 2) and $BA_2MA_{n-1}Pb_nI_{3n+1}$ (n = 3 - 4), respectively[148].

5.3. Charge carrier mobility in two-dimensional perovskites

In order to investigate the charge carrier mobility, all four thin films were measured by OPTP Spectroscopy (The method and set-up is described in **chapter 3 "Experimental method and data analysis"**). *Figure 5.3 (a)* shows the mobility spectra for thin films, measured at 20 ps after photoexcitation, with modified Drude-Smith fit imposed above the spectra. The real parts of mobility show an increase with frequency while the imaginary parts gradually decreases and have negative values for all thin films. Such behavior of imaginary and real parts of THz mobility spectra indicate the presence of localized charge carriers in the thin films. Moreover, the mobility drops are observed at frequencies ~ 1 and 1.8 THz. These frequencies are the same as in the 3D counterparts and they are arising from coupling of charge carriers with metal-halide network vibrations. Besides that, the depth of these mobility drops decreases with decrease in the number of sheets in perovskites structure.

Due to the weak frequency dependency, thin film mobility values were determined from the time domain THz signal. As expected, the mobility decreases with decrease in the number of sheets n. The highest values of mobility, equal to 8 $cm^2V^{-1}s^{-1}$ and 5.9 $cm^2V^{-1}s^{-1}$, were obtained for $BA_2MA_3Pb_4I_{13}$ (HC) and $BA_2MA_3Pb_4I_{13}$ (RT) thin films, respectively. The higher mobility for the thin film, prepared by hot-casting technique, was expected as multiple works[136,137,139] have shown that this technique leads to improved power conversion efficiency due to improved alignment of the octahedral layers to the substrate and electrodes. This thin film with highest mobility has also shown the best PCE in the finished solar cell[148]. The lowest

mobilities 3.7 $cm^2V^{-1}s^{-1}$ and 5.1 $cm^2V^{-1}s^{-1}$ were obtained for double (n=2) and triple layered (n=3) 2D perovskites respectively. The obtained mobility values for thin films are in good agreement with THz mobility values obtained in some other works[86,118–120].

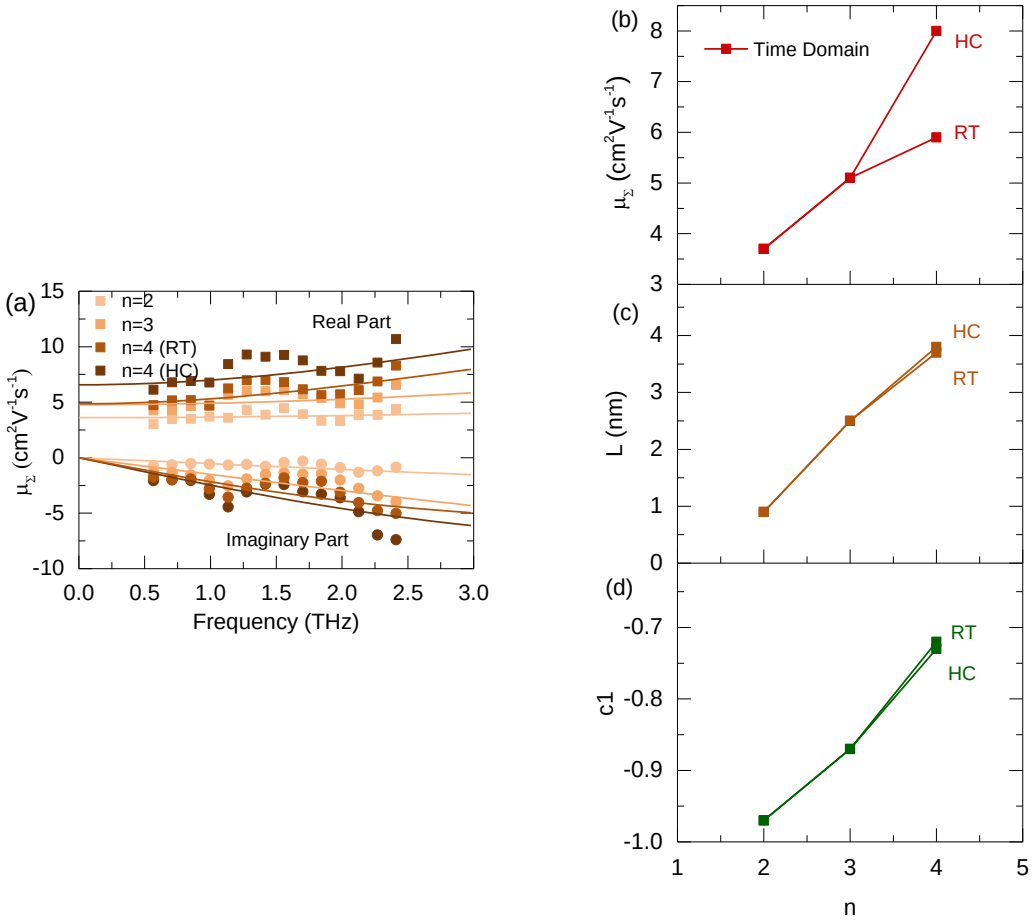

Figure 5.3. (a) Mobility spectra and modified Drude-Smith fit for BA2MA2Pb2I7, (b) time-domain mobility, (c) localization length from the fit and (d) parameter c1 depending on the number of layers.

Table 5.1. Parameters of applied modified Drude-Smith fit for measured 2D perovskites thin films.

Sample	**Scattering time τ, fs**	c_1	**DC mobility μ_{DC}, $cm^2V^{-1}s^{-1}$**	**Time domain μ_t, $cm^2V^{-1}s^{-1}$**	**Localization length L, nm**
$BA_2MA_3Pb_4I_{13}$ *(RT, n =4)*	1	-0.72	4.9	5.9	3.7
$BA_2MA_3Pb_4I_{13}$ *(HC, n = 4)*	1.4	-0.73	6.6	8	3.8
$BA_2MA_2Pb_3I_{10}$ *(n = 3)*	2.1	-0.87	4.8	5.1	2.5
$BA_2MAPb_2I_7$ *(n = 2)*	6	-0.97	3.7	3.7	0.91

In order to give more quantitative insight into the transport properties, the modified Drude-Smith model was applied to all measured thin films spectra. The fit (modeling) was performed

by varying the scattering time τ, parameter c_1, localization length L and diffusion time $t_\circ$, while the effective mass m for charge carriers was set to average value available in literature $0.1m_0$[149], assumed equal to both electrons and holes due to similarity of effective masses in 2D

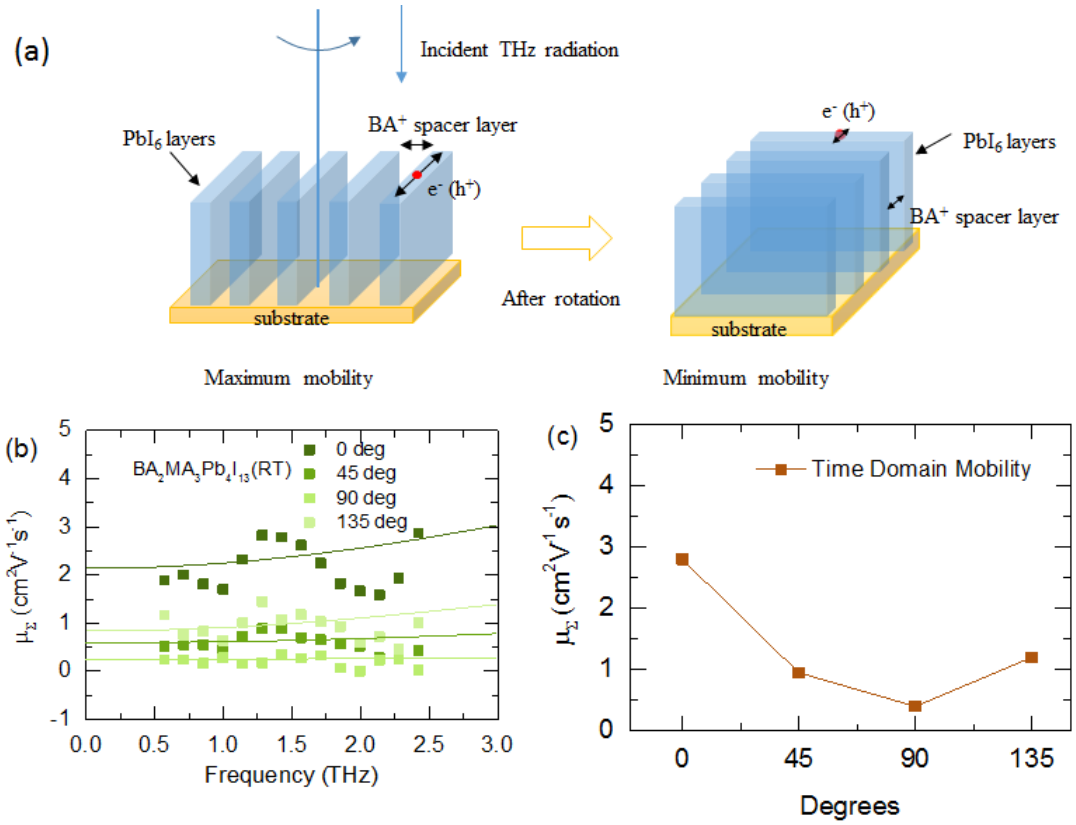

Figure 5.4.(a)The scheme, explaining the dependency of mobility on layers orientation: electron (hole) acceleration by THz field, polarized parallel to the conductive PbI_6 layers (left) and localization of electron (hole) when the polarization plane of THz field is perpendicular to orientation of the layers (right); (b) The mobility spectra and modified Drude-Smith fit; (c) time-domain mobility depending on layers orientation for BA2MA3PbI12 (RT).

perovskites, calculated by DFT in the various works. The modeling also shows the decrease of localization length L and c_1 with decrease in the number of metal-halide sheets n (*Figure 5.3 c, d*), indicating thereby the charge carrier localization in very thin meta-halide layers with low n value. Beside the difference in mobility in $BA_2MA_3Pb_4I_{13}$ (HC) and $BA_2MA_3Pb_4I_{13}$ (RT) thin films, there is not much difference in localization length L and c_1 for both thin films. The relaxation time is in the range 1-6 fs for measured thin films (*table 5.1*) and thereby comparable to the ones in 3D counterparts. The localization length L is in good agreement with thicknesses of metal-halide $[PbI_6]^{4-}$layers. A typical thickness for a single $[PbI_6]^{4-}$sheet layer (n=1) is ~0.6 nm[150], indicating rather the charge carrier localization scale is within a perovskite layer.

The reduction of mobility with decrease in *n* may be easily understood by the increasing strength of quantum confinement of photogenerated charge carriers within layers (quantum wells). Another aspect limiting the mobility in multilayered structures is exciton formation due to dielectric confinement, which arises from periodic change in permittivity of the layers (the dielectric constants for spacer layers $\varepsilon \sim 2$ and for PbI_6 octahedral layers $\varepsilon \sim 5$)[118].

In order to investigate in-plane and out-of-plane charge carrier mobility, we performed OPTP measurements after rotating the sample to angles of 0°, 45°, 90° and 135°. For this measurement we used a $BA_2MA_3Pb_4I_{13}$ (RT) thin film, where the layers were oriented perpendicular to the substrate according to XRD measurements, performed by Zhang[148]. By rotating the thin film the mobility is expected to change, reaching its maximum, when the polarization plane of THz filed is parallel to metal-halide layers, and reaching its minimum, when the polarization plane is perpendicular to the layers (*figure 5.4 (a)*).

Figure 5.4 (b) shows the mobility spectra at various angles for the $BA_2MA_3Pb_4I_{13}$ (RT) thin film and *figure 5.4 (c)* shows the time domain mobility depending on the measurement angles. As shown in the graph, the time domain mobility of 2.8 $cm^2V^{-1}s^{-1}$ is at its maximum at 0°, then it gradually decreases to its minimum value 0.4 $cm^2V^{-1}s^{-1}$ at 90° and starts increasing again. The similar effect of dependency of mobility on the layers orientation was also observed in some other 2D MHPs thin films[120,121], measured by TRMC and in another measurement configuration by tilting the thin film with regard to the THz beam polarization plane. Since the performance of the SCs strongly depends on the charge carrier mobility, this effect may have a drastic impact on the SCs performance. Therefore, the vertical (perpendicular) orientation of the conductive $[PbI_6]^{4-}$layers with regard to selective contacts is preferential in order to guarantee the most efficient collection of charge carriers.

5.4. Charge carrier dynamics

In order to study charge carrier dynamics in two-dimensional perovskites, we measured the photoconductivity transients (decay of photoinduced change in THz pulse transmission $\Delta T/T$) of the thin films by OPTP Spectroscopy at the maximum of THz pulse with pump beam fluence 21.1 μJcm^{-2}. Since the photoconductivity is a product of mobility μ and excess charge carrier density ΔN (photogenerated charge carrier density), it is assumed that mobility does not change

significantly with time after photoexcitation and the decay of $\Delta T/T$ (literally photoconductivity) occurs due to the kinetics of excess charge carriers $\Delta N(t)$.

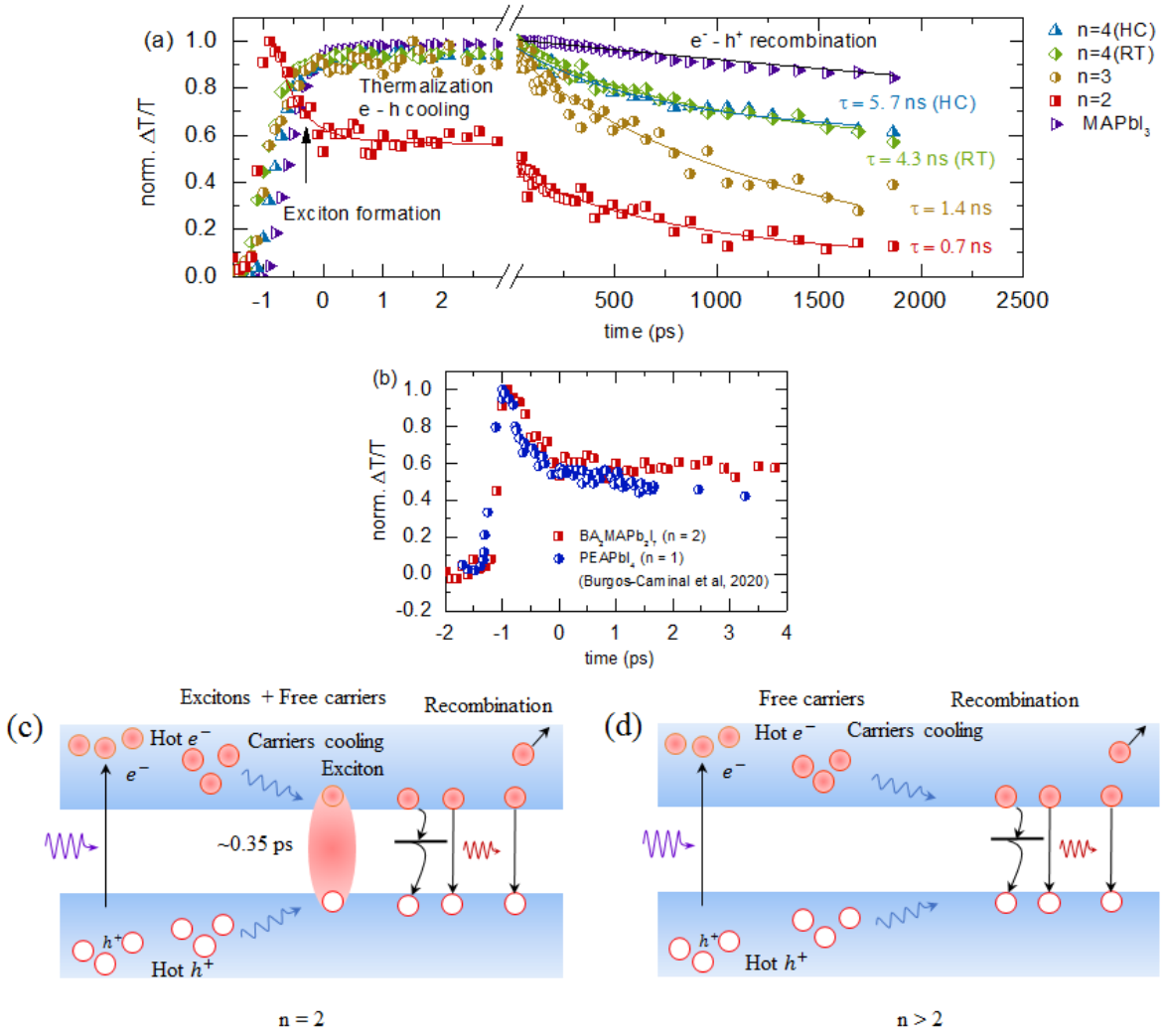

Figure 5.5. The photoconductivity decay ΔT/T form THz measurements for thin films (a); comparison of photoconductivity decay ΔT/T in $BA_2MAPb_2I_7$ (n = 2) in thin work with transient for $PEAPbI_4$ in the work Burgos-Caminal et al., 2017. Indicating the exciton formation in two-dimensional perovskites(b); The scheme of charge carrier kinetics (dynamics) in 2D perovskites n =2(c) and n = 3-4 (d).

F*igure 5.5 (a)* shows the recorded transients for two-dimensional perovskites thin films compared to $MAPbI_3$ thin films (3D perovskite). In order to clearly see the dynamics directly after photoexcitation of charge carriers, the plot is split into two subplots in the timeframes first from -1 to 3ps and then from 20 ps to 1860 ps. The $BA_2MA_{n-1}Pb_nI_{3n+1}$ (n = 3-4) and $MAPbI_3$

thin films show very identical behavior in the first ps of rise of $\Delta T/T$ and then shows the plateau up to 100 ps for $MAPbI_3$ and up to ~ 50 ps for the two-dimensional perovskites thin films (n = 3, 4). The plateau ($\Delta T/T$ remain constant) up to tens of ps may be attributed to cooling of charge carriers in halide perovskites due to hot phonon bottleneck effect at high fluences, that was already observed in some other works[87,151]. According to bottleneck effect, the charge carriers emit and reabsorb LO optical phonons, what in turn results in increase of effective cooling time – time needed for charge carriers to reach the band edges. After that $\Delta T/T$ decays can be explained by charge carrier recombination.

Interestingly, the $BA_2MAPb_2I_7$ ($n = 2$) shows a different dynamics than the other thin films. After photoexcitation, $\Delta T/T$ shows a drastic decrease. As the OPTP is sensitive to free charge carrier density $\Delta N(t)$, the decrease of transmission $\Delta T/T$ is likely to be due to that electrons and holes form the excitons. Moreover, identical behavior in two-dimensional perovskites was also shown in the work Burgos-Caminal et al.[54](*Figure 5.5 (b))* who studied the charge carrier dynamics in $PEAPbI_4$ (n = 1) by time-resolved THz Spectroscopy (TRTS, OPTP) and fluorescence upconversion spectroscopy (FLUPS). By comparing the results from TRTS and FLUPS, they concluded the exciton formation occurs within 350 fs after photoexcitation. By performing a three exponential fit, we have found the following first decay time 390 fs, which can be interpreted as the timeframe of exciton formation.

The decay time of the transients may be estimated by performing the multi-exponential fit $y = y_0 + A \cdot \exp[-(t - t_0)/\tau_1] + B \cdot \exp[-(t - t_0)/\tau_2] + C \cdot \exp[-(t - t_0)/\tau_3]$and the total decay time is defined as $\tau = (A\tau_1 + B\tau_2 + C\tau_3)/(A + B + C)$. From the fit the following total decay times for the thin films are obtained: 5.7, 4.3 ns for $BA_2MA_3Pb_4I_{13}$ (n = 4, HC, RT) respectively, 1.4 ns for $BA_2MA_2Pb_3I_{10}$ (n = 3) and 0.7 ns for $BA_2MAPb_2I_7$ (n = 2). The defined decay times cannot be directly regarded as lifetimes of charge carriers, but we still may give some assumptions why they are different and decrease with n. Despite a bit different decay times for n = 4 thin films obtained from the exponential decay fit, both of them show similar behavior and the transients overlap in the ns time range. Thus, the preparation technique has a minor effect on charge carrier dynamics. However, the transients decay faster than the transient for $MAPbI_3$. Due to low trap densities in $MAPbI_3$ and passivation effect of the interface layers by organic spacer cations in two-dimensional perovskites, the faster decay of transients is likely to be owing to enhanced Auger recombination or radiative recombination, enhanced because of quantum confinement in 2D perovskites. With increase in content of organic spacer cations and decrease in thickness of the octahedral layers (lower n), the excitonic effects are becoming

stronger. According to the work (Blancon et al., 2017)[142], in low dimensional perovskites at n <2, the strong excitonic interactions between electrons and holes, result in recombination via traps and thereby result in shorter lifetimes.

On the base of photoconductivity transients, described above, the following charge carrier dynamics may be proposed in two-dimensional perovskites (see *figure 5.5 (c,d)*). The analysis of transients indicates that charge carrier dynamics in 2D perovskites is dependent on the number of sheets *n*. For *n* = 3-4, where the layers are thicker, we observe the charge carrier dynamics similar to the 3D counterparts: The slow cooling is observed within ~100 ps for MAPI and slightly shorter ~ 50 ps for two-dimensional perovskites *n*=3-4. After cooling and reaching the band edges the charge carriers are likely to undergo the radiative recombination or Auger recombination. For *n* =2, where quantum and dielectric confinement are stronger, charge carriers form very fast the excitonic state within 390 fs after photoexcitation. The reduction of decay time, compared to 3D $MAPbI_3$, is highly likely to be due to the confinement of the charge carriers within $[PbI_6]^{4-}$ layers that may increase the rate of radiative or Auger recombination.

5.5. Conclusions

The two-dimensional MHPs thin films with various number of octahedral $[PbI_6]^{4-}$ sheets (*n* = 2-4) were measured by THz Spectroscopy. The measured mobility is in the range from 3.7 $cm^2V^{-1}s^{-1}$ for *n* =2 and 8 $cm^2V^{-1}s^{-1}$ for *n* = 4, prepared by hot-casting technique. Charge carrier mobility decreases with decrease in number of $[PbI_6]^{4-}$ sheets *n*. This reduction of mobility can be explained by localization of charge carriers within these layers. The localization length *L*, determined from the modified Drude-Smith fit, is in the range from 0.9 nm to 3.7 nm, what is in good agreement with the thickness of metal-halide layers. Furthermore, poor transport properties are observed across the layers of separation molecules, which results in preferential charge carrier transport within $[PbI_6]^{4-}$ layers. We directly observed these preferential transports by sample rotation and could confirm vertical orientation of the conductive $[PbI_6]^{4-}$layers in $BA_2MA_3Pb_4I_{13}$ thin film. Moreover, the kinetics and lifetimes are strongly influenced by exciton formation for the thin film with *n*=2.

6. Charge carrier transport in nanocrystalline perovskites

6.1. Introduction

Alongside with three- and two-dimensional perovskites, the colloidal 0-dimensional perovskites (quantum dots (QDs), nanocrystals (NCs)) have recently attracted much attention due to their low cost production, relatively low V_{OC} losses, high PL quantum yield (PLQY), high defect tolerance, efficient multiple exciton generation and the potential to suppress the Shockley-Queisser limit by collecting hot charge carriers before they cooled down to the band edges[152,153,154]. However, in spite of all advantages, the power conversion efficiency (PCE) is still limited and is far from the PCE for their 3D counterparts, with its maximum so far value 17.4 %[155]. The reason for relatively low PCE is poor charge carrier transport due to bad NCs coupling (large spacing between NCs). The measured mobility values in perovskites NCs are in the range of 0.01 - 2 $cm^2V^{-1}s^{-1}$ [156–160]as shown in *figure 6.1*, except the high values of mobility 2500 - 4500 $cm^2V^{-1}s^{-1}$ for $CsPbBr_3$ QDs in the works (Yettapu et al., 2015)[160] and (Sarkar et al., 2016)[159] (both from Mandal et al. group) and low values of mobility $2.6 \cdot 10^{-6}$ $cm^2V^{-1}s^{-1}$, determined from SCLC method by (Liu et al., 2020)[158]. The mobility varies depending on the measuring methods and composition of perovskite, but is lower than in 3D and 2D counterparts for the most cases.

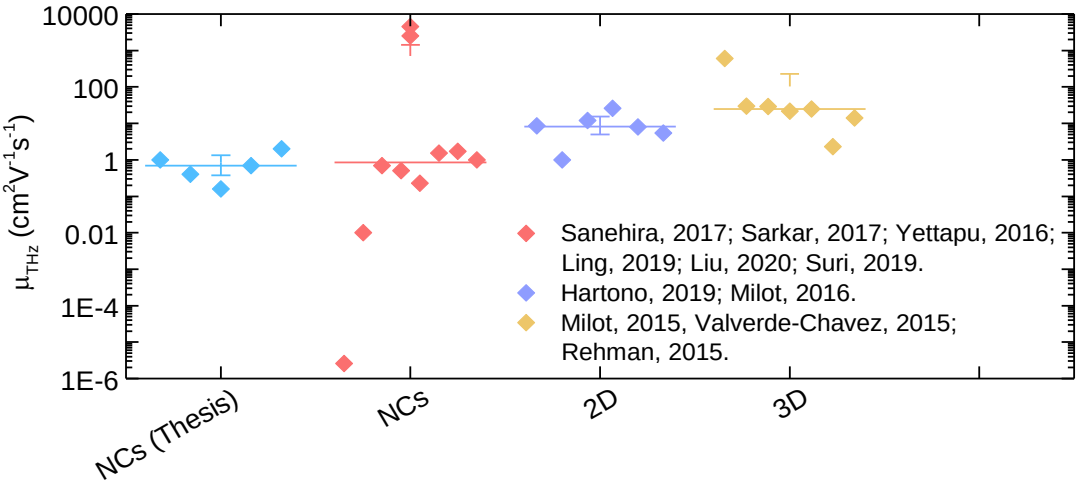

Figure 6.1. Comparison of mobility measured by various techniques in the perovskites of various dimensions.

The most of the perovskites NCs thin films are produced according to ligand-assisted methods at room temperature for organic-inorganic PNCs, described by (Schmidt et al., 2014)[161] and (Zhang et al.,2015)[162] and hot-injection method for all-inorganic perovskites NCs,

introduced by (Protesescu et al, 2015)[163]. Unlike conventional II-IV NCs, the octylamine or oleylamine (OLA) and oleic (OA) acids are the main surface ligands, used in the thin film preparation. OLA controls the kinetics of crystallization and thereby influences the size of colloidal NCs, while the OA suppresses the NCs aggregation and influences the colloidal stability[162]. However, these ligands are relatively long and thereby they limit the charge carrier transport in perovskites NCs by creating the barriers between the NCs.. *Figure 6.2* shows the difference in mobility in the THz range for $CsPbI_3$ polycrystalline and nanocrystalline thin films.

In order to improve the charge carriers coupling in the PNCs, the main studies on ligands engineering is being conducted in the following directions: (1) by removing the ligands and replacing them with shorter ones[157,164,165]; (2) by controlling the amount of the ligands during the synthesis[158,166,167]; (3)partial replacement of OLA/OA with other ones such as octanoic/octylamine ligands[168].

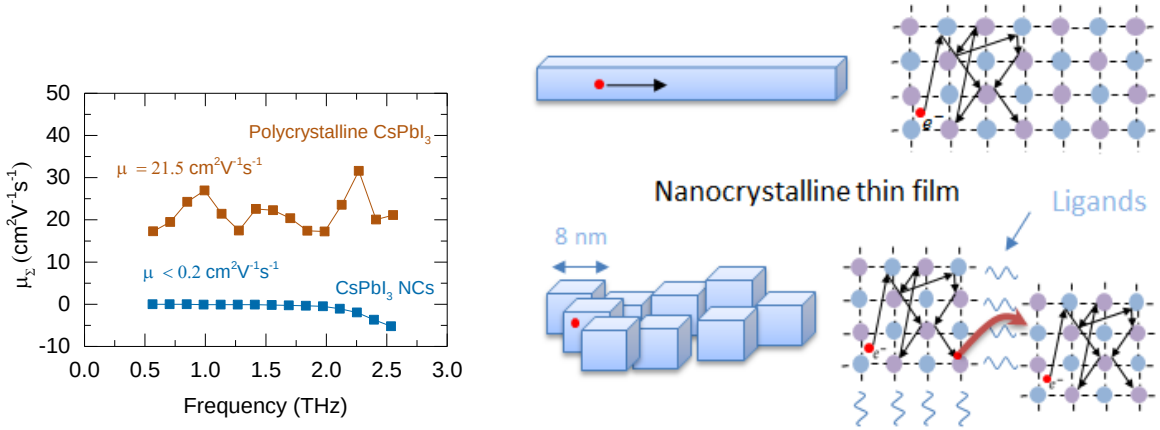

Figure 6.2. The real parts of mobility spectra in $CsPbI_3$ poly- and nanoncrystalline thin films (left) and schematic explanation of limitation of the mobility in nanocrystalline materials by introducing the barriers between the NCs from the ligands (right).

The nm-size of the crystals implies that the photoexcited charge carriers may become confined or localized within nanocrystals, resulting in change of optoelectronic properties of the materials such as increasing the bandgaps. Furthermore, similar to 2D perovskites , the quantum confinement of the photoexcited charge carriers may trap them into a bound excitonic states. The studies on steady-state PL have shown that exciton binding energies in perovskites NCs vary in the range 20-75 meV[169,170], what is in general higher than room temperature energies *kT* and therefore it makes the exciton stable even at room temperature in perovskites NCs. The presence of excitons and high defect tolerance in the perovskites NCs results in very high PLQY (around 90 %)[163]. A number of studies showed the formation of excitons, biexcitons

in the ps range[154,171,172,173]. Moreover, the confinement of charge carriers leads to enhancement of Auger/radiative recombination at high fluences and thereby limiting the lifetimes. The characteristic lifetimes are in the range of 1-100 ns[156,158,164,166,168,171,174–176], with the highest values for organic-inorganic perovskites NCs.

The ligands play an important role in stabilization and kinetics of the NCs and at the same time worsening the coupling between them. Therefore, in this chapter we investigate how various ligands treatments such as washing, annealing and replacement with shorter ones influences the charge carrier mobility and dynamics in perovskites $CsPbI_3$ NCs.

6.2. Sample preparation

Nanocrystalline $CsPbI_3$ thin films were prepared by Martin Kaergel in the group of Dr. Unold at Helmholtz Zentrum Berlin according to hot-injection method described in details by Protesescu et al.[163]. Instead of oleylamine acid (OLA), the dioctylamine acid was used as a surface ligand. Different treatment were carried out with thin films in order to investigate their impact on charge carrier transport: removal of the ligands from the surface of NCs by immersing into the solution of methyl acetat MeOAc; by annealing at 200 °C for 1 minute; or by replacement and coating with FA (formamidinium) and FA+Pb (formamidinium + lead) as described by Sanehira et al.[164].

Thus, we probed four different $CsPbI_3$ nanocrystalline thin films with different ligands treatment: $CsPbI_3$ NCs with washed ligands away by MeOAc, $CsPbI_3$ NCs annealed at 200 °C, $CsPbI_3$ NCs coated by FA and FA with Pb. The average size of nanocrystals is in the range of 8-20 nm. Further in this chapter the charge carrier transport properties in nanocrystalline thin films are compared with polycrystalline $CsPbI_3$ thin film, prepared by Pascal Becker in the group of Dr. Unold, which transport properties were described in **chapter 4** 3D perovskites.

6.3. Charge carrier mobility in NCs perovskites

In order to study charge carrier mobility, all treated thin films were measured by OPTP Spectroscopy (The technique is described in detail in the **chapter 3 "Experimental Method and Data Analysis")**. *Figures 6.3 – 6.5* show the THz mobility spectra for the thin films.

The removal of the ligands was done by immersing the thin film into a bath with MeOAc. *Figure 6.3 (a)* shows the mobility spectrum for the thin film with washed (removed) ligands. As seen from the graph, both real and imaginary parts of mobility spectrum are very close to 0

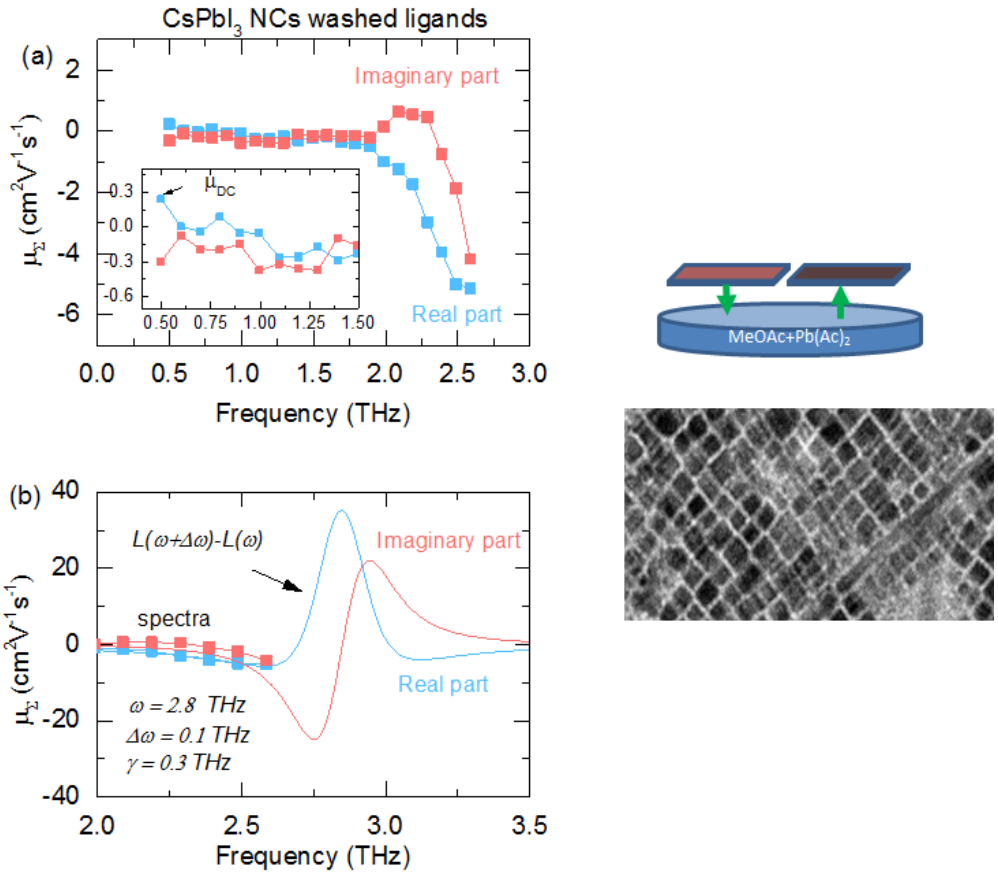

Figure 6.3. The real and imaginary parts of mobility spectra for $CsPBI_3$ NCs with removed ligands in the solution of methyl acetat MeOAc. The SEM images were provided by Martin Kaergel.

$cm^2V^{-1}s^{-1}$ in the frequency range from 0.5 to 2 THz. From 2 THz real part of mobility shows a drastic drop of mobility while the imaginary part first slightly increases and sharply drops afterwards too. The behavior of mobility spectrum rather indicates the resonance character, arising from some phonon excitation by THz pulse. If the real and imaginary parts had an inverse tendency (i.e. if it had the positive sign), then the resonance could be regarded as a Lorentzian response of charge carriers, indicating the total localization of charge carrier. However, if we assume the resonance undergoes the frequency shift $\Delta\omega$ due to heating by pump pulse and take into account that we measure the difference in THz pulse transmission $\mu \sim \Delta T/T$, then the negative sign of real and imaginary parts may come from the difference of two Lorentzian curves shifted by frequency $\Delta\omega$ $\mu \sim L(\omega + \Delta\omega) - L(\omega)$. By performing the modeling of two shifted Lorentzian curves for $\Delta\omega$, it was found the resonance frequency ω =

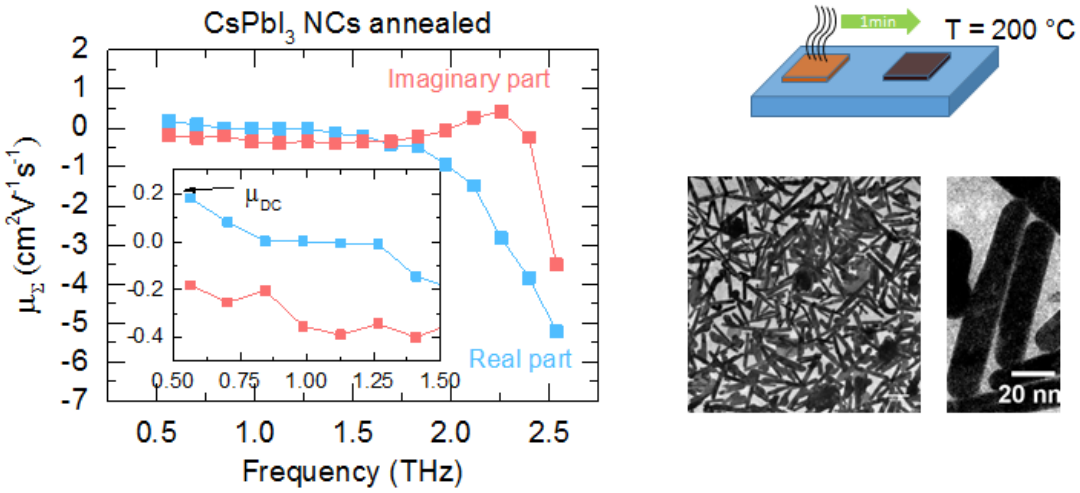

Figure 6.4. The real and imaginary parts of mobility spectra for $CsPBI_3$ NCs annealed at 200 °C. The SEM image were provided by Martin Kaergel.

2.8 THz with frequency shift $\Delta\omega = 0.1$ THz fit well to experimental spectra (*figure 6.3 b*). Since the resonance dominates in all measurement frequency range, it is tough to assign the DC value of mobility. However, according to the insets in the *figure 6.3*, we may conclude that mobility is lower than 1 $cm^2V^{-1}s^{-1}$. The low mobility in washed thin films may come from reduced colloidal stability resulted from partial removal of the ligands especially OA that is responsible for stability of the nanocrystals.

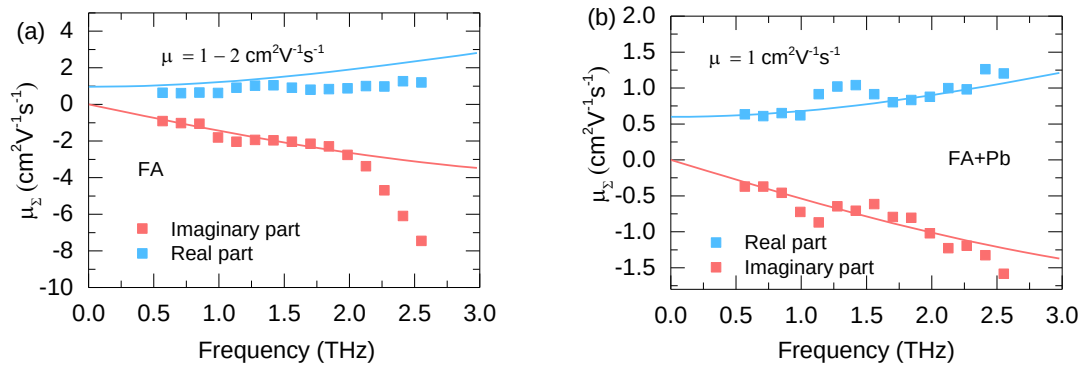

Figure 6.5. The real and imaginary parts of the mobility spectra for $CsPbI_3$ NCs coated by FA and by FA with Pb after ligands removal.

In *figure 6.4* the mobility spectrum for thin film that after the removal of ligands was also annealed at 200 °C. As see from the graph, the spectrum shows similar mobility behavior with clear domination of resonance at 2.8 THz. The DC mobility is also lower than 1 $cm^2V^{-1}s^{-1}$.

A further attempt to improve the electron coupling was done by coating the nanocrystals with FA (formamidinium) and FA with Pb (formamidinium with lead) after removal of the ligands in methyl acetat MeOAc as it is described in the work (Sanehira et a., 2017)[164]. *Figure 6.5* shows the mobility spectra for the thin films. As it is seen from the figures, the mobility spectra are not so strongly dominated by resonance. The real part of mobility decreases in the low THz range and the imaginary part is negative, indicating the localization of charge carriers. The mobility spectrum for the thin film coated by FA reveals higher mobility and show the phonon features coming from electron-phonon coupling at frequencies 1 and 1.8 THz, resulting from excitation of PbI_6 vibrations by THz field. This coupling may indicate that a perovskite phase forms between the NCs thus improving the transport properties. The applied modified Drude-Smith fit yields the following mobility values 1.5 and 1 $cm^2V^{-1}s^{-1}$ for FA and FA w/ Pb, respectively. And for FA spectra we may observe the phonon resonance at 2.5 THz similar to washed and annealed NCs but much suppressed (weaker).

6.4. Charge carrier dynamics in NCs perovskites

In order to investigate the charge carrier dynamics in the thin films, the photoconductivity transients were measured by OPTP technique. The decay times were estimated by performing the triple exponential fit $y = y_0 + A_1 \cdot \exp[-(t - t_0)/\tau_1] + A_2 \cdot \exp[-(t - t_0)/\tau_2] + A_3 \cdot \exp[-(t - t_0)/\tau_3]$ with estimation of average decay time as follows $\tau_{avg} = \sum_{i=1}^{3} A_i\tau_i \,/\, \sum_{i=1}^{3} A_i$. *Figure 6.6* shows the normalized THz transients $\Delta T/T$ for all thin films.

The longest decay time 6.9 ns was obtained for FA-coated $CsPbI_3$ NCs while interestingly the thin films coated with FA and Pb show the fastest decay around 0.7 ns. The polycrystalline and nanocrystalline $CsPbI_3$ show quite similar decay times 3.3 and 2.7 ns, respectively. Since the mobility spectra were overload from the resonance, arising likely from the heating of the sample by optical pump, it is not completely clear if the THz transients indicate the decay due to recombination processes or due to phonon effect. Since the mobility spectra from thin films with NCs coated with FA and FAw/Pb are not explicitly affected by phonon resonance, we assume that the decay time is defined by trapping-assisted recombination. The longest decay time for FA-coated $CsPbI_3$ may reveal the largest total decay times that are likely to be due to passivation effect of the traps by coating with FA atoms. The possible reason for short decay times for FA/Pb-coated is probably due to formation of multiple phases of $FAPbI_3$ and $CsPbI_3$ with recombination active phase boundaries, due to excess of lead Pb that may results in high

trap densities at the grain boundaries. The assignment of the decay times for the rest of the thin films is ambiguous due to the strong effect of the phonon resonance in the mobility spectra.

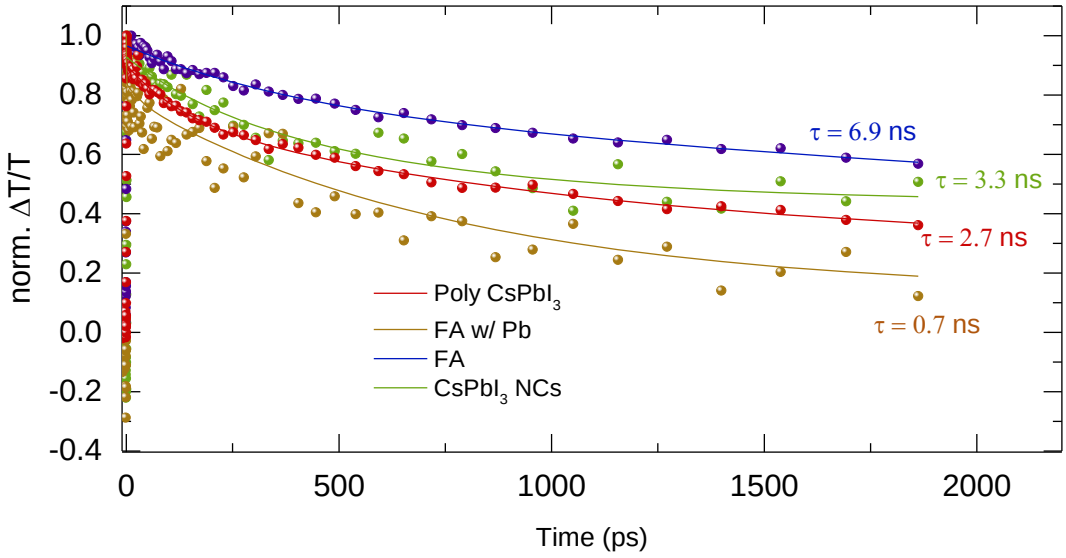

Figure 6.6. The photoconductivity transients for variously treated $CsPbI_3$ NCs with indicated decay times.

6.5. Conclusions

The nanocrystalline $CsPbI_3$ thin films were studied by THz spectroscopy. The thin films were treated by various processes and the impact of post-treatments on charge carrier mobility was investigated. The thin films with removed ligands and annealed afterwards show very similar mobility behavior, dominated by the resonance feature, as assumed, due to the heating by optical pump pulse. The mobility is less than 1 $cm^2V^{-1}s^{-1}$ for both thin films. The $CsPbI_3$ NCs, coated by FA and FAw/Pb, show the highest mobility in the rnage from 1-2 $cm^2V^{-1}s^{-1}$. Also, the mobility spectra look rather the mobility spectra for their 3D counterparts, revealing the phonon excitation at 1 and 1.8 THz and with signs of charge carrier localization. The increased mobility for the coated thin films can be attributed to enhanced coupling between the perovskites NCs.

7. Conclusions and Outlook

This thesis is dedicated to the investigation of charge carrier transport and dynamics in various metal-halide perovskites. The charge carrier mobility was measured by THz Spectroscopy (OPTP) at temperatures between 10-300K and the spectra were modeled by various models, including the Drude, truncated and modified Drude-Smith models. The charge carrier transport in three-dimensional metal-halide perovskites was also quantitatively analyzed in a broad range of temperatures with respect to the scattering of charge carriers at phonons and impurities within the linear transport and relaxation time approximations. The charge carrier dynamics was studied in low-dimensional halide perovskites by THz spectroscopy and the decays of the THz transients were analyzed by multi-exponential decay curves.

The polycrystalline three-dimensional metal-halide solution processed thin films $MAPbI_3$, $(Cs,FA)PbI_3$ and $(Cs,FA, MA)Pb(I,Br)_3$ were provided by Dr. M. Stolterfoht from Potsdam University and the polycrystalline $CsPbI_3$ thin film, prepared by evaporation, was provided by Dr. P. Becker from Helmholtz Zentrum Berlin.

The thin films reveal moderate mobilities with the highest mobility value (33.5 ± 3.0) $cm^2V^{-1}s^{-1}$ for $MAPbI_3$ and the minimum value (21.5 ± 2.2) $cm^2V^{-1}s^{-1}$ for $CsPbI_3$ at room temperatures. The phenomenological parameter c_1, determined from the modified Drude-Smith modelling, varies from -0.3 to -0.6, depending on the thin film. The negative values of the parameter c_1 along with negative imaginary part of mobility spectra indicate the presence of localization of charge carriers in the thin films. The scattering times in the metal halide perovskites are also very short and do not exceed 10 fs for any of the samples. These short scattering times can be regarded as one of the origins of moderate mobilities in metal-halide perovskites.

The mobility tends to increase with decrease of temperature. This trend indicates band-like transport in three-dimensional perovskites, i.e. the mobility should be limited by scattering at phonons at higher temperatures. The mobility at low temperatures in turn stays relatively constant and reaches a plateau. Moreover, the phase transition in $MAPbI_3$ at around 160 K does not impact the mobility significantly.

The analysis of charge carrier mobility, conducted in this work, taking into account the scattering at various phonons and impurities, has shown that the scattering at polar optical phonons likely limits the mobility in metal-halide perovskites at room temperatures. To the best of our knowledge, for the first time, the mobility related to polar optical phonon scattering was

calculated by regarding the polaron effective mass and is compared to previous works on polaron mobilities in halide perovskites. The obtained electron and hole mobility, scattered at polar optical phonons with polaron effective mass, is equal to 184 $cm^2V^{-1}s^{-1}$ and is lower than the polaron mobility 240 $cm^2V^{-1}s^{-1}$ (sum of electron and hole mobility), calculated by the Hellwarth formula[20]. However, regardless of the applied models, the retrieved mobilities are much larger than the ones obtained from the experiments. The inclusion of dynamic disorder, of the Rashba effect or of dielectric drag have only partially lowered the modeled mobilities towards the experimental results. Additional, uncertainty or discrepancies in determination of input parameters, used in mobility calculation may contribute. Since the effective mass for electrons and holes varies in the range from $0.1 – 0.3m_e$[76–78] in the literature, the choice of the largest available effective mass moves the predicted polar optical mobility toward the experimental results. The polaronic drag further increases the effective masses of electrons and holes by ~+25%.Therefore, more accurate determination of the effective mass of charge carriers is still required. Moreover, alongside with effective mass of charge carriers, the static and high-frequency dielectric constants as well as polar optical phonons energy have also an impact on charge carrier mobility in metal-halide perovskites . As shown in this thesis, the similarity between the polaron and polar optical phonons mobility with polaron effective mass indicates that charge carrier mobility at room temperatures can be explained by both scattering at polar optical phonons and polaron formation. Therefore, it makes it hard to distinguish between scattering at polar optical phonon or polaron formation in metal-halide perovskites, based only on mobility values.

The low temperature mobility reaches a plateau at around 80 K and stays relatively constant for most of the thin films except for a little reduction of mobility in (Cs,FA)PbI_3 at 30 K. Such a behavior of mobility may be explained by scattering at impurities that often limit the mobility in semiconductors at low temperatures. The detailed analysis of charge carrier scattering at charged impurities shows that scattering at charged impurities is not sufficient to explain the mobility behavior. For the first time, in this work the scattering at neutral impurities was considered for lead-halide perovskites. The gentle increase of mobility with temperature for neutral impurity scattering together with charged impurity scattering describe the measured mobilities at low temperatures for impurity concentrations $N = 10^{17} – 10^{18}$ cm^{-3}. Alongside with impurities, this thesis shows the importance of considering exciton formation at low temperatures. The scattering at acoustic phonons can be neglected since the mobility both at room and at low temperatures is much higher than the ones obtained from experiment.

The detailed analysis of mobility in metal-halide perovskites shows that the cation has a minor impact on charge carrier mobility. The temperature behavior is very similar to all thin films regardless of cation composition. At room temperature the mobility values are very close to each other and ranging from 21.5 to 30 $cm^2V^{-1}s^{-1}$, as specified above. At low temperatures the difference in mobility at 10 K is more pronounce: the highest mobility 280 $cm^2V^{-1}s^{-1}$ is obtained for $MAPbI_3$ and the lowest one 100 $cm^2V^{-1}s^{-1}$ is for $CsPbI_3$ and $(Cs,FA)PbI_3$ at 10 K. The mobility spectra at low temperatures for $MAPbI_3$ and $CsPbI_3$ show a rather Drude-like mobility behavior. Charge carrier localization becomes more evident with increase in temperature in these thin films. The perovskites thin films with more complicated cation composition $(Cs,FA)PbI_3$ and $(Cs,FA,MA)Pb(I,Br)_3$ show the signs of localization of charge carriers already at 10 K. The reduction of mobility for the last two thin films indicates a larger amount of impurities and the corresponding increase in scattering rate.

Another class of materials of interest in this thesis is two-dimensional halide perovskites. The following thin films $BA_2MA_{n-1}Pb_nI_{3n+1}$ with various number of metal-halide $[PbI_6]^{4-}$ sheets layers (n=2-4), separated by layers of hydrophobic bulky cations, were produced by hot-injection method and were provided by S. Zhang from Potsdam University.

The mobilities in thin films reduce from (8.0 ± 0.9) $cm^2V^{-1}s^{-1}$ for (n = 4) to (3.7 ± 0.4) $cm^2V^{-1}s^{-1}$ (n = 2). The reduction of mobility with reduction of number of metal-halide sheets n is accompanied with decrease of the phenomenological parameter c_1 from -0.72 (n = 4) to -0.97 (n = 2). Such a decrease indicates the increase in localization of charge carriers in confined structures. The localization length L, defined from the modified Drude-Smith fit, is in the range from 3.7 nm for (n = 4) to 0.91 (n = 2). These values of localization lengths are comparable to thickness of metal-halide layers, indicating that charge carriers are rather localized within metal-halide layers. The reduction of mobility with n value is intuitively understandable due to charge carrier confinement within the metal-halide layers. However, the quantitative analysis of quantum and dielectric confinement and their impact on charge carrier transport are still required for 2D halide perovskites.

The layers orientation may also have an impact on charge carrier transport in two-dimensional halide perovskites thin films. The studies of mobility in this thesis, depending on the orientation of the layers with regard to polarization plane of THz field, clearly shows an anisotropy of the mobility.

Moreover, it was found that charge carrier dynamics in thin films (n = 3-4) have similarities to three-dimensional halide perovskites thin films ($MAPbI_3$). For these thin films (n = 3-4) thermalization and charge cooling occur within picoseconds, similar to $MAPbI_3$. The total decay times in thin films, obtained from the multi-exponential fit, increase from 1.4 ns to 5.7 ns with increasing of the number of metal-halide sheets n. This is highly likely due to enhanced radiative or Auger recombination for increasing confinement. In contrast, charge carrier dynamics in the thin film with n = 2 exhibit an additionally very fast decay within 390 fs after sample photoexcitation, which is attributed to an enhanced exciton formation.

The nano-crystalline thin films $CsPbI_3$ were produced by hot-injection method and were treated afterwards by M. Kärgel at the Helmholtz Zentrum Berlin. The post-treatments, in particular removal of the ligands, annealing and coating the NCs with formamidinium FA and formamidinium/lead FAw/Pb, were done in order to enhance the coupling between the nanocrystals. The impact of post-treatments on the charge carrier mobility was investigated by THz Spectroscopy. The thin films with washed ligands and annealed afterward show mobility lower than 1 $cm^2V^{-1}s^{-1}$. The thin films coated with FA and FA w/Pb) show enhanced mobility 1.5 and 1.0 $cm^2V^{-1}s^{-1}$, respectively.

8. Appendices

Abbreviation List

SC	Sollar cell
PCE	Power Conversion Efficiency
MHP	Metal Halide Perovskites
OPTP	Optical Pump THz Probe Spectroscopy
PLQY	Photoluminescence quantum yield
TRPL	Time Resolved Photoluminescence
TRTS	Time Resolved THz Spectroscopy
TRMC	Time resolved microwave spectroscopy
SCLC	Space charge limited current
MA	Methylammonium
FA	Formamidinium
OA	oleylamine
OLA	octylamine
MeOAc	methyl acetat
RPP	Ruddlesden – Popper perovskites
AM	Air Mass
NC	Nanocrystal

References

1. Luceño-Sánchez, J. A., Díez-Pascual, A. M. & Capilla, R. P. Materials for photovoltaics: State of art and recent developments. *Int. J. Mol. Sci.* **20**, (2019).

2. P. Würfel, U. W. *Physics of Solar Cells: From Basic Principles to Advanced Concepts*. *Physics of Solar Cells* (Wiley-VCH, 2016).

3. Moller, C. K. Crystal Structure and Photoconductivity of Caesium Plumbohalides. *Nature* **182**, 1436 (1958).

4. Kojima, A., Teshima, K., Shirai, Y. & Miyasaka, T. Organometal halide perovskites as visible-light sensitizers for photovoltaic cells. *J. Am. Chem. Soc.* **131**, 6050–6051 (2009).

5. Manser, J. S., Christians, J. A. & Kamat, P. V. Intriguing Optoelectronic Properties of Metal Halide Perovskites. *Chem. Rev.* **116**, 12956–13008 (2016).

6. Qiu, L., He, S., Ono, L. K., Liu, S. & Qi, Y. Scalable Fabrication of Metal Halide Perovskite Solar Cells and Modules. *ACS Energy Lett.* **4**, 2147–2167 (2019).

7. Bercegol, A. *et al.* Slow Diffusion and Long Lifetime in Metal Halide Perovskites for Photovoltaics. *J. Phys. Chem. C* **122**, 24570–24577 (2018).

8. Milot, R. L., Eperon, G. E., Snaith, H. J., Johnston, M. B. & Herz, L. M. Temperature-Dependent Charge-Carrier Dynamics in CH3NH3PbI3 Perovskite Thin Films. *Adv. Funct. Mater.* **25**, 6218–6227 (2015).

9. Herz, L. M. Charge-Carrier Mobilities in Metal Halide Perovskites: Fundamental Mechanisms and Limits. *ACS Energy Lett.* **2**, 1539–1548 (2017).

10. Alcocer, M. J. P., Leijtens, T., Herz, L. M., Petrozza, A. & Snaith, H. J. Electron-Hole Diffusion Lengths Exceeding Trihalide Perovskite Absorber. *Science (80-.).* **342**, 341–344 (2013).

11. Herz, L. M. Charge-Carrier Dynamics in Organic-Inorganic Metal Halide Perovskites. *Annu. Rev. Phys. Chem.* **67**, 65–89 (2016).

12. De Wolf, S. *et al.* Organometallic halide perovskites: Sharp optical absorption edge and its relation to photovoltaic performance. *J. Phys. Chem. Lett.* **5**, 1035–1039 (2014).

13. Wehrenfennig, C., Liu, M., Snaith, H. J., Johnston, M. B. & Herz, L. M. Homogeneous emission line broadening in the organo lead halide perovskite CH3NH3PbI3- xClx. *J. Phys. Chem. Lett.* **5**, 1300–1306 (2014).

14. Leijtens, T. *et al.* Towards enabling stable lead halide perovskite solar cells; Interplay between structural, environmental, and thermal stability. *J. Mater. Chem. A* **5**, 11483–11500 (2017).

15. Noh, J. H., Im, S. H., Heo, J. H., Mandal, T. N. & Seok, S. Il. Chemical management for colorful, efficient, and stable inorganic-organic hybrid nanostructured solar cells. *Nano Lett.* **13**, 1764–1769 (2013).

16. McMeekin, D. P. *et al.* A mixed-cation lead mixed-halide perovskite absorber for tandem solar cells. *Science (80-.).* **351**, 151–155 (2016).

17. Bi, D. *et al.* High-performance perovskite solar cells with enhanced environmental stability based on amphiphile-modified CH3NH3PbI3. *Adv. Mater.* **28**, 2910–2915 (2016).

18. Han, Y. *et al.* Degradation observations of encapsulated planar CH3NH3PbI3 perovskite solar cells at high temperatures and humidity. *J. Mater. Chem. A* **3**, 8139–8147 (2015).

19. Kirchartz, T. & Rau, U. What Makes a Good Solar Cell? *Adv. Energy Mater.* **8**, (2018).

20. Frost, J. M. Calculating polaron mobility in halide perovskites. *Phys. Rev. B* **96**, 1–10 (2017).

21. Sendner, M. *et al.* Optical phonons in methylammonium lead halide perovskites and implications for charge transport. *Mater. Horizons* **3**, 613–620 (2016).

22. Filippetti, A., Mattoni, A., Caddeo, C., Saba, M. I. & Delugas, P. Low electron-polar optical phonon scattering as a fundamental aspect of carrier mobility in methylammonium lead halide CH3NH3PbI3 perovskites. *Phys. Chem. Chem. Phys.* **18**, 15352–15362 (2016).

23. Mante, P. A., Stoumpos, C. C., Kanatzidis, M. G. & Yartsev, A. Electron-acoustic phonon coupling in single crystal CH3NH3PbI3 perovskites revealed by coherent acoustic phonons. *Nat. Commun.* **8**, 1–7 (2017).

24. Bonn, M., Miyata, K., Hendry, E. & Zhu, X. Y. Role of Dielectric Drag in Polaron Mobility in Lead Halide Perovskites. *ACS Energy Letters* **2**, 2555–2562 (2017).

25. Yu, Z. G. Rashba Effect and Carrier Mobility in Hybrid Organic-Inorganic Perovskites. *J. Phys. Chem. Lett.* **7**, 3078–3083 (2016).

26. Mayers, M. Z., Tan, L. Z., Egger, D. A., Rappe, A. M. & Reichman, D. R. How Lattice and Charge Fluctuations Control Carrier Dynamics in Halide Perovskites. *Nano Lett.* **18**, 8041–8046 (2018).

27. Jacoboni, C. *Theory of Electron Transport in Semiconductors*. (Springer, 2010).

28. Ridley, B. K. *Quantum Processes in Semiconductors*. (Oxford University Press, 1999).

29. Yu, Peter Y., M. C. *Fundamentals of Semiconductors. Physics and Materials Properties.* (Springer, 2010). doi:10.1016/j.msec.2007.10.028

30. Devreese, J. T. Polarons. *Encyclopedia of Applied Physics* 383–489 (1996). doi:10.1016/B978-0-12-374984-0.01182-7

31. Devreese, J. T. & Alexandrov, A. S. Fröhlich polaron and bipolaron: Recent developments. *Reports Prog. Phys.* **72**, (2009).

32. Katan, C., Mercier, N. & Even, J. Quantum and Dielectric Confinement Effects in Lower-Dimensional Hybrid Perovskite Semiconductors. *Chem. Rev.* **119**, 3140–3192 (2019).

33. Marongiu, D., Saba, M., Quochi, F., Mura, A. & Bongiovanni, G. The role of excitons in 3D and 2D lead halide perovskites. *J. Mater. Chem. C* **7**, 12006–12018 (2019).

34. Singh, J. *Modern Physics for Engineers.* (WILEY-VCH Verlag GmbH & Co. KGaA, 2004). doi:10.1119/1.1974132

35. Sze, S. M. *Physics of Semiconductor Devices*. (John Wiley & Sons, 1981).

36. R. Stratton. The influence of interelectronic collisions on conduction and breakdown in polar crystals. *Proceeding R. London Ser. a-mathematical Phys. Sci.* **246**, 406–422 (1958).

37. Conwell, E. M. & Vassell, M. O. High-field transport in n- Type GaAs. *Phys. Rev.* **166**, 797–821 (1968).

38. Sclar, N. Neutral Impurity Scattering in Smiconductors. *Phys. Rev.* **104**, 1559–1561 (1956).

39. T. C. McGill, R. B. Neutral Impurity Scattering. *Phys. Rev* **11**, 5208–5210 (1974).

40. Feynman, R. P., Hellwarth, R. W., Iddings, C. K. & Platzman, P. M. Mobility of slow electrons in a polar crystal. *Phys. Rev.* **127**, 1004–1017 (1962).

41. Kadanoff, L. P. Boltzmann equation for polarons. *Phys. Rev.* **130**, 1364–1369 (1963).

42. Hellwarth, R. W. & Biaggio, I. Mobility of an electron in a multimode polar lattice. **60**, 299–307 (1999).

43. Stoumpos, C. C. *et al.* High Members of the 2D Ruddlesden-Popper Halide Perovskites: Synthesis, Optical Properties, and Solar Cells of (CH3(CH2)3NH3)2(CH3NH3)4Pb5I16. *Chem* **2**, 427–440 (2017).

44. Ulbricht, R., Hendry, E., Shan, J., Heinz, T. F. & Bonn, M. Carrier dynamics in semiconductors studied with time-resolved terahertz spectroscopy. *Rev. Mod. Phys.* **83**, 543–586 (2011).

45. Joyce, H. J., Boland, J. L., Davies, C. L., Baig, S. A. & Johnston, M. B. A review of the electrical properties of semiconductor nanowires: Insights gained from terahertz conductivity spectroscopy. *Semiconductor Science and Technology* **31**, (2016).

46. Dexheimer, S. Time-Resolved Terahertz Studies of Conductivity Processes in Novel Electronic Materials. in *Terahertz Spectroscopy: Principles and Applications* (ed. Dexheimer, S.) 171–204 (CRC Press, 2017).

47. Funk, S., Acuna, G., Handloser, M. & Kersting, R. Probing the momentum relaxation time of charge carriers in ultrathin layers with terahertz radiation. *Opt. Express* **17**, 17450 (2009).

48. Jensen, B. The frequency-dependent relaxation time of free carriers in InP. *J. Appl. Phys.* **50**, 5800–5804 (1979).

49. Kübler, J. K. The Exciton Binding Energy of III–V Semiconductor Compounds. *Phys. Status Solidi* **35**, 189–195 (1969).

50. Causley, R. L. & Lewis, R. A. Characterisation of indium phosphide using terahertz radiation. *IEEE Semicond. Semi-Insulating Mater. Conf. SIMC* **2000**-**Janua**, 101–104 (2000).

51. Hass, M. & Henvis, B. W. Infrared lattice reflection spectra of III-V compound semiconductors. *J. Phys. Chem. Solids* **23**, 1099–1104 (1962).

52. Bergren, M. R., Palomaki, P. K. B., Neale, N. R., Furtak, T. E. & Beard, M. C. Size-Dependent Exciton Formation Dynamics in Colloidal Silicon Quantum Dots. *ACS Nano* **10**, 2316–2323 (2016).

53. Bretschneider, S. A. *et al.* Quantifying Polaron Formation and Charge Carrier Cooling in Lead-Iodide Perovskites. *Adv. Mater.* **30**, (2018).

54. Burgos-Caminal, A., Socie, E., Bouduban, M. E. F. & Moser, J. E. Exciton and Carrier Dynamics in Two-Dimensional Perovskites. *J. Phys. Chem. Lett.* **11**, 7692–7701 (2020).

55. Iwaszczuk, K., Cooke, D. G., Fujiwara, M., Hashimoto, H. & Uhd Jepsen, P. Simultaneous reference and differential waveform acquisition in time-resolved terahertz spectroscopy. *Opt. Express* **17**, 21969 (2009).

56. Smith, N. V. Classical generalization of the Drude formula for the optical conductivity. *Phys. Rev. B - Condens. Matter Mater. Phys.* **64**, (2001).

57. Cocker, T. L. *et al.* Microscopic origin of the Drude-Smith model. *Phys. Rev. B* **96**, (2017).

58. Jung, E. H. *et al.* Efficient, stable and scalable perovskite solar cells using poly(3-hexylthiophene). *Nature* **567**, 511–515 (2019).

59. Rehman, W. *et al.* Photovoltaic mixed-cation lead mixed-halide perovskites: Links between crystallinity, photo-stability and electronic properties. *Energy Environ. Sci.* **10**, 361–369 (2017).

60. Rehman, W. *et al.* Charge-Carrier Dynamics and Mobilities in Formamidinium Lead Mixed-Halide Perovskites. *Adv. Mater.* **27**, 7938–7944 (2015).

61. Karakus, M. *et al.* Phonon-Electron Scattering Limits Free Charge Mobility in Methylammonium Lead Iodide Perovskites. *J. Phys. Chem. Lett.* **6**, 4991–4996 (2015).

62. Kumar, A. Ultrafast THz photophysics of solvent engineered triple.cation halide perovskites. *J. Appl. Phys.* **124**, 215106 (2018).

63. Ponseca, C. S. *et al.* Organometal halide perovskite solar cell materials rationalized: Ultrafast charge generation, high and microsecond-long balanced mobilities, and slow recombination. *J. Am. Chem. Soc.* **136**, 5189–5192 (2014).

64. Herz, L. M. How Lattice Dynamics Moderate the Electronic Properties of Metal-Halide Perovskites. *J. Phys. Chem. Lett.* **9**, 6853–6863 (2018).

65. Zhao, T., Shi, W., Xi, J., Wang, D. & Shuai, Z. Intrinsic and Extrinsic Charge Transport in CH3 NH3 PbI3 Perovskites Predicted from First-Principles. *Sci. Rep.* **7**, 1–9 (2016).

66. Oga, H., Saeki, A., Ogomi, Y., Hayase, S. & Seki, S. Improved understanding of the electronic and energetic landscapes of perovskite solar cells: High local charge carrier mobility, reduced recombination, and extremely shallow traps. *J. Am. Chem. Soc.* **136**, 13818–13825 (2014).

67. Biewald, A. *et al.* Temperature-Dependent Ambipolar Charge Carrier Mobility in Large-Crystal Hybrid Halide Perovskite Thin Films. *ACS Appl. Mater. Interfaces* **11**, 20838–20844 (2019).

68. Shrestha, S. *et al.* Assessing Temperature Dependence of Drift Mobility in Methylammonium Lead Iodide Perovskite Single Crystals. *J. Phys. Chem. C* **122**, 5935–5939 (2018).

69. Davies, C. L. *et al.* Impact of the Organic Cation on the Optoelectronic Properties of Formamidinium Lead Triiodide. *J. Phys. Chem. Lett.* **9**, 4502–4511 (2018).

70. Egger, D. A. *et al.* What Remains Unexplained about the Properties of Halide Perovskites? *Adv. Mater.* **30**, 1–11 (2018).

71. Zhang, S. *et al.* Interface Engineering of Solution-Processed Hybrid Organohalide Perovskite Solar Cells. *ACS Appl. Mater. Interfaces* **10**, 21681–21687 (2018).

72. Stolterfoht, M. *et al.* The perovskite/transport layer interfaces dominate non-radiative recombination in efficient perovskite solar cells. *arXiv* 1–28 (2018).

73. Becker, P. *et al.* Low Temperature Synthesis of Stable γ-CsPbI3 Perovskite Layers for Solar Cells Obtained by High Throughput Experimentation. *Adv. Energy Mater.* **9**, 16–19 (2019).

74. Pérez-Osorio, M. A. *et al.* Vibrational Properties of the Organic-Inorganic Halide Perovskite CH3NH3PbI3 from Theory and Experiment: Factor Group Analysis, First-Principles Calculations, and Low-Temperature Infrared Spectra. *J. Phys. Chem. C* **119**, 25703–25718 (2015).

75. Damle, V. H., Gouda, L., Tirosh, S. & Tischler, Y. R. Structural Characterization and Room Temperature Low-Frequency Raman Scattering from MAPbI3 Halide Perovskite Films Rigidized by Cesium Incorporation. *ACS Appl. Energy Mater.* **1**, 6707–6713 (2018).

76. Giorgi, G., Fujisawa, J. I., Segawa, H. & Yamashita, K. Small photocarrier effective masses featuring ambipolar transport in methylammonium lead iodide perovskite: A density functional analysis. *J. Phys. Chem. Lett.* **4**, 4213–4216 (2013).

77. Galkowski, K. *et al.* Determination of the exciton binding energy and effective masses for methylammonium and formamidinium lead tri-halide perovskite semiconductors. *Energy*

Environ. Sci. **9**, 962–970 (2016).

78. Staub, F. *et al.* Beyond Bulk Lifetimes: Insights into Lead Halide Perovskite Films from Time-Resolved Photoluminescence. *Phys. Rev. Appl.* **6**, 1–13 (2016).

79. Ruf, F. *et al.* Temperature-dependent studies of exciton binding energy and phase-transition suppression in (Cs,FA,MA)Pb(I,Br)3 perovskites. *APL Mater.* **7**, (2019).

80. La-O-Vorakiat, C. *et al.* Elucidating the role of disorder and free-carrier recombination kinetics in CH 3 NH 3 PbI 3 perovskite films. *Nat. Commun.* **6**, 1–8 (2015).

81. Luo, L. *et al.* Ultrafast terahertz snapshots of excitonic Rydberg states and electronic coherence in an organometal. *Nat. Commun.* **8**, 1–8 (2017).

82. Valverde-Chávez, D. A. *et al.* Intrinsic femtosecond charge generation dynamics in single crystal CH3NH3PbI3. *Energy Environ. Sci.* **8**, 3700–3707 (2015).

83. Katzenellenbogen, N. & Grischkowsky, D. Electrical characterization to 4 THz of N- and P-type GaAs using THz time-domain spectroscopy. *Appl. Phys. Lett.* **61**, 840–842 (1992).

84. Lee, B. J. & Zhang, Z. M. Temperature and doping dependence of the radiative properties of silicon: Drude model revisited. in *13th IEEE International Conference on Advanced Thermal Processing of Semiconductors, RTP 2005* 251–260 (2005). doi:10.1109/RTP.2005.1613717

85. Zhai, Y. *et al.* Individual Electron and Hole Mobilities in Lead-Halide Perovskites Revealed by Noncontact Methods. *ACS Energy Lett.* **5**, 47–55 (2019).

86. Hartono, N. T. P. *et al.* The effect of structural dimensionality on carrier mobility in lead-halide perovskites. *J. Mater. Chem. A* **7**, 23949–23957 (2019).

87. Frost, J. M., Whalley, L. D. & Walsh, A. Slow Cooling of Hot Polarons in Halide Perovskite Solar Cells. *ACS Energy Lett.* **2**, 2647–2652 (2017).

88. Yang, Y. *et al.* Observation of a hot-phonon bottleneck in lead-iodide perovskites. *Nat. Photonics* **10**, 53–59 (2016).

89. Poncé, S., Schlipf, M. & Giustino, F. Origin of Low Carrier Mobilities in Halide Perovskites. *ACS Energy Lett.* **4**, 456–463 (2019).

90. Miyata, K., Atallah, T. L. & Zhu, X. Y. Lead halide perovskites: Crystal-liquid duality, phonon glass electron crystals, and large polaron formation. *Science Advances* **3**, 1–11 (2017).

91. Zhao, D. *et al.* Low-frequency optical phonon modes and carrier mobility in the halide perovskite CH3NH3PbBr3 using terahertz time-domain spectroscopy. *Appl. Phys. Lett.* **111**, (2017).

92. Umari, P., Mosconi, E. & De Angelis, F. Relativistic GW calculations on CH3 NH3 PbI 3 and CH3 NH3 SnI3 Perovskites for Solar Cell Applications. *Sci. Rep.* **4**, 1–7 (2014).

93. Menéndez-Proupin, E., Palacios, P., Wahnón, P. & Conesa, J. C. Self-consistent relativistic band structure of the CH3 NH3 PbI3 perovskite. *Phys. Rev. B - Condens. Matter Mater. Phys.* **90**, 1–7 (2014).

94. Rakita, Y., Cohen, S. R., Kedem, N. K., Hodes, G. & Cahen, D. Mechanical properties of APbX3 (A = Cs or CH3NH3; X = i or Br) perovskite single crystals. *MRS Commun.* **5**, 623–629 (2015).

95. Butler, K. T., Frost, J. M. & Walsh, A. Band alignment of the hybrid halide perovskites CH3NH3PbCl3, CH3NH3PbBr3 and CH3NH3PbI3. *Mater. Horizons* **2**, 228–231 (2015).

96. Coll, M. *et al.* Polarization switching and light-enhanced piezoelectricity in lead halide

perovskites. *J. Phys. Chem. Lett.* **6**, 1408–1413 (2015).

97. Brenner, T. M. *et al.* Are Mobilities in Hybrid Organic-Inorganic Halide Perovskites Actually 'high'? *J. Phys. Chem. Lett.* **6**, 4754–4757 (2015).

98. Zhu, X. Y. & Podzorov, V. Charge Carriers in Hybrid Organic-Inorganic Lead Halide Perovskites Might Be Protected as Large Polarons. *J. Phys. Chem. Lett.* **6**, 4758–4761 (2015).

99. Wright, A. D. *et al.* Electron-phonon coupling in hybrid lead halide perovskites. *Nat. Commun.* **7**, (2016).

100. Walsh, A., Scanlon, D. O., Chen, S., Gong, X. G. & Wei, S. H. Self-regulation mechanism for charged point defects in hybrid halide perovskites. *Angew. Chemie - Int. Ed.* **54**, 1791–1794 (2015).

101. Motti, S. G. *et al.* Defect Activity in Lead Halide Perovskites. *Advanced Materials* **31**, 1–11 (2019).

102. Polyakov, A. Y. *et al.* Trap states in multication mesoscopic perovskite solar cells: A deep levels transient spectroscopy investigation. *Applied Physics Letters* **113**, (2018).

103. Miyata, A. *et al.* Direct measurement of the exciton binding energy and effective masses for charge carriers in organic-inorganic tri-halide perovskites. *Nat. Phys.* **11**, 582–587 (2015).

104. D'Innocenzo, V. *et al.* Excitons versus free charges in organo-lead tri-halide perovskites. *Nat. Commun.* **5**, 1–6 (2014).

105. Wehrenfennig, C., Liu, M., Snaith, H. J., Johnston, M. B. & Herz, L. M. Charge-carrier dynamics in vapour-deposited films of the organolead halide perovskite CH3NH3PbI3-xClx. *Energy Environ. Sci.* **7**, 2269–2275 (2014).

106. Bokdam, M. *et al.* Role of Polar Phonons in the Photo Excited State of Metal Halide Perovskites. *Sci. Rep.* **6**, 1–8 (2016).

107. Chen, Z. *et al.* Single-Crystal MAPbI3 Perovskite Solar Cells Exceeding 21% Power Conversion Efficiency. *ACS Energy Lett.* **4**, 1258–1259 (2019).

108. Elumalai, N. K., Mahmud, M. A., Wang, D. & Uddin, A. Perovskite solar cells: Progress and advancements. *Energies* **9**, (2016).

109. Kang, Y. & Han, S. Intrinsic Carrier Mobility of Cesium Lead Halide Perovskites. *Phys. Rev. Appl.* **10**, 1 (2018).

110. Jong, U. G., Yu, C. J., Kim, Y. S., Kye, Y. H. & Kim, C. H. First-principles study on the material properties of the inorganic perovskite Rb1-xCsxPbI3 for solar cell applications. *Phys. Rev. B* **98**, (2018).

111. Quarti, C. *et al.* The raman spectrum of the CH3NH3PbI3 hybrid perovskite: Interplay of theory and experiment. *J. Phys. Chem. Lett.* **5**, 279–284 (2014).

112. Ferreira, A. C. *et al.* Elastic Softness of Hybrid Lead Halide Perovskites. *Phys. Rev. Lett.* **121**, 1–6 (2018).

113. Zheng, Y. *et al.* Unique characteristics of 2D Ruddlesden-Popper (2DRP) perovskite for future photovoltaic application. *J. Mater. Chem. A* **7**, 13860–13872 (2019).

114. Smith, I. C., Hoke, E. T., Solis-Ibarra, D., McGehee, M. D. & Karunadasa, H. I. A Layered Hybrid Perovskite Solar-Cell Absorber with Enhanced Moisture Stability. *Angew. Chemie - Int. Ed.* **53**, 11232–11235 (2014).

115. Zhang, F. *et al.* Advances in two-dimensional organic-inorganic hybrid perovskites. *Energy Environ. Sci.* **13**, 1154–1186 (2020).

116. Etgar, L. The merit of perovskite's dimensionality; Can this replace the 3D halide perovskite? *Energy Environ. Sci.* **11**, 234–242 (2018).

117. Xu, Z. *et al.* Phase Distribution and Carrier Dynamics in Multiple-Ring Aromatic Spacer-Based Two-Dimensional Ruddlesden-Popper Perovskite Solar Cells. *ACS Nano* **14**, 4871–4881 (2020).

118. Milot, R. L. *et al.* Charge-Carrier Dynamics in 2D Hybrid Metal-Halide Perovskites. *Nano Lett.* **16**, 7001–7007 (2016).

119. Buizza, L. R. V. *et al.* Charge-Carrier Dynamics, Mobilities, and Diffusion Lengths of 2D–3D Hybrid Butylammonium–Cesium–Formamidinium Lead Halide Perovskites. *Adv. Funct. Mater.* **29**, (2019).

120. Chen, Y. *et al.* Tailoring Organic Cation of 2D Air-Stable Organometal Halide Perovskites for Highly Efficient Planar Solar Cells. *Adv. Energy Mater.* **7**, 1–7 (2017).

121. Zhang, F. *et al.* Enhanced Charge Transport in 2D Perovskites via Fluorination of Organic Cation. *J. Am. Chem. Soc.* **141**, 5972–5979 (2019).

122. Venkatesan, N. R., Labram, J. G. & Chabinyc, M. L. Charge-Carrier Dynamics and Crystalline Texture of Layered Ruddlesden-Popper Hybrid Lead Iodide Perovskite Thin Films. *ACS Energy Lett.* **3**, 380–386 (2018).

123. Gao, L. *et al.* Improving Charge Transport via Intermediate-Controlled Crystal Growth in 2D Perovskite Solar Cells. *Adv. Funct. Mater.* **29**, 1–7 (2019).

124. Labram, J. G. *et al.* Charge transport in a two-dimensional hybrid metal halide thiocyanate compound. *J. Mater. Chem. C* **5**, 5930–5938 (2017).

125. Ishida, N., Wakamiya, A. & Saeki, A. Quantifying Hole Transfer Yield from Perovskite to Polymer Layer: Statistical Correlation of Solar Cell Outputs with Kinetic and Energetic Properties. *ACS Photonics* **3**, 1678–1688 (2016).

126. Zhang, X. *et al.* Stable high efficiency two-dimensional perovskite solar cells via cesium doping. *Energy Environ. Sci.* **10**, 2095–2102 (2017).

127. Zhang, X. *et al.* Orientation Regulation of Phenylethylammonium Cation Based 2D Perovskite Solar Cell with Efficiency Higher Than 11%. *Adv. Energy Mater.* **8**, 1–9 (2018).

128. Peng, J., Chen, Y., Zheng, K., Pullerits, T. & Liang, Z. Insights into charge carrier dynamics in organo-metal halide perovskites: From neat films to solar cells. *Chem. Soc. Rev.* **46**, 5714–5729 (2017).

129. Lian, X. *et al.* The Second Spacer Cation Assisted Growth of a 2D Perovskite Film with Oriented Large Grain for Highly Efficient and Stable Solar Cells. *Angew. Chemie - Int. Ed.* **58**, 9409–9413 (2019).

130. Lai, H. *et al.* Two-dimensional ruddlesden-popper perovskite with nanorod-like morphology for solar cells with efficiency exceeding 15%. *J. Am. Chem. Soc.* **140**, 11639–11646 (2018).

131. Solis De La Fuente, M. *et al.* Enhanced Charge Carrier Transport in 2D Perovskites by Incorporating Single-Walled Carbon Nanotubes or Graphene. *ACS Energy Lett.* **5**, 109–116 (2020).

132. Ma, C., Shen, D., Ng, T. W., Lo, M. F. & Lee, C. S. 2D Perovskites with Short Interlayer Distance for High-Performance Solar Cell Application. *Adv. Mater.* **30**, 2–7 (2018).

133. Quan, L. N. *et al.* Ligand-Stabilized Reduced-Dimensionality Perovskites. *J. Am. Chem. Soc.* **138**, 2649–2655 (2016).

134. Proppe, A. H. *et al.* Synthetic Control over Quantum Well Width Distribution and Carrier Migration in Low-Dimensional Perovskite Photovoltaics. *J. Am. Chem. Soc.* **140**, 2890–2896 (2018).

135. Chen, A. Z. *et al.* Understanding the Formation of Vertical Orientation in Two-dimensional Metal Halide Perovskite Thin Films. *Chem. Mater.* **31**, 1336–1343 (2019).

136. Chen, A. Z. *et al.* Origin of vertical orientation in two-dimensional metal halide perovskites and its effect on photovoltaic performance. *Nat. Commun.* **9**, 1–7 (2018).

137. Tsai, H. *et al.* High-efficiency two-dimensional ruddlesden-popper perovskite solar cells. *Nature* **536**, 312–317 (2016).

138. Cheng, P. *et al.* Highly Efficient Ruddlesden-Popper Halide Perovskite PA2MA4Pb5I16 Solar Cells. *ACS Energy Lett.* **3**, 1975–1982 (2018).

139. Soe, C. M. M. *et al.* Understanding Film Formation Morphology and Orientation in High Member 2D Ruddlesden–Popper Perovskites for High-Efficiency Solar Cells. *Adv. Energy Mater.* **8**, 2–11 (2018).

140. Fu, W. *et al.* Two-Dimensional Perovskite Solar Cells with 14.1% Power Conversion Efficiency and 0.68% External Radiative Efficiency. *ACS Energy Lett.* **3**, 2086–2093 (2018).

141. Qing, J. *et al.* Aligned and Graded Type-II Ruddlesden–Popper Perovskite Films for Efficient Solar Cells. *Adv. Energy Mater.* **8**, 1–8 (2018).

142. Blancon, J. C. *et al.* Extremely efficient internal exciton dissociation through edge states in layered 2D perovskites. *Science (80-.).* **355**, 1288–1292 (2017).

143. Kumar, A. *et al.* Excitons in 2D perovskites for ultrafast terahertz photonic devices. *Sci. Adv.* **6**, 1–9 (2020).

144. Zhang, X. *et al.* Vertically Oriented 2D Layered Perovskite Solar Cells with Enhanced Efficiency and Good Stability. *Small* **13**, 2–9 (2017).

145. Thouin, F. *et al.* Phonon coherences reveal the polaronic character of excitons in two-dimensional lead halide perovskites. *Nat. Mater.* **18**, 349–356 (2019).

146. Neutzner, S. *et al.* Exciton-polaron spectral structures in two-dimensional hybrid lead-halide perovskites. *Phys. Rev. Mater.* **2**, 1–10 (2018).

147. Srimath Kandada, A. R. & Silva, C. Exciton Polarons in Two-Dimensional Hybrid Metal-Halide Perovskites. *J. Phys. Chem. Lett.* **11**, 3173–3184 (2020).

148. Zhang, S. *et al.* The Role of Bulk and Interface Recombination in High-Efficiency Low-Dimensional Perovskite Solar Cells. *Adv. Mater.* **31**, 1–11 (2019).

149. Zibouche, N. & Islam, M. S. Structure-Electronic Property Relationships of 2D Ruddlesden-Popper Tin- And Lead-based Iodide Perovskites. *ACS Appl. Mater. Interfaces* **12**, 15328–15337 (2020).

150. Wang, K. *et al.* Distinct conducting layer edge states in two-dimensional (2D) halide perovskite. *Sci. Adv.* **5**, 1–11 (2019).

151. Yang, J. *et al.* Acoustic-optical phonon up-conversion and hot-phonon bottleneck in lead-halide perovskites. *Nat. Commun.* **8**, (2017).

152. Liu, C. *et al.* Metal Halide Perovskite Nanocrystal Solar Cells: Progress and Challenges. *Small Methods* **2000419**, 1–20 (2020).

153. Akkerman, Q. A., Rainò, G., Kovalenko, M. V. & Manna, L. Genesis, challenges and opportunities for colloidal lead halide perovskite nanocrystals. *Nat. Mater.* **17**, 394–405 (2018).

154. Li, M. *et al.* Slow cooling and highly efficient extraction of hot carriers in colloidal perovskite nanocrystals. *Nat. Commun.* **8**, 3–12 (2017).

155. Zhao, Q. *et al.* High efficiency perovskite quantum dot solar cells with charge separating heterostructure. *Nat. Commun.* **10**, (2019).

156. Suri, M. *et al.* Enhanced Open-Circuit Voltage of Wide-Bandgap Perovskite Photovoltaics by Using Alloyed (FA1- xCsx)Pb(I1- xBrx)3 Quantum Dots. *ACS Energy Lett.* **4**, 1954–1960 (2019).

157. Ling, X. *et al.* 14.1% CsPbI3 Perovskite Quantum Dot Solar Cells via Cesium Cation Passivation. *Adv. Energy Mater.* **9**, 1–9 (2019).

158. Liu, C. *et al.* Surface Ligands Management for Efficient CsPbBrI2 Perovskite Nanocrystal Solar Cells. *Sol. RRL* **4**, 1–9 (2020).

159. Sarkar, S. *et al.* Terahertz Spectroscopic Probe of Hot Electron and Hole Transfer from Colloidal CsPbBr3 Perovskite Nanocrystals. *Nano Lett.* **17**, 5402–5407 (2017).

160. Yettapu, G. R. *et al.* Terahertz Conductivity within Colloidal CsPbBr3 Perovskite Nanocrystals: Remarkably High Carrier Mobilities and Large Diffusion Lengths. *Nano Lett.* **16**, 4838–4848 (2016).

161. Schmidt, L. C. *et al.* Nontemplate synthesis of CH3NH3PbBr3 perovskite nanoparticles. *J. Am. Chem. Soc.* **136**, 850–853 (2014).

162. Zhang, F. *et al.* Brightly luminescent and color-tunable colloidal CH3NH3PbX3 (X = Br, I, Cl) quantum dots: Potential alternatives for display technology. *ACS Nano* **9**, 4533–4542 (2015).

163. Protesescu, L. *et al.* Nanocrystals of Cesium Lead Halide Perovskites (CsPbX<inf>3</inf>, X = Cl, Br, and I): *Nano Lett.* **15**, 3692–3696 (2015).

164. Sanehira, E. M. *et al.* Enhanced mobility CsPbI3 quantum dot arrays for record-efficiency, high-voltage photovoltaic cells. *Sci. Adv.* **3**, (2017).

165. Pan, J. *et al.* Highly Efficient Perovskite-Quantum-Dot Light-Emitting Diodes by Surface Engineering. *Adv. Mater.* **28**, 8718–8725 (2016).

166. Xue, J. *et al.* Surface Ligand Management for Stable FAPbI3 Perovskite Quantum Dot Solar Cells. *Joule* **2**, 1866–1878 (2018).

167. Yuan, J. *et al.* Spray-Coated Colloidal Perovskite Quantum Dot Films for Highly Efficient Solar Cells. *Adv. Funct. Mater.* **29**, 1–7 (2019).

168. Chen, K. *et al.* Short-Chain Ligand-Passivated Stable α-CsPbI3 Quantum Dot for All-Inorganic Perovskite Solar Cells. *Adv. Funct. Mater.* **29**, 1–8 (2019).

169. Yuan, X. *et al.* Temperature-dependent photoluminescence of inorganic perovskite nanocrystal films. *RSC Adv.* **6**, 78311–78316 (2016).

170. Diroll, B. T., Zhou, H. & Schaller, R. D. Low-Temperature Absorption, Photoluminescence, and Lifetime of CsPbX3 (X = Cl, Br, I) Nanocrystals. *Adv. Funct. Mater.* **28**, 1–7 (2018).

171. Luo, B. *et al.* Synthesis, Optical Properties, and Exciton Dynamics of Organolead Bromide

Perovskite Nanocrystals. *J. Phys. Chem. C* **119**, 26672–26682 (2015).

172. Aneesh, J. *et al.* Ultrafast Exciton Dynamics in Colloidal CsPbBr3 Perovskite Nanocrystals: Biexciton Effect and Auger Recombination. *J. Phys. Chem. C* **121**, 4734–4739 (2017).

173. Ghosh, S. *et al.* Phonon Coupling with Excitons and Free Carriers in Formamidinium Lead Bromide Perovskite Nanocrystals. *J. Phys. Chem. Lett.* **9**, 4245–4250 (2018).

174. Sun, S., Yuan, D., Xu, Y., Wang, A. & Deng, Z. Ligand-Mediated Synthesis of Shape-Controlled Cesium Lead Halide Perovskite Nanocrystals via Reprecipitation Process at Room Temperature. *ACS Nano* **10**, 3648–3657 (2016).

175. Dirin, D. N. *et al.* Harnessing Defect-Tolerance at the Nanoscale: Highly Luminescent Lead Halide Perovskite Nanocrystals in Mesoporous Silica Matrixes. *Nano Lett.* **16**, 5866–5874 (2016).

176. Protesescu, L. *et al.* Dismantling the 'red Wall' of Colloidal Perovskites: Highly Luminescent Formamidinium and Formamidinium-Cesium Lead Iodide Nanocrystals. *ACS Nano* **11**, 3119–3134 (2017).

Acknowledgement

This thesis were not be possible to finish without help and support of many people, who I worked with and who supported me psychologically and professionally.

First, I would like to thank Dr. Thomas Unold, my supervisor from the HZB, for opportunity to work at HZB, for his expertise in Photovoltaics area, constructive critics and useful advices that made possible to bring my work forward and to successfully finish the thesis.

I would like to acknowledge Prof. Dr. Neher, my supervisor from Potsdam University, for his constructive feedback regarding my research.

Specially I would like to express many thanks to Hannes Hempel, who guided me through all way of PhD study by helping a lot with THz set-up, who helped me to develop ideas for my research work and who, was always the first, who I could address all my questions and any kind of arising problems during my research.

Thanks a lot to my boyfriend Alexander and to my parents, who supported me morally and encouraged me to never give up especially at rough times.

Moreover, I would like to acknowledge my colleagues:

Rainer Eichberger, Sönke Müller, Dennis Friedrich for possibility to perform the measurements in the THz laboratory and for the help of operating the laser system.

Martin Stolterfoht, S. Zhang, Martin Kärgel and Pascal Becker for providing the samples for measurements.

Thanks to my colleagues Pascal Becker, Martin Kärgel, Jose Marquez Prieto, Sergei Levcenco, Marin Rusu for constructive advise and helpful discussions for my research at HZB.

Furthermore, I would like to thank the MatSec school for financial support during my PhD study at the HZB.

Abstract

Halide perovskites are a class of novel photovoltaic materials that have recently attracted much attention in the photovoltaics research community due to their highly promising optoelectronic properties, including large absorption coefficients and long carrier lifetimes. The charge carrier mobility of halide perovskites is investigated in this thesis by THz spectroscopy, which is a contact-free technique that yields the intra-grain sum mobility of electrons and holes in a thin film.

The polycrystalline halide perovskite thin films, provided from Potsdam University, show moderate mobilities in the range from 21.5 to 33.5 $cm^2V^{-1}s^{-1}$. It is shown in this work that the room temperature mobility is limited by charge carrier scattering at polar optical phonons. The mobility at low temperature is likely to be limited by scattering at charged and neutral impurities at impurity concentration $N=10^{17}$-10^{18} cm^{-3}. Furthermore, it is shown that exciton formation may decrease the mobility at low temperatures. Scattering at acoustic phonons can be neglected at both low and room temperatures. The analysis of mobility spectra over a broad range of temperatures for perovskites with various cation compounds shows that cations have a minor impact on charge carrier mobility.

The low-dimensional thin films of quasi-2D perovskite with different numbers of $[PbI_6]^{4-}$ sheets (n=2-4) alternating with long organic spacer molecules were provided by S. Zhang from Potsdam University. They exhibit mobilities in the range from 3.7 to 8 $cm^2V^{-1}s^{-1}$. A clear decrease of mobility is observed with decrease in number of metal-halide sheets *n*, which likely arises from charge carrier confinement within metal-halide layers. Modelling the measured THz mobility with the modified Drude-Smith model yields localization length from 0.9 to 3.7 nm, which agrees well on the thicknesses of the metal-halide layers. Additionally, the mobilities are found to be dependent on the orientation of the layers. The charge carrier dynamics is also dependent on the number of metal-halide sheets *n*. For the thin films with n =3-4 the dynamics is similar to the 3D MHPs. However, the thin film with n = 2 shows clearly different dynamics, where the signs of exciton formation are observed within 390 fs timeframe after photoexcitation.

Also, the charge carrier dynamics of $CsPbI_3$ perovskite nanocrystals was investigated, in particular the effect of post treatments on the charge carrier transport.

Zusammenfassung

Metall-Halogenid Perowskite sind eine Klasse von photovoltaischen Materialien, welche in letzter Zeit sehr viel Aufmerksamkeit von Forschern bekommen haben. Der Grund dafür liegt in ihren vielversprechenden optoelektronischen Eigenschaften, wie beispielsweise hohe Absorptionskoeffizienten, lange Lebenszeiten der Ladungsträger und moderate Beweglichkeiten.

Die Beweglichkeit der Ladungsträger und deren Kinetik wurde in dieser Dissertation mit Hilfe von Teraherzspektroskopie in verschiedenen Metall-Halogenide Perowskiten untersucht.

Die polykristallinen Halogenide Perowskit-Dünnschichten, bereitgestellt von Dr. M. Stolterfoht von der Universität Potsdam, haben bei Raumtemperatur moderate Ladungsträgerbeweglichkeiten in einem Bereich von 21.5 bis 33.5 $cm^2V^{-1}s^{-1}$. Die Analyse dieser Beweglichkeiten in Abhängigkeit der Temperatur zeigt, dass die Beweglichkeit bei Raumtemperatur durch die Interaktion mit polaren optischen Phononen limitiert wird. Bei niedrigeren Temperaturen sind die Beweglichkeiten durch Streuung an geladenen und neutralen Störstellen limitiert, wobei die Störstellenkonzentration bei ca. $N = 10^{17}$-10^{18} cm^{-3} liegt. Weiterhin wird es gezeigt, dass die Reduktion der Anzahl beweglicher Ladungsträger durch Exzitonenbildung ebenfalls bei niedrigen Temperaturen berücksichtigt werden muss. Streuung an akustischen Phononen kann sowohl bei Raum- als auch bei niedrigen Temperaturen vernachlässigt werden. Die Analyse der Beweglichkeitsspektren von Perowskiten mit unterschiedlichen Kationen und bei verschiedenen Temperaturspannen zeigt, dass diese Kationen einen sehr geringen Einfluss auf die Ladungsträgerbeweglichkeit haben.

Niederdimensionale Perowskit-Dünnschichten aus alternierenden quasi-2D $[PbI_6]^{4-}$ Schichten *n* (*n*=3-4) und organischen Trennschichten wurde von S. Zhang von der Universität Potsdam bereitgestellt. Diese zeigen Beweglichkeiten zwischen 3.7 und 8 $cm^2V^{-1}s^{-1}$. Der signifikante Rückgang der beobachteten Beweglichkeit lässt sich auf die Anzahl der Metall-Halogeniden Schichten *n* zurückführen, in welcher die Ladungsträger räumlich eingeschränkt sind. Die Lokalisationslänge reicht von 0.9 bis 3.7 nm und ist vergleichbar mit der Dicke der einzelnen quasi-2D-Schichten. Ebenfalls ist die Beweglichkeit abhängig von der Schichtenorientierung. Zusätzlich ist die Ladungsträgerdynamik abhängig von der Anzahl der Metall-Halogeniden $[PbI_6]^{4-}$Schichten *n*. Dicke quasi-2D-Schichten (*n* = 3-4) zeigen ähnliche Dynamik wie drei dimensionale Perowskite, wogegen die dünnen quasi-2D-Schichten (*n* = 2) schnelle Exzitonbildung innerhalb 390 fs nach der Ladungsträgeranregung zeigen.

Des weiteren wurde die Ladungsträgerdynamik von $CsPbI_3$ Perovskite-Nanokristallen untersucht, insbesondere die Auswirkung von Ligandenaustausch und Temperierung auf die Ladungsträgerbeweglichkeit.

Selbstständigkeitserklärung

Hiermit erkläre ich, dass die Arbeit an keiner anderen Hochschule eingereicht sowie selbständig von mir und nur mit den angegebenen Mitteln angefertigt wurde.

_____

Andrei Petsiuk

List of publications

1. A. Petsiuk, H. Hempel, P. Becker, M. Stolterfoht, D. Neher, R. Eichberger, T. Unold, „Limits of charge carrier transport in metal halide perovskites" (In preparation)

Co-author

1. M. Kölbach, H. Hempel, K. Harbauer, M. Schleuning, A. Petsiuk, K. Höflich, V. Deinhart. D. Friedrich, R. Eichberger, F. F. Abdi, R. van de Krol; „Garin boundaries limit the charge carrier transport in pulsed laser deposited α- $SnWO_4$ thin film photoabsorbers", *ACS Appl. Energy Mater*. 2020, 3, 4320-4330
2. S. Zhang, S. M. Hosseini, R. Gunder, A. Petsiuk, P. Caprioglio, C. M. Wolff, S. Shoaee, P. Meredith, S. Schorr, T. Unold, P. L. Burn, D. Neher, M. Stolterfoht; "The role of bulk and interface recombination in high efficiency low dimensional perovskite solar cells", *Adv. Mater*. 2019, 31, 1901090.